ANL-76-15

ANL-76-15

LIGHT-WATER-REACTOR SAFETY RESEARCH PROGRAM: QUARTERLY PROGRESS REPORT

October–December 1975

U of C-AUA-USERDA

ARGONNE NATIONAL LABORATORY, ARGONNE, ILLINOIS

Prepared for the U. S. NUCLEAR REGULATORY COMMISSION
Office of Nuclear Regulatory Research

Printed in the United States of America
Available from
National Technical Information Service
U. S. Department of Commerce
5285 Port Royal Road
Springfield, Virginia 22161
Price: Printed Copy $5.00; Microfiche $2.25

Distribution Categories:
Water Reactor Safety
Research—Fuel Behavior
(NRC-3)
Water Reactor Safety
Research—Analysis Development
(NRC-4)

ANL-76-15

ARGONNE NATIONAL LABORATORY
9700 South Cass Avenue
Argonne, Illinois 60439

LIGHT-WATER-REACTOR SAFETY RESEARCH PROGRAM: QUARTERLY PROGRESS REPORT

October–December 1975

Robert G. Sachs, Laboratory Director
Jack A. Kyger, Associate Laboratory Director

Previous reports in this series:

ANL-75-28	January–March 1975
ANL-75-58	April–June 1975
ANL-75-72	July–September 1975

TABLE OF CONTENTS

TABLE OF CONTENTS

LIST OF FIGURES

LIST OF FIGURES

LIST OF FIGURES

LIST OF FIGURES

LIST OF TABLES

ABSTRACT

This progress report summarizes the Argonne National Laboratory work performed during October, November, and December 1975 on water-reactor-safety heat-transfer and flow problems. The following research and development areas are covered: (1) Loss-of-coolant Accident Research: Heat Transfer and Fluid Dynamics; (2) Transient Fuel Response and Fission-product Release Program; and (3) Mechanical Properties of Zircaloy Containing Oxygen.

I. LOSS-OF-COOLANT ACCIDENT RESEARCH: HEAT TRANSFER AND FLUID DYNAMICS

Responsible Section Managers:
M. A. Grolmes, R. E. Henry, and P. A. Lottes, RAS

A. Experimental Study of Energy Partition in Aluminum/Water Vapor Explosions (R. P. Anderson, RAS)

Explosions have been produced by sudden contact between molten aluminum and water in industrial accidents and laboratory experiments. The high-pressure gas in these events may have been generated by a sudden vaporization of the water (vapor explosion) or by a chemical reaction between the aluminum and water. Both types of reactions probably occur in real metal/water systems: Explosions in molten-silver/water systems[1] must be caused by vaporization, since the chemical-reaction potential is small while experimental studies in molten-aluminum/water systems have identified three sizes of explosions with the largest size generally assumed to be chemical in nature.[2] The ratio of production to water-vapor generation in a medium-scale aluminum/water explosion is a matter of some concern and debate. It is fundamentally important to the understanding and analysis of explosive reactions that the two energy-releasing mechanisms be isolated and studied separately. This is a difficult experimental task, since a vapor explosion and a partial oxidation reaction would produce similar pressurization rates. It may be possible to experimentally identify the oxidation reaction by measuring the total kinetic-energy release, sudden local temperature increases, or emission of light radiation.

An experimental program to study types of energy generation in aluminum/water reactions has been undertaken. The first requirement for such a program is a system capable of generating reproducible explosions while recording accurate measurements of pressure, temperature, and liquid velocities. An initial decision was made to try to generate explosions by contacting small quantities of water (less than 50 g) with modest quantities of aluminum (~1000 g). This geometry enjoys numerous advantages over large-scale systems; problems of personnel safety and equipment shielding are minimized, pressure and velocity variations are easier to measure, the geometry of the reacting water mass is easier to control, and the smaller dimensions make efficient reactions more likely, thus aiding the discrimination between chemical and vapor explosions. The geometry does have one outstanding disadvantage: No large-scale aluminum/water reactions have been produced in small systems of this type although explosions have been produced in small aluminum/water shock tubes.[3]

The presence of a stable vapor film separating the two liquids was assumed to cause the difficulty in generating explosions in small-scale systems. Experimental efforts to date have concentrated on attempts to initiate

a reaction by penetrating or collapsing this vapor film. Methods and results of these noninstrumented scoping tests are described below.

A furnace with an integral crucible was constructed as shown in Fig. I.1. The stainless steel crucible was 20 cm long with a 5-cm ID and a 6-cm OD; the furnace used 1000-W resistance heaters and 8-cm-thick, soft asbestos insulation. It was capable of heating 1000 g of aluminum to 1000°C in 3 hr.

The first three tests injected water jets of increasing velocity across a 10-cm air gap and into the molten-aluminum mass. The water injector was similar to that shown in Fig. I.1, but it lacked a transport cylinder and was thus locked in place during each test. The first test used a pressure of 9 atm to inject through a 15-cm-long, 0.3-cm-ID tube; the second test again used 9 atm, but removed the tube and injected directly out of the solenoid valve; and the third test retained this geometry while boosting the injection pressure to 31 atm. The results of all three tests were similar--a benign splashing of aluminum with no indication of an explosive reaction.

The effect of a noncondensible gas layer formed around the water jet as it traversed the 10-cm air gap might deter jet penetration through the gas/vapor film. An injector transport system was installed (as shown in Fig. I.1). Immediately preceding the water injection, the injector was lowered until the needle tip was 8 cm below the aluminum surface. A test with an injector pressure of 25 atm again produced benign splashing with no apparent large pressures.

It was decided to abandon efforts to produce an explosion by penetrating the gas film with a medium velocity jet and try to produce an explosion by collapsing the vapor film surrounding an entrapped water droplet. A series of vertical sliding concentric tubes was installed above the furnace. An annular graphite piston (5-cm OD x 2.5-cm ID) was floated on top the molten aluminum. A thin-walled glass sphere containing ~0.5 g of water and a small volume of air was cemented to the lower end of the longest, smallest-diameter tube in the concentric tube assembly. During a test, the tube assembly was allowed to drop under the force of gravity. The small inner tube and glass sphere would pass through the 2.5-cm hole in the graphite annular piston and penetrate to the bottom of the crucible, where the glass sphere would rupture. A larger concentric tube would continue to slide downward outside the arrested inner tube until it struck the graphite piston, generating a large pressure wave in the molten-aluminum mass. The first test of this type resulted in an apparent explosion; molten aluminum was splattered off a beam 6 m above the furnace.

Having apparently succeeded in the initial objective of producing a pressurization in a small-scale system, we have designed a new experimental system for the second stage of the program. It includes an improved concentric tube assembly and two furnaces with provision for instrumentation installation. It is currently under construction.

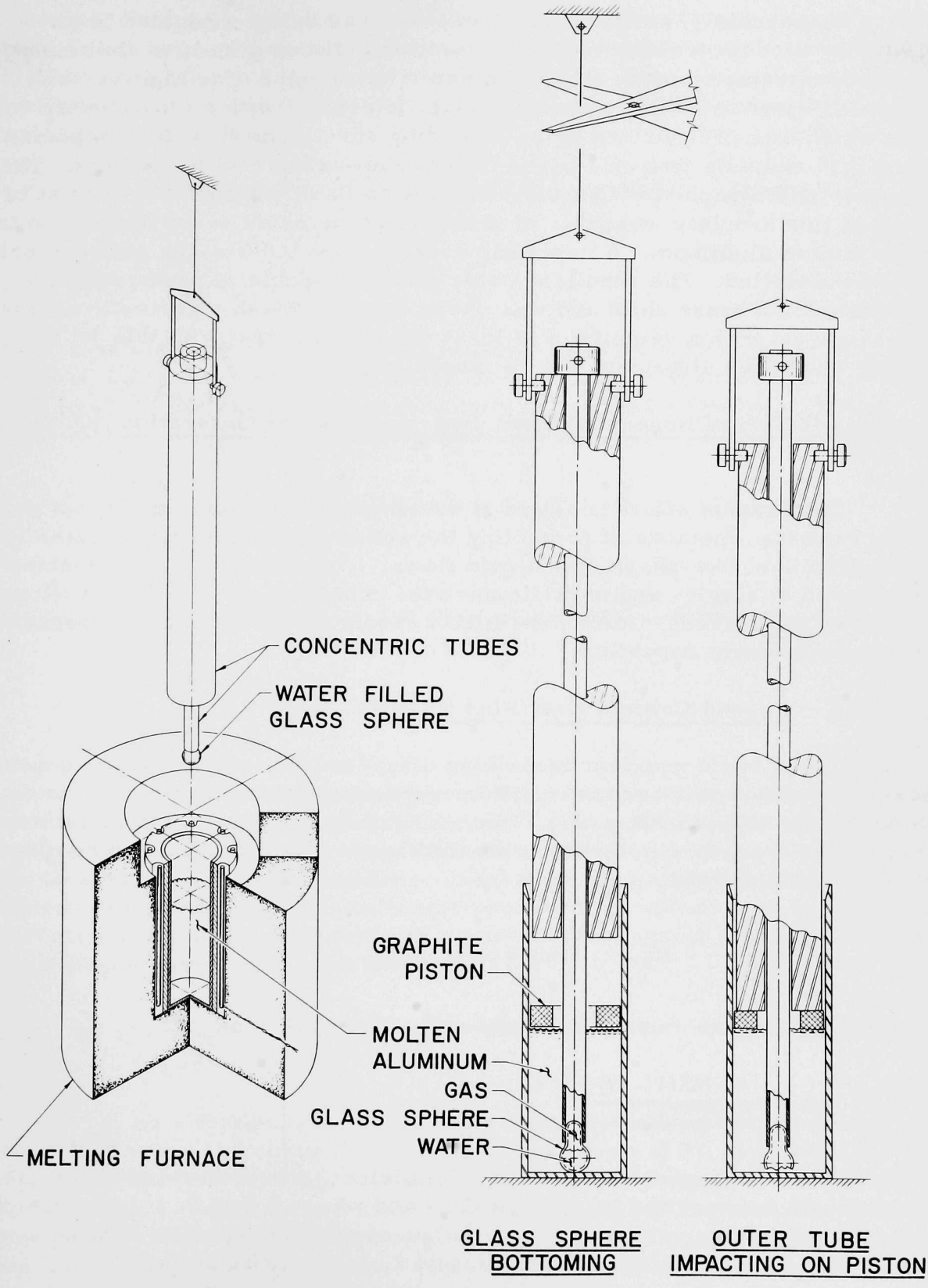

Fig. I.1. Experimental Apparatus for Aluminum–Water Interactions. ANL Neg. No. 900–76–76.

Concurrently, another series of tests was being conducted in an attempt to produce a violent surface reaction between a molten-aluminum mass and ultrahigh-speed, small-diameter water jets. The high-velocity water was ejected through an orifice plate in contact with a small water volume, which was pressurized by an exploding wire. The first test impacted seven 0.25-mm-dia jets on a molten-aluminum surface without effect. The jets were photographed with a 0.5-μs-duration flash and found to consist of a spray of fine droplets incapable of penetrating the oxide scum floating on top of the molten aluminum. A new plate with a single 0.5-cm-dia polished orifice was installed. The resultant water jet was capable of penetrating an 0.08-mm-thick brass shim and was shown by microflash pictures to consist of a single jet with a velocity of at least 400 m/s. A test with this jet impacting on molten aluminum will be conducted soon.

B. Investigation of Nonequilibrium, Two-phase Vapor Generation (O. C. Jones, RAS)

The present effort is aimed at developing relatively simple, but physically realistic, methods of predicting the actual vapor-generation rates in nonequilibrium, two-phase, gas-liquid flows. These methods are required to be included in single- and multidimensional computer codes being developed as part of the current effort of the NRC aimed at developing an independent safety-assessment capability.

1. Beyond Critical Heat Flux (BCHF)

A basic equation describing dispersed flow, BCHF vapor generation as a first-order, nonlinear, inhomogeneous relaxation process was developed (see ANL-75-58, p. 17). The nonequilibrium component of the total energy was described in terms of the difference between equilibrium and nonequilibrium quality ($x_e - x$), given by

$$x_e \frac{d(x_e - x)}{dx_e} + N_{sr}(x_e - x) = x_e. \tag{1}$$

The nonequilibrium relaxation number, N_{sr}, was given as

$$N_{sr} = \frac{6h_d \Delta\lambda(1 - \alpha)}{\delta G \overline{C_{pv}}(1 - x_c)}, \tag{2}$$

where h_d is the droplet heat-transfer coefficient, α is the void fraction, $\Delta\lambda$ is the length between the location of CHF and where $x = 1.0$, δ is the droplet size, G is the mass velocity, $\overline{C_{pv}}$ is the average vapor specific heat between saturated and superheated conditions, and x_c is the critical quality.

The advantage of Eq. 1 over other current phenomenological methods is its simplicity, providing that a local, nondifferential formulation can be obtained for N_{sr}. It is desirable to keep as much physics as possible

in the correlation or calculation of N_{sr}, but eliminate the differential problems caused by having to account for droplet acceleration, droplet splitting, and additional effective h_d due to droplet holdup. Thus, three of the four simultaneous differential equations normally used by Bennett et al.,[4] for example, are eliminated.

The superheat relaxation number, N_{sr}, can be written as

$$N_{sr} = \frac{3}{2}\left(\frac{n\pi}{6}\right)^{2/3} \frac{k_v D \Delta i_{fg}}{\overline{C_{pv}\varphi}} Nu_\delta (1 - \alpha)^{1/3}, \tag{3}$$

where n is the droplet density, Nu_δ is the droplet Nusselt Number, φ is the heat flux, k_v is the vapor conductivity, D is the tube diameter, and Δi_{fg} is the latent heat. If the initial droplet diameter is half that given by a critical Weber number of 7.5, the initial number density at CHF, n_c, can be determined by

$$n_c = \frac{6(1 - \alpha_c)}{\pi \delta_c^2}. \tag{4}$$

With n_c a constant, the droplet diameter at any downstream location is given by

$$\delta = \delta_c \left(\frac{1 - \alpha}{1 - \alpha_c}\right)^{1/3}. \tag{5}$$

With appropriate formulations for droplet drag and heat transfer, calculated values for N_{sr} can be obtained as approximating the actual values. Due to neglect of droplet acceleration and resultant splitting, and also due to effective increase in time residence and heat transfer from holdup, the calculated values will generally be less than the actual values. An approximate correction for the latter is obtained by dividing the actual relaxation numbers by the Boussinesq number for droplets,

$$B_0 = \frac{G}{\rho_\ell \sqrt{g\delta}}. \tag{6}$$

As a test of this method, the extensive data of Forslund and Rohsenow[5] have been correlated for mass velocities of 95, 175, and 260 kg/m^2-s, pipe diameters of 5.8, 8.2, and 11.7 mm, heat fluxes between 16 and 94 kW/m^2, and equilibrium qualities over 3.0 at 0.17 MPa, including some axially nonuniform heat fluxes of >20% of average. Figure I.2 shows these data correlated with what appears to be quite a bit of scatter. However, these are obtained by differentiation of the actual quality versus equilibrium-quality information of Ref. 5 and will be expected to show considerable scatter. The basic result is that all the data seem to be correlated in a single group, indicating that the appropriate effects of mass velocity, heat flux, and tube size are properly accounted for over the dispersed flow range.

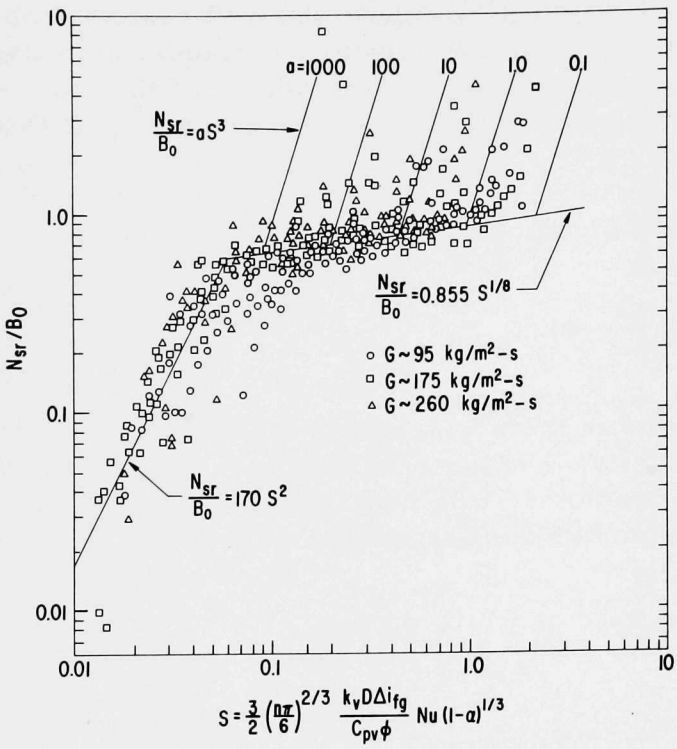

Fig. I.2

Correlation of Superheat Relaxation Number for All Data of Ref. 5

Since the rod-flow regime that sometimes exists between low-quality CHF and the inception of mist flow must be accounted for in starting off a calculation, this region has been empirically correlated as seen in Fig. I.2, where

$$\frac{N_{sr}}{B_0} = aS^3, \tag{7}$$

where

$$a = 2.15 \times 10^{-2}\left[\frac{G}{D\rho_v}\left(\frac{\mu_v}{\rho_v g^2}\right)^{1/3}\right]^{7/2} \exp[-40(0.24 - x_c)], \tag{8}$$

ρ_v and μ_v are the density and viscosity of the vapor, and g is gravitational acceleration. The other regions are described by

$$\frac{N_{sr}}{B_0} = \begin{cases} 170S^2, & S < 0.06; \\ 0.855S^{1/8}, & S \geq 0.06. \end{cases} \tag{9}$$

Figures I.3-I.5 compare the calculated nonequilibrium quality with all the actual values for the three separate mass velocities. This comparison

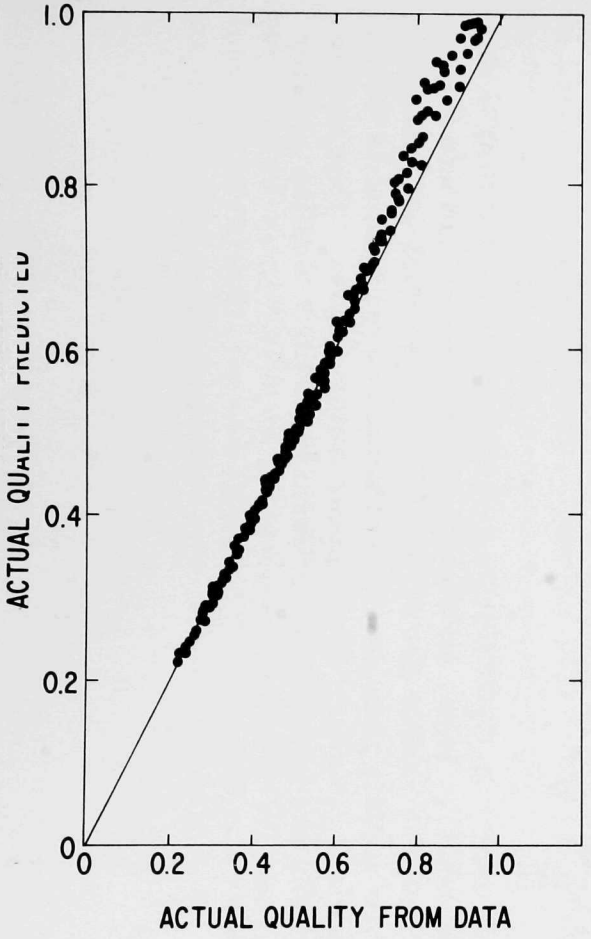

Fig. I.3. Comparison of Calculated Actual Qualities with Those Derived from Ref. 5 at a Mass Velocity of 95 kg/m^2-s

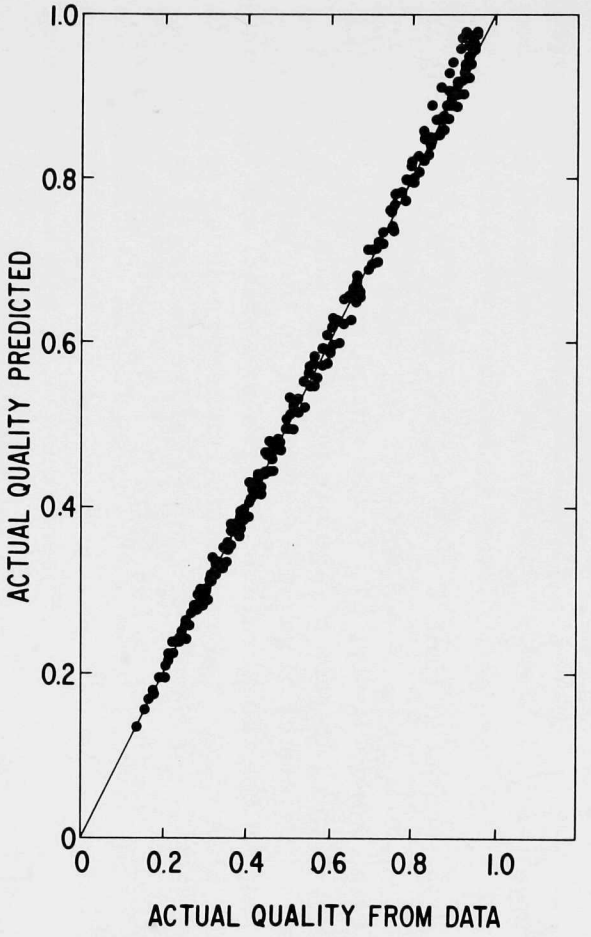

Fig. I.4. Comparison of Calculated Actual Qualities with Those Derived from Ref. 5 at a Mass Velocity of 175 kg/m^2-s

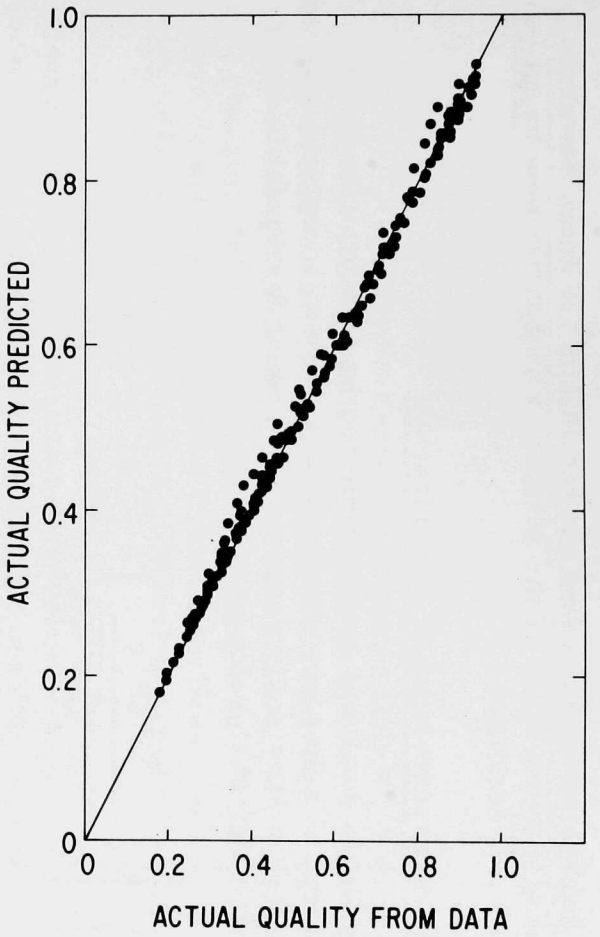

Fig. I.5. Comparison of Calculated Actual Qualities with Those Derived from Ref. 5 at a Mass Velocity of 260 kg/m^2-s

does not validate a correlation. Such was not the intent. It does, however, demonstrate the initial acceptability of the method, which must now be extended to other fluids and conditions.

2. Flashing-pressure Induced Vaporization

Although little work has been completed on this topic in this quarter, the description of spherical bubble growth due to decompression has been extended beyond that previously reported to account for variable vapor density. The general relation developed is

$$R(t) = \left(\frac{\rho_{v0}}{\rho_v}\right)^{1/3}\left[R_0 + \frac{k_s k_\ell \Delta T_s}{\rho_{v0}\Delta i_{fg}\sqrt{\pi\alpha_\ell}}\int_0^t \left(\frac{\rho_{v0}}{\rho_v}\right)^{2/3}\eta^{-1/2}\,d\eta - \ldots\right.$$

$$\left. - \frac{k_s k_\ell}{\rho_{v0}\Delta i_{fg}\sqrt{\pi\alpha_\ell}}\int_0^t \left(\frac{\rho_{v0}}{\rho_v}\right)^{2/3}\int_0^\eta \frac{F'(\zeta)}{(\eta - \zeta)^{1/2}}\,d\zeta\,d\eta\right], \qquad (10)$$

where R(t) is the bubble radius at time t with respect to its initial radius at time zero, R_0 (where $\rho_v = \rho_{v0}$), k_s is a sphericity correction, α_ℓ and k_ℓ are the liquid diffusivity and conductivity, ΔT_s is the initial superheat, and $F'(\zeta)$ is the time derivative of the saturation vapor temperature due to pressure variations. For water, the effect of variable pressure in the integrals of Eq. 10 is small as long as the temperature changes are small and agreement with existing data for both linear and exponential pressure decay is good. If the pressure decays so that the saturation temperature decrease may be described by a generalized power law of the form $T = T_0 - bt^n$, then the size follows the relation

$$R(t) = \left(\frac{\rho_{v0}}{\rho_v}\right)^{1/3}\left[R_0 + \frac{2k_s}{\sqrt{\pi}}\,Ja_T\sqrt{\alpha_\ell t} + \frac{2nk_s S(n)}{\sqrt{\pi}(2n+1)}\,\frac{k_\ell b t^{n+\frac{1}{2}}}{\rho_{v0}\Delta i_{fg}\sqrt{\alpha_\ell}}\right]. \qquad (11)$$

The Jakob number is $Ja_T = \rho_\ell C_\ell \Delta Ts/\rho_{v0}\Delta i_{fg}$, and the coefficient S(n) is dependent on the decay power. Thus, for time long enough to eliminate the effect of initial superheat the radius grows as $t^{n+\frac{1}{2}}$ and the void volume grows as $t^{3(n+\frac{1}{2})}$, much more rapidly than previous theories have indicated. Thus, flashing void fraction and pressure drop appear autocatalytic. That is, the higher the void fraction, the greater the pressure gradient, and the greater the resultant void growth.

C. One-dimensional Drift-flux Modeling; Drift Velocity in Dispersed-flow Regime (M. Ishii)

1. Introduction

A general transient two-phase flow problem can be formulated by using a two-fluid model or a drift-flux model. In the two-fluid model, each phase is considered separately with two sets of conservation equations of mass, momentum, and energy. However, an introduction of two momentum equations in a formulation, as with the two-fluid model, presents considerable difficulties because of mathematical complications and uncertainties in specifying interfacial interaction terms between two phases.

Numerical instabilities caused by improper choice of interfacial interaction terms in the phase-momentum equations are quite common. Therefore, careful studies of the interfacial constitutive equations are required in the two-fluid-model formulation. For example, Réocreux[7] has suggested that, under certain conditions, the interaction terms should include first-order time and spatial derivatives. These difficulties associated with a two-fluid model can be significantly reduced by formulating two-phase problems in terms of the drift-flux model[8] in which the motion of the mixture is expressed by the mixture-momentum equation and the relative motion between phases is taken into account by a kinematic constitutive equation. The drift-flux model is appropriate when the dynamics of two phases are strongly coupled. Consequently, in the drift-flux model, the dynamic interactions between phases of the two-fluid model is replaced by a kinematic relation between the two velocity fields.

Because of its simplicity and applicability to a wide range of two-phase flow systems of practical interest, the drift-flux model is of considerable importance. In particular, the model is useful for thermohydraulic analyses of light-water reactors and liquid-metal-cooled fast breeder reactors under transient and accident conditions.

In the drift-flux model, the relative motion between phases must be specified by a constitutive equation in order to take into account the diffusions of one phase with respect to another. The mixture-momentum equation, together with this kinematic constitutive equation, specifies the motions of each phase. Because of the simplicity of the formulation and numerical analysis, the drift-flux model is useful to many two-phase flow problems encountered in engineering systems.

In view of the practical importance of the drift-flux model for two-phase flow analyses in general and in analyses of nuclear-reactor accidents, in particular, we are studying the kinematic constitutive equation for the drift velocity for dispersed two-phase flow regimes.

2. Drift-flux Model

In two-phase flows, there is always some relative motion of one phase with respect to the other. Therefore, a two-phase flow problem should be formulated in terms of two velocity fields. According to the degree of the dynamic coupling between the phases, two-phase flow problems can be formulated in terms of a two-fluid model or a drift-flux model.[6,8,9] The two-fluid model is formulated in terms of two sets of conservation equations governing the balance of mass, momentum, and energy of each phase. However, the macroscopic fields of one phase are not independent of the other phase. Therefore, interaction terms that couple the transports of mass, momentum, and energy of each phase across the interfaces should appear in the field equations. On the other hand, the drift-flux model (or mixture model) is formulated by considering the mixture as a whole, rather than two phases separately. Therefore, the drift-flux model requires only four field equations, namely, equations of continuity, momentum, and energy for the mixture, and the continuity equation for one of the phases.[8]

In the two-fluid-model formulation, the transport processes of each phase are expressed by their own balance equations. Therefore, the model can probably predict more detailed changes and phase interactions than the drift-flux model. However, this also implies that the two-fluid model is considerably more complicated, not only because of the increased number of field equations and the unknown, but also because of the several necessary constitutive equations. Furthermore, these constitutive equations should be formulated fairly accurately so to offer any meaningful advantage of the two-fluid model over the drift-flux model. This is particularly true as regard to phase-interaction terms that specify the exchange of mass, momentum, and energy at the interfaces. However, accurate constitutive equations for interaction terms under transient conditions are largely unknown. Moreover, the use of existing inaccurate constitutive equations can result in numerical instabilities, since the two-fluid model is inherently unstable due to the Kelvin-Helmholtz instability, unless a proper stabilization mechanism is built into the model through constitutive equations.

The drift-flux model is simpler than the two-fluid model. However, the former requires some drastic constitutive assumptions, since it has only four field equations in contrast to six field equations in the two-fluid model. Therefore, some of the characteristics of two-phase flow will be lost. The simplification introduced by using only four field equations rather than six makes the use of the drift-flux model an attractive and powerful technique for analyzing a number of engineering problems. In particular, the drift-flux model is useful when the information required is the response of the total mixture and not that of each constituent phase separately.

The four field equations in the drift-flux model are the result of the elimination of one energy and one momentum equation from the original

six field equations of the two-fluid model. Therefore, the relative motion and energy difference should be expressed by additional constitutive equations. These two effects inherent to the two-phase flows are taken into account by using a continuity equation for one of the phases and supplementing it with kinematic and phase-change constitutive equations.

The continuity equation of a phase denoted as kth component is given by

$$\frac{\partial \alpha_k \rho_k}{\partial t} + \frac{\partial}{\partial z}(\alpha_k \rho_k v_k) = \Gamma_k \qquad (k = d \text{ or } c), \tag{12}$$

where Γ_k denotes the mass source from the interfaces. The total mass balance across the interfaces requires that

$$\Gamma_c + \Gamma_d = 0, \tag{13}$$

where c and d denote the continuous and dispersed phase, respectively. Therefore by adding the two phase-continuity equations, we obtain the mixture continuity equation given by

$$\frac{\partial \rho_m}{\partial t} + \frac{\partial \rho_m v_m}{\partial z} = 0, \tag{14}$$

where the mixture density is defined by

$$\rho_m \equiv \alpha_d \rho_d + (1 - \alpha_d)\rho_c \tag{15}$$

and the mixture center of mass velocity by

$$v_m \equiv [\alpha_d \rho_d v_d + (1 - \alpha_d)\rho_c v_c]/\rho_m. \tag{16}$$

On the other hand, the velocity of the center of volume of the mixture, i.e., the total volumetric flux, is defined by

$$j \equiv \alpha_d v_d + (1 - \alpha_d)v_c. \tag{17}$$

The drift velocity of a dispersed phase V_{dj} is the velocity of the dispersed phase with respect to the volume center of the mixture. Therefore,

$$V_{dj} \equiv v_d - j = (1 - \alpha_d)(v_d - v_c) = (1 - \alpha_d)v_r, \tag{18}$$

where v_r is the relative velocity between phases. The advantage of using the drift velocity is apparent for dispersed two-phase systems, since it can be

easily related to a rise velocity of bubbles or a terminal velocity of particles or drops. From the definitions of various velocity fields,

$$v_d = v_m + \frac{\rho_c}{\rho_m} V_{dj}. \tag{19}$$

By substituting Eq. 19 into the dispersed-phase-continuity equation, Eq. 12, we obtain

$$\frac{\partial \alpha_d \rho_d}{\partial t} + \frac{\partial}{\partial z}(\alpha_d \rho_d v_m) = \Gamma_d - \frac{\partial}{\partial z}\left(\frac{\alpha_d \rho_d \rho_c}{\rho_m} V_{dj}\right). \tag{20}$$

Since the convective term in the left-hand side of Eq. 20 is expressed by the mixture velocity v_m, an additional diffusion term appears on the right-hand side. Thus, to take into account the effects of the relative motion between phases in the drift-flux model, the drift velocity should be specified. This kinematic constitutive equation may be formulated in a functional form as

$$V_{dj} = V_{dj}(\alpha_d, p, g, v_m, \ldots) \tag{21}$$

This constitutive equation replaces one of the phase-momentum equations of the two-fluid model formulation. To take into account the mass transfer across the interfaces, a constitutive equation for Γ_d should also be given.

The drift velocity in the drift-flux model plays a role similar to that of the diffusion coefficient in a single-phase, two-component system. However, the application of a diffusion coefficient is useful only when the relative motion between components or phases is due to a concentration gradient and can be expressed by a linear constitutive law. For general two-phase flow systems, Fick's law of diffusion may not hold, since in this case the interfacial geometry, the body force field, and the interfacial momentum transfer are the factors governing the relative motion of phases. In other words, the diffusion of phases in two-phase systems is macroscopic, whereas in single-phase two-component systems, it is due to the microscopic molecular diffusion.

The constitutive equation for the drift velocity can therefore be expected to depend strongly on the two-phase flow regimes, since the momentum transfer between the phase is governed by the geometry of the interfaces as well as by the interfacial area concentration. The constitutive equation for the vapor-drift velocity for bubbly and slug flow regimes has been studied by Zuber et al.[10-12] by balancing the gravity force with the drag force. The analysis of the drift velocity in two-phase annular flows has been completed and reported in the previous quarterly progress report (ANL-75-72). The present study is an extension of the above analyses based on the concept of the mixture viscosity.

3. Relative Motion in Single-particle System

A motion of the single solid particles, drops, or bubbles in an infinite medium has been studied extensively in the past. In what follows we shall summarize these results in simple forms useful for the development of the drift constitutive equation in multiparticle systems.

If the relative velocity of a single particle in an infinite medium is denoted by $v_{r\infty} = v_d - v_{c\infty}$, the drag coefficient is defined by $C_{D\infty} \equiv -2F_D/(\rho_c v_{r\infty}|v_{r\infty}|\pi r^2)$, where F_D is the drag force and r is the radius of a particle. On the other hand, the pressure and body force acting on the particle is given by

$$F_p + F_g = \tfrac{4}{3}\pi r^3(\rho_c - \rho_d)g, \tag{22}$$

which should be balanced by the drag force. Hence, $F_p + F_g + F_D = 0$. By introducing the nondimensional parameters[13] for the velocity fields and radius given by $v^* \equiv |v|[\rho_c^2/(\mu_c g\Delta\rho)]^{1/3}$ and $r^* \equiv r(\rho_c g\Delta\rho/\mu_c^2)^{1/3}$, we can solve the force balance for the radius as

$$r^* = \tfrac{3}{8}C_{D\infty}v_{r\infty}^{*2}. \tag{23}$$

The standard particle Reynolds number and the viscosity number are defined by

$$\left.\begin{aligned} N_{Re\infty} &\equiv \frac{2r\rho_c|v_{r\infty}|}{\mu_c} = 2r^*v_{r\infty}^* \\ N_\mu &\equiv \mu_c\Big/\left(\rho_c\sigma\sqrt{\frac{\sigma}{g\Delta\rho}}\right)^{1/2} \end{aligned}\right\}. \tag{24}$$

Extensive studies on the single-particle drag show that in general the drag coefficient is a function of the Reynolds number. However, the exact functional form depends on whether the particle is a solid particle, drop, or bubble.

For viscous regime, the function $C_{D\infty}$ is uniquely given by

$$C_{D\infty} = \frac{24}{N_{Re\infty}}(1 + 0.1N_{Re\infty}^{0.75}). \tag{25}$$

For solid particles, the drag coefficient becomes essentially constant at about $C_{D\infty} = 0.45$ for $N_{Re\infty} \geq 1000$. This Newton's regime holds up to $N_{Re\infty} = 2 \times 10^5$.

For fluid particles such as drops or bubbles, we have a flow regime characterized by the distortion of particle shapes and irregular motions. In this distorted-fluid-particle regime, the drag coefficient increases with the Reynolds number (or with the particle size). Thus,

$$C_{D\infty} = \frac{4}{3} N_\mu^{2/3} r^* \qquad \left(\text{or } \frac{\sqrt{2}}{3} N_\mu N_{Re\infty}\right) \tag{26}$$

for $N_\mu \geq 36\sqrt{2}\,(1 + 0.1 N_{Re\infty}^{0.75})/N_{Re\infty}^2$. As the size of bubbles further increases, the bubbles become spherical-cap-shaped and the drag coefficient reaches a constant value of $C_{D\infty} = 8/3$. The transition from the distorted bubble regime to the spherical-cap bubble regime occurs at about $r^* = 2/N_\mu^{2/3}$. For a liquid drop, the drag coefficient can increase further according to Eq. 26. However, eventually a droplet becomes unstable and disintegrates into smaller drops. This limit can be given by the well-known Weber-number criterion, and it corresponds to $r^* \leq 3/N_\mu^{2/3}$ and $C_{D\infty} \leq 4$. Figure I.6 summarizes the above results on the drag coefficient for single particles of solid, liquid, and gas.

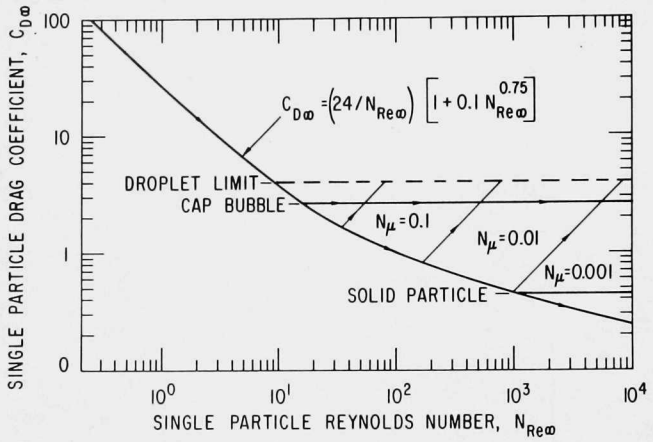

Fig. I.6

Single-particle Drag Coefficient

By knowing the drag law, $C_{D\infty} = C_{D\infty}(N_{Re\infty})$, we can calculate the terminal velocity from Eq. 23. In the viscous regime, the terminal velocity can be approximated by

$$v\, v_{r\infty}^* \simeq \frac{4.86}{r^*}\left[(1 + 0.08 r^{*3})^{4/7} - 1\right]. \tag{27}$$

On the other hand, in the Newton's regime for solid particles, the drag coefficient is constant. Therefore,

$$v_{r\infty}^* = 2.43 r^{*1/2}, \tag{28}$$

which holds for $r^* \geq 34.65$.

For the distorted-fluid-particle regime, the terminal velocity reduces to a constant value of

$$v^*_{r\infty} = \sqrt{2}/N_\mu^{1/3}. \tag{29}$$

Hence, in this regime the relative velocity is independent of the fluid-particle size. Furthermore, for the spherical-cap bubble regime, the terminal velocity becomes

$$v^*_{r\infty} = r^{*1/2}. \tag{30}$$

These results are summarized in Fig. I.7.

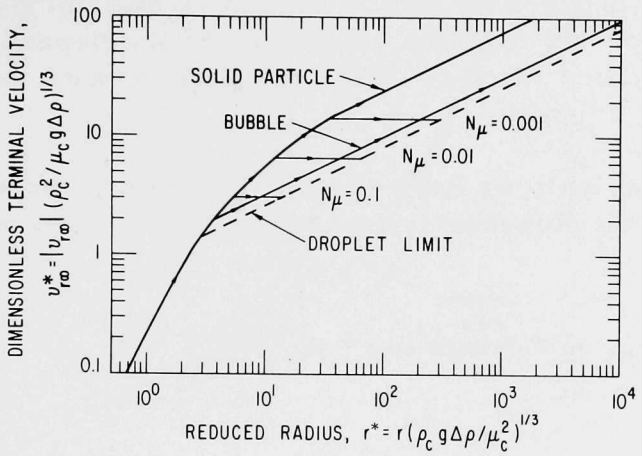

Fig. I.7

Terminal Velocity

4. Multiparticle System in Infinite Media

In multiparticle systems, we must consider the effects of the void fraction on the pressure gradient and on the drag law. The momentum equation for the kth phase can be written as

$$\alpha_k \rho_k \left(\frac{\partial v_k}{\partial t} + v_k \frac{\partial v_k}{\partial z} \right) = \alpha_k \left(-\rho_k g - f_{kw} + f_{ki} - \frac{\partial p}{\partial z} \right), \tag{31}$$

where f_{kw} and f_{ki} are the wall shear force and the interfacial force, respectively. By considering the steady-state condition without phase changes, we obtain

$$\frac{\partial p}{\partial z} = -\rho_m g - (1 - \alpha_d) f_{cw}. \tag{32}$$

Since the effect of the wall can be neglected for a system in an infinite medium, we have $dp/dz = -\rho_m g$.

By introducing the drag coefficient C_D for the multiparticle system based on the relative velocity, we can express the radius of particles by

$$r^* = \frac{3}{8} C_D \frac{v_r^{*2}}{1 - \alpha_d}, \tag{33}$$

which corresponds to Eq. 23 of a single-particle system. Now, for convenience, we define $B \equiv v_r^*/v_{r\infty}^*$ for particles with same r^*. Then, from Eqs. 23 and 33, we get

$$C_{D\infty}(N_{Re\infty}) = C_D(N_{Re})B^2/(1 - \alpha_d), \tag{34}$$

where the Reynolds number is given by $N_{Re} = 2r\rho_c|v_r|/\mu_m$ and μ_m is the mixture viscosity. If we know the mixture viscosity and the dependence of C_D on N_{Re}, Eq. 34 can be solved for B to obtain the slip velocity in terms of the single-particle terminal velocity.

In the present analysis we have extended Taylor's correlation for the mixture viscosity along the Roscoe-type power relation based on the maximum packing α_{dm}. Thus,

$$\frac{\mu_m}{\mu_c} = \left(1 - \frac{\alpha_d}{\alpha_{dm}}\right)^{-2.5\alpha_{dm}(\mu_d + 0.4\mu_c)/(\mu_d + \mu_c)}. \tag{35}$$

The maximum packing α_{dm} for solid or liquid particle systems ranges from 0.5 to 0.74. However, $\alpha_{dm} = 0.62$ suffices for most of the practical cases. For a bubbly flow, α_{dm} can be much higher. Therefore, by considering the standard range of interest of the void fraction, we may take $\alpha_{dm} \simeq 1$.

Figure I.8 compares the present mixture viscosity to the various existing model for solid-particle systems. By including the effect of the viscosity of the dispersed phase in the correlation, the newly developed model has the advantage over the conventional correlations, because it is not limited to particulate flows but can also be applied to droplet and bubbly flows.

Now let us assume that in the viscous regime a complete similarity exists between $C_{D\infty}$ based on $N_{Re\infty}$ and C_D based on N_{Re}, so that $C_D(N_{Re}) = C_{D\infty}(N_{Re})$. Then from Eq. 34, we obtain

$$B \doteq (1 - \alpha_d)^{1/2} f(\alpha_d) \frac{1 + 0.1N_{Re\infty}^{0.75}}{1 + 0.1N_{Re\infty}^{0.75}[f(\alpha_d)]^{6/7}}, \tag{36}$$

where $f(\alpha_d) = (1 - \alpha_d)^{1/2}\mu_c/\mu_m$. Consequently, the drift velocity can be given by

$$V_{dj} \doteq v_{r\infty}(1 - \alpha_d)^{1.5} f(\alpha_d) \frac{1 + \psi(r^*)}{1 + \psi(r^*)[f(\alpha_d)]^{6/7}}, \tag{37}$$

where $\psi(r^*) = 0.55[(1 + 0.08r^{*3})^{4/7} - 1]^{0.5}$ for the viscous regime.

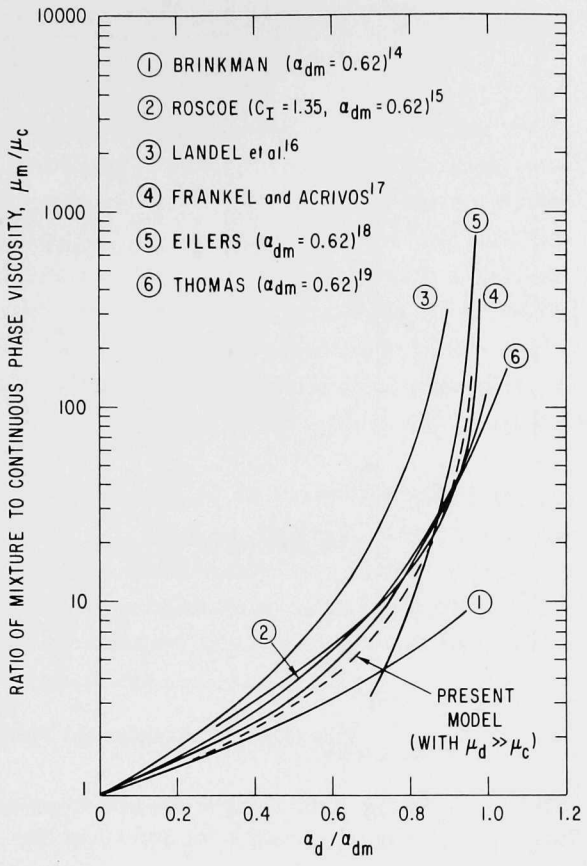

Fig. I.8

Mixture-viscosity Model

For solid-particle systems, we assume that the transition from the viscous regime to the Newton's regime occurs at the same radius as in the single-particle system, and that the drag coefficient C_D is a continuous function. Then, for $r^* \geq 34.65$, we obtain

$$V_{dj} = v_{r\infty}(1 - \alpha_d)^{1.5} f(\alpha_d) \frac{18.67}{1 + 17.67[f(\alpha_d)]^{6/7}}. \tag{38}$$

Figure I.9 compares the above theoretical results given by Eqs. 37 and 38 with the empirical correlation for solid-particlate systems.[20] An agreement at relatively low volumetric concentrations is excellent at all Reynolds-number regions. At very high values of α_d, the present theory predicts much lower drift velocities than the Richardson-Zaki correlation.[20] However, the original experimental data of Richardson and Zaki also indicate this trend, which is predicted by the present theory as shown in Fig. I.10.

In the distorted-fluid-particle regime, we assume that the drag coefficient C_D for a multiparticle system is same as that of a single particle system; i.e., $C_D = (4/3)N_\mu^{2/3} r^*$. Then we obtain

$$V_{dj} = v_{r\infty}(1 - \alpha_d)^{1.5}. \tag{39}$$

This form is identical to the expression given by Zuber and Findley.[9] The above criterion is applicable for $N_\mu \geq 36\sqrt{2}(1 + 0.1N_{Re\infty}^{0.75})/N_{Re\infty}^2$.

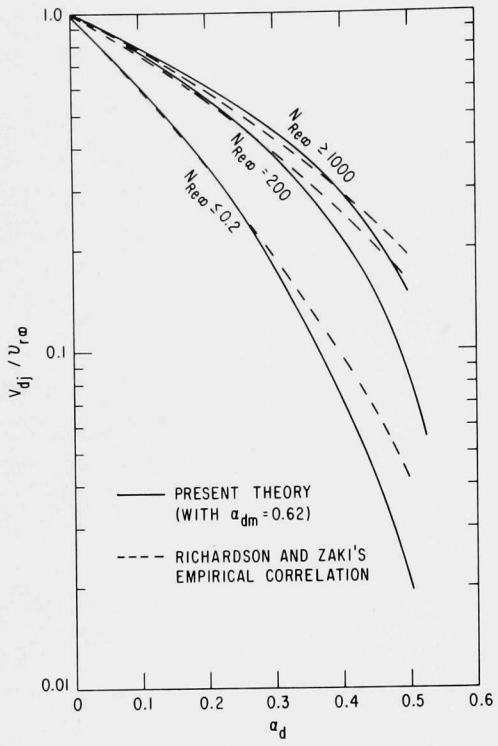

Fig. I.9. Comparison of Predicted Results with Richardson and Zaki's Empirical Correlations for Solid-particulate Flow System

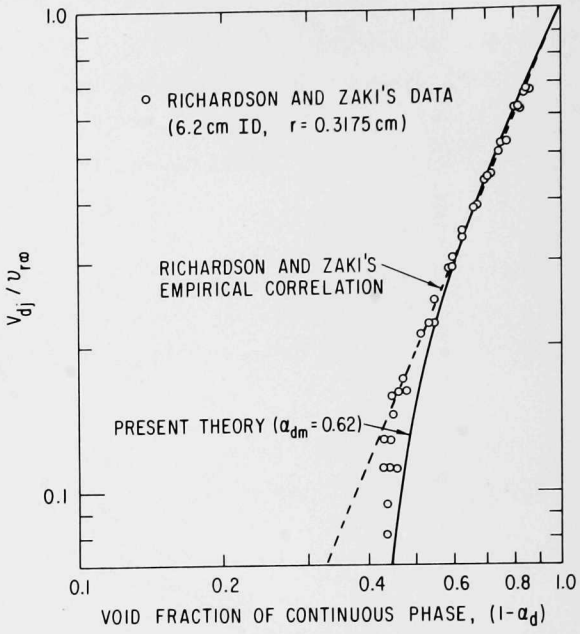

Fig. I.10. Comparison with Experimental Data for Solid Particles

As the radius of the fluid particle is further increased, the wake and bubble boundary layer can overlap due to the formation of the large wake regions. In other words, a particle can influence both the surrounding fluid and other particles directly. Hence the entrainment of a particle in a wake of other particles becomes possible. This flow regime is known as the churn turbulent flow regime and is commonly observed in bubbly flows. In this flow regime, a typical particle moves with respect to the average volumetric flux j rather than the average velocity of a continuous phase. Hence, the reference velocity in the definitions of the drag coefficient and the Reynolds number should be the drift velocity rather than the relative velocity. By assuming that the drag coefficient in the churn-turbulent-flow regime can be given by $C_D = (\sqrt{2}/3)N_\mu N_{Re}$, we obtain

$$V_{dj}^* = \frac{\sqrt{2}}{N_\mu^{1/3}}\left[\frac{\mu_m}{\mu_c}(1 - \alpha_d)\right]^{1/3}. \tag{40}$$

For a churn turbulent bubbly flow, the ratio of the viscosities is given by $\mu_c/\mu_m = 1 - \alpha_d$. Therefore the vapor-drift velocity reduces to

$$V_{dj} = \sqrt{2}\left(\frac{\sigma g \Delta\rho}{\rho_c^2}\right)^{1/4}. \tag{41}$$

This result is consistent with the study by Zuber and Findley[11] for bubbly flows.

D. Spontaneously Generated Heat-flux Crisis (R. E. Henry and J. C. Leung, RAS)

Analyses of current PWR designs show that steady-state operating conditions produce local subcooled boiling within a few coolant subchannels at a system pressure of 15.5 MPa. This corresponds to a wall temperature, including the Jens-Lottes superheat,[21] of 621°K. Additional analyses for a hypothetical, guillotine rupture of an inlet coolant line show that such systems would rapidly depressurize to about 10.8 MPa, which is the saturation pressure corresponding to the upper-plenum temperature. Indeed, this behavior has been experimentally measured in the semiscale MOD-1 experiments,[22-25] which have also measured the very rapid critical heat flux during the blowdown.

This observation is considerably different from those reported by other investigators.[26-28] Consequently, the basic mechanism(s) must be understood before a realistic extrapolation can be made to current PWR designs. Table I.1 illustrates the spontaneous (homogeneous) nucleation rates that would be experienced by surfaces that were in subcooled boiling at 15.5 MPa and depressurized to 10.8 MPa.

TABLE I.1. Homogeneous Nucleation Rates

$$J = A(T)e^{-W/kT}$$

P = 10.8 MPa (1570 psia)

T		P_V				
°F	°K	psia	MPa	σ, n/m	r, Å	J, Sites/cm³-s
660	621.9	2365	16.31	0.00401	14.6	1.5×10^{31}
655	619.1	2286	15.76	0.00454	18.4	5.4×10^{29}
650	616.3	2208	15.23	0.00507	23.1	1.6×10^{27}
645	613.6	2133	14.71	0.00562	28.9	8.6×10^{22}
644	613.0	2118	14.61	0.00573	30.3	4.9×10^{21}
640	610.8	2060	14.20	0.00617	36.6	1.5×10^{15}
635	608.0	1989	13.71	0.00673	46.7	13
630	605.2	1919	13.24	0.00731	60.6	3.2×10^{-26}
625	602.4	1852	12.77	0.00788	81.3	8.7×10^{-82}

Such nucleation rates are certainly significant. Let us assume that a critical-size cavity is about 60 Å in diameter and that these cavities are produced in a liquid layer extending 60 Å from the heater surface. One then finds that, with a nucleation rate of 5×10^{21} sites/cm³-s, nuclei of the critical size physically touch in a square lattice at the critical-size diameter within 1 ms. This results in a vapor blanket along the heater surface. As illustrated in Table I.1, temperatures above 613°C have such nucleation potentials.

If, in addition, the wall is hot enough so that the temperature upon contact between the coolant and the wall results in an interface temperature of

613°K, this vapor blanketing will be sustained because nucleation and coalescence will occur on approximately a millisecond time scale and terminate all significant energy transfer. On the other hand, if such temperature levels are not achieved, efficient cooling will be maintained during the subcooled blowdown portion and the vapor blanketing will result from a quasi-steady condition after several seconds.

An evaluation of the experiments reported in Refs. 27 and 28 shows that their operating conditions were initially 10.3 MPa, and an evaluation of the spontaneous nucleation shows that it is not significant under such initial conditions. A similar analysis of the data in Ref. 26 shows that the system did not experience subcooled boiling under steady-state conditions because of the reduced heat flux. Consequently, temperature levels illustrated in Table I.1 were not achieved.

Figure I.11 compares this mechanism to some of the recent semiscale data. No rapid critical heat flux should be observed in the downstream portion of the heater rods, a rapid and sustained heat-flux crisis should be observed in the central portion, and the lower portion, should see some initial vapor blanketing and a rewet. As shown in Fig. I.11, this is in excellent agreement with the experimental observations.

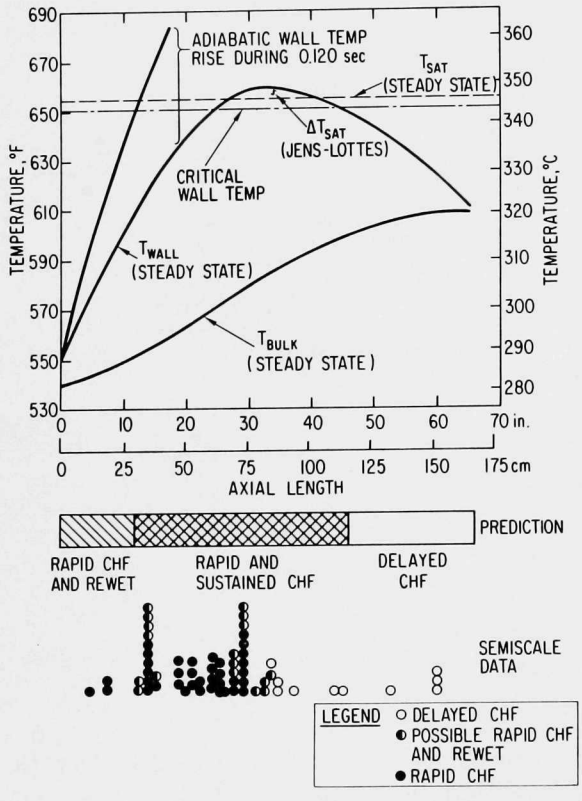

Fig. I.11. Results of Semiscale Test S-02-7. Predicted and measured location of a rapid and sustained heat-flux crisis. ANL Neg. No. 900-76-91.

This model presents a firm physical basis for interpreting available experimental results and extrapolation to the behavior of pressurized-water-reactor systems.

E. Transient Critical Heat Flux (J. C. Leung, R. E. Henry, and O. C. Jones, RAS)

1. Modification of Test Loop

In the earlier version of the test-loop design,[29] the blowdown vessel was installed with only one flexible tube joining the flowing loop and as a result, the fluid, Freon-11, had to be stored in a stagnant condition. Attempting to maintain the same fluid temperature inside the blowdown vessel and the rest of the flowing loop was difficult. As a result of the large thermal capacity of the vessel, the stagnant fluid was at a lower temperature in adiabatic Run 4/9B

reported.[30] This earlier version was subsequently modified to the present design, which is shown in Fig. I.12. Continuous fluid flow inside the blowdown vessel was allowed during the initial steady-state operation.

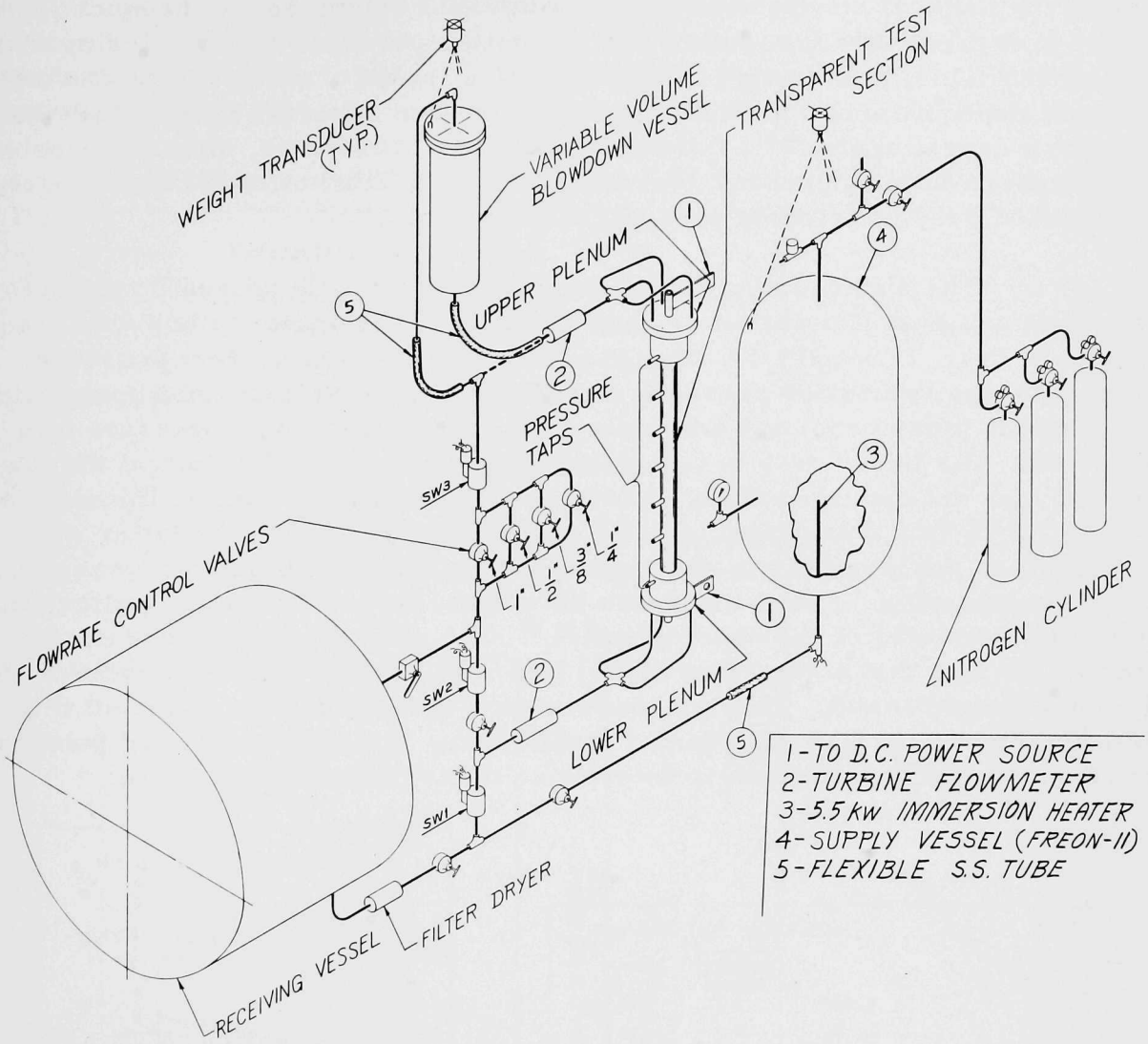

Fig. I.12. Test loop for Transient-blowdown Critical Heat Flux. ANL Neg. No. 900-4557 Rev. 1.

During the earlier diabatic blowdown tests [Runs 4/22,[31] 5/19,[30] and 5/29 (Ref. 31)], the three air-operated solenoid valves (SW1, SW2, and SW3) did not close or open at the same time. To minimize this effect, small globe valves were used to meter the airflow to individual solenoid valves. This allowed a finer tuning of the system response and produced repeatable and satisfactory operation.

2. Effect of Bubble Growth in the Decompression Process

The bubble growth rate has been found to affect the initial decompression characteristic.[32] This is understandable, since the system pressure

would decrease immediately to the ambient pressure if it were not for vaporization of the hot liquid. For adiabatic blowdown, nucleation sites in the form of surface cavities are activated as a result of decompression. With Freon-11 at operating temperatures and pressures, the bubble growth rate is essentially limited by the heat conduction to the liquid/vapor interface. Consequently, the actual pressure must drop below the saturation pressure value, causing some superheat. This phenomenon of bubble nucleation as a result of the thermodynamic nonequilibrium state of the fluid has been reported in other adiabatic blowdown experiments.[32,33] But for the diabatic blowdowns, where subcooled bubbles were initally present, thermodynamic equilibrium was more closely approached during the early phase of the blowdown.

The different characteristics associated with adiabatic and diabatic blowdown are best illustrated by showing the system pressure and void fraction as in Figs. I.13 and I.14. For the diabatic case, the system pressure dropped to the saturation pressure corresponding to the exit fluid temperature in the upper plenum; for the adiabatic case, an undershoot in pressure was observed. The initial rise in calculated equilibrium void fraction at the lower channel was not experimentally observed in the adiabatic run; an immediate jump to ~90% void was characteristic of the diabatic case. The latter was attributed to the large vapor generation during flow reversal accompanying the decompression. For the diabatic blowdown, thermodynamic equilibrium void was estimated at the upper channel.[30] The prediction was encouraging in view of the fact that a slug-flow model had been used in the interpretation of the void measurement. This reasonably good agreement was expected if the system approached thermodynamic equilibrium. Existing subcooled bubbles acted as nucleation sites where interphase mass transfer took place.

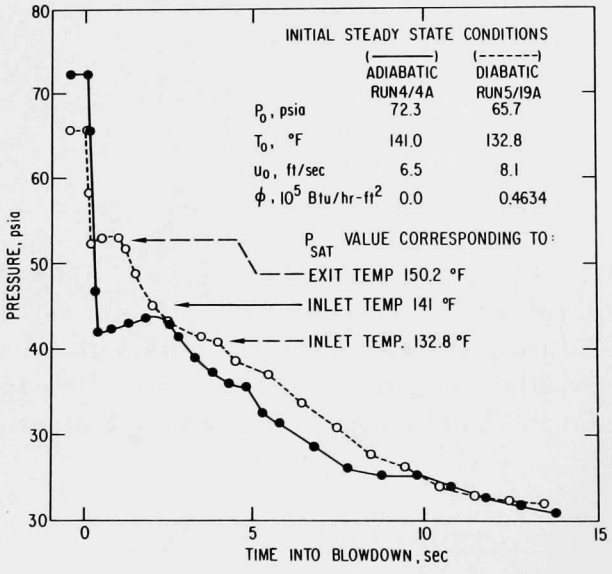

Fig. I.13. Pressure History for Adiabatic and Diabatic Blowdowns. ANL Neg. No. 900-75-423 Rev. 1.

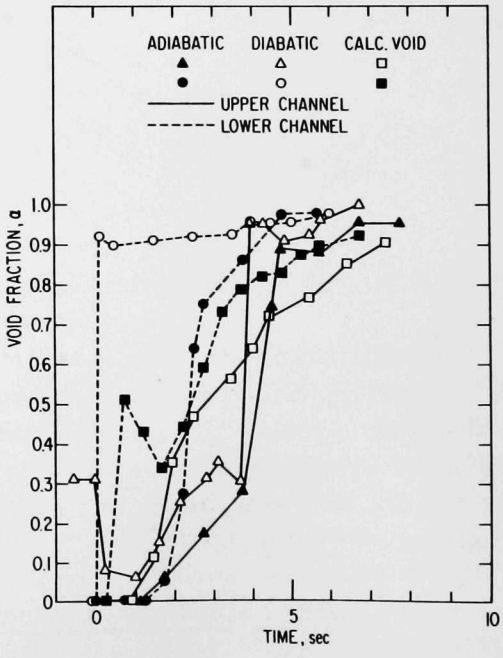

Fig. I.14. Void-fraction Measurements for Adiabatic and Diabatic Blowdowns. ANL Neg. No. 900-75-421.

3. Diabatic Blowdown Tests with High-speed Photography

Three tests (Runs 6/4, 6/9, and 6/12) were conducted with high-speed movies (800-1000 frames per s) of the bottom 6 in. of the heated channel. Since this series of tests was aimed at studying the effect of blowdown volume on time to CHF, the initial steady-state conditions were maintained reasonably constant, as shown in Table I.2. The results of these three blowdown tests are presented in Figs. I.15-I.31. High-speed photographic results are also shown

TABLE I.2. Initial Steady-state Conditions in Test Section before Blowdown

Run No.	Pressure, P_0, psia	Temperature, T_0, °F	Subcooling, ΔT_{sub}, °F	Velocity in TS, u_0, ft/s	Mass Velocity, G, $lb_m/hr\text{-}ft^2$	Heat Flux, φ, $Btu/hr\text{-}ft^2$	Blowdown Volume,[a] V_{BD}, ft^3
4/22	67.5	127.1	40.8	3.28	1.04×10^6	38,500	0.080
5/19-A	65.7	132.8	33.2	8.05	2.53×10^6	46,340	0.072
5/29	66.0	132.8	33.5	7.54	2.37×10^6	45,520	0.318
6/4	64.8	132.8	32.2	7.54	2.37×10^6	45,460	0.318
6/9	64.5	133.9	30.7	7.54	2.37×10^6	46,300	0.201
6/12	65.1	133.3	32.0	7.54	2.37×10^6	46,570	0.072

[a]Blowdown volume is defined to be the system volume between the lower plenum and the SW3 valve.

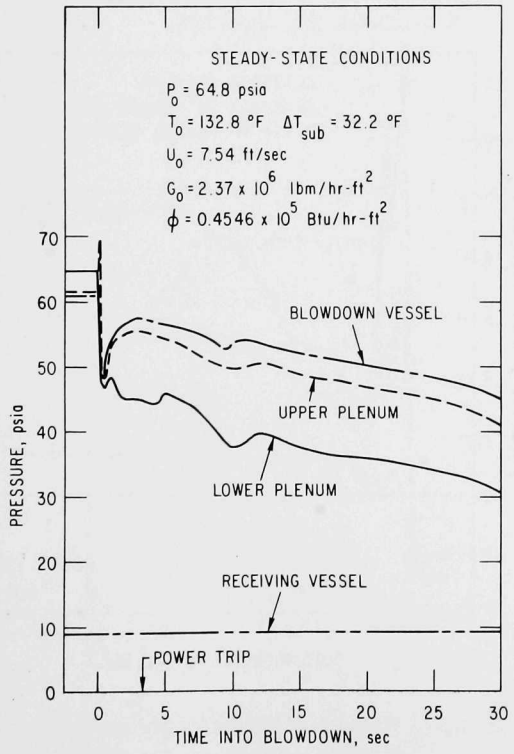

Fig. I.15. Pressure History for Run 6/4. Blowdown volume ≅0.318 ft^3. ANL Neg. No. 900-75-498.

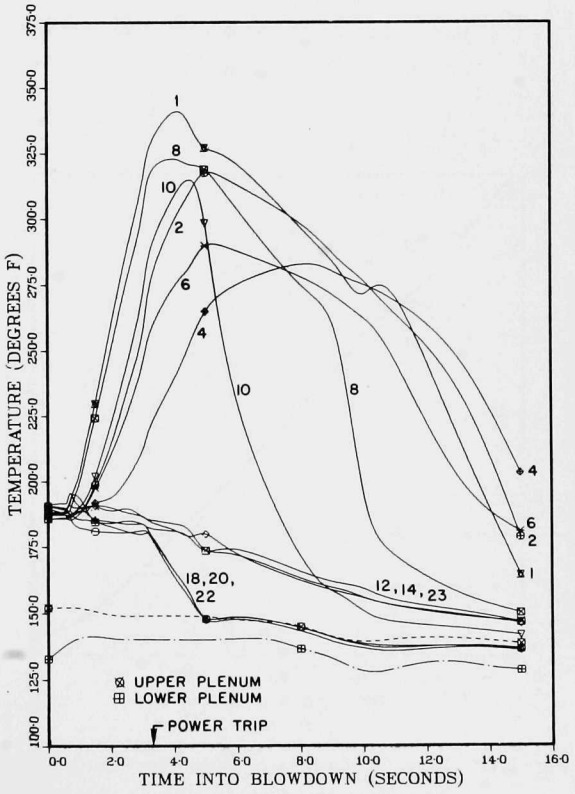

Fig. I.16. Temperature History for Run 6/4. ANL Neg. No. 900-75-804.

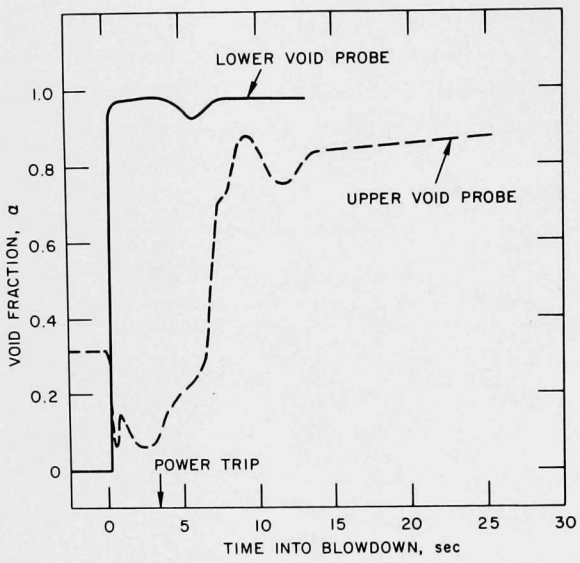

Fig. I.17. Void-fraction Measurement for Run 6/4. ANL Neg. No. 900-75-501.

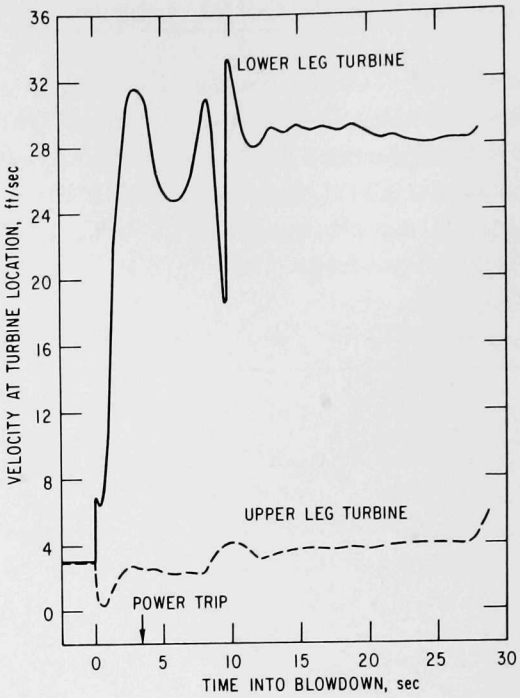

Fig. I.18. Turbine-flow Measurement for Run 6/4. ANL Neg. No. 900-75-500.

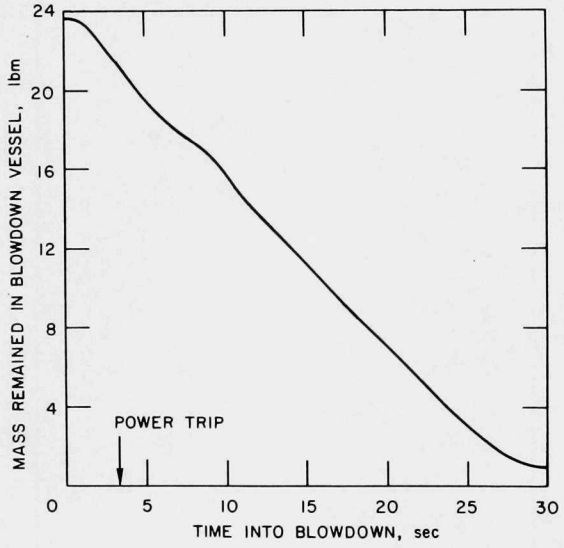

Fig. I.19. Mass in Blowdown Vessel for Run 6/4. ANL Neg. No. 900-75-497.

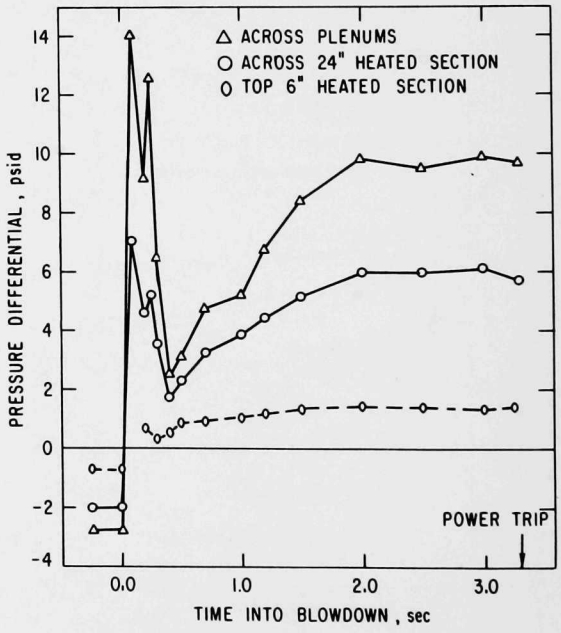

Fig. I.20. Pressure-differential Measurement for Run 6/4. ANL Neg. No. 900-75-921.

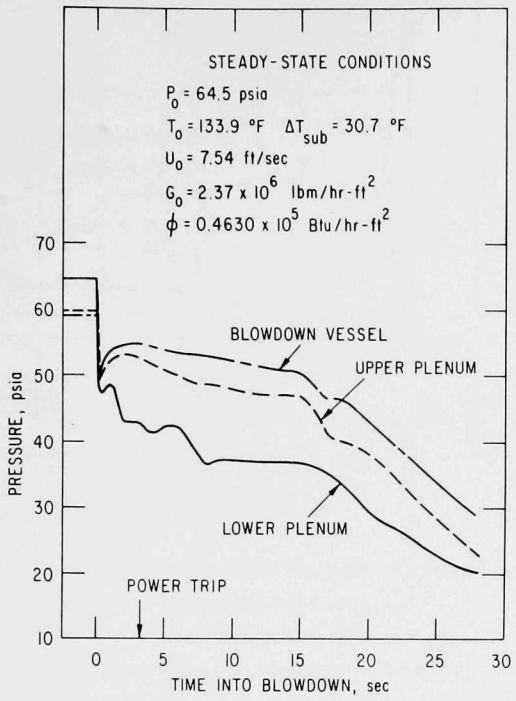

Fig. I.21. Pressure History for Run 6/9. ANL Neg. No. 900-75-495.

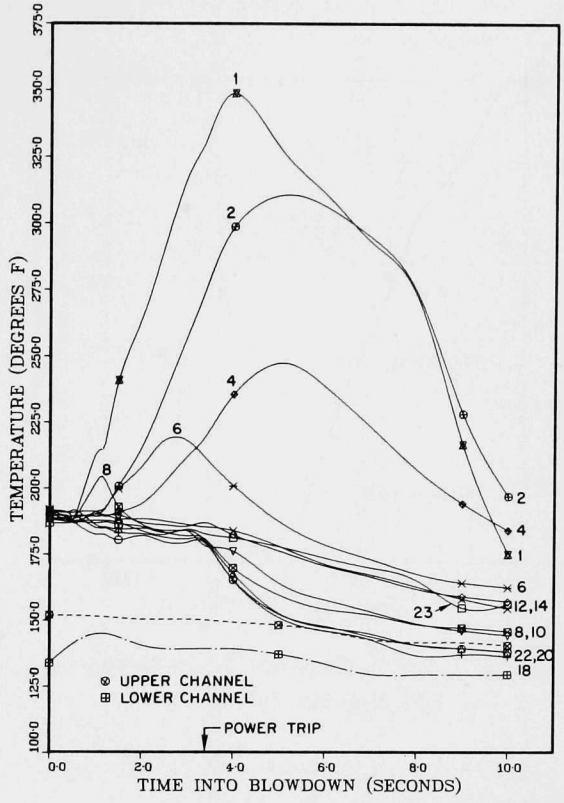

Fig. I.22. Temperature History for Run 6/9. ANL Neg. No. 900-75-803.

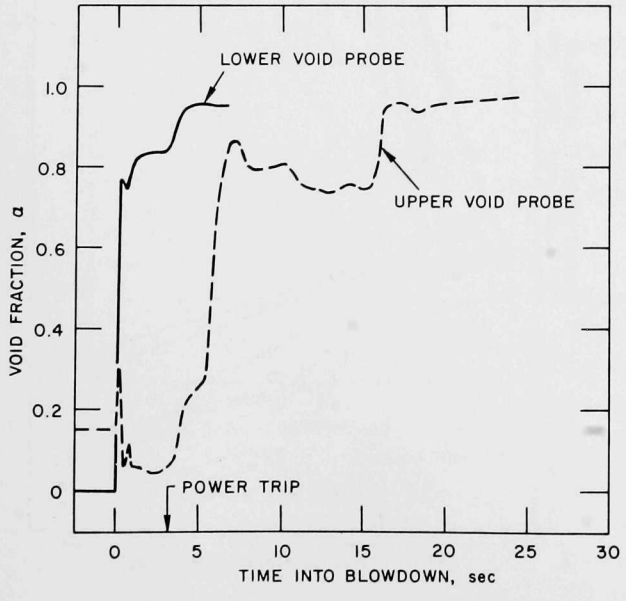

Fig. I.23. Void-fraction Measurement for Run 6/9. ANL Neg. No. 900-75-502.

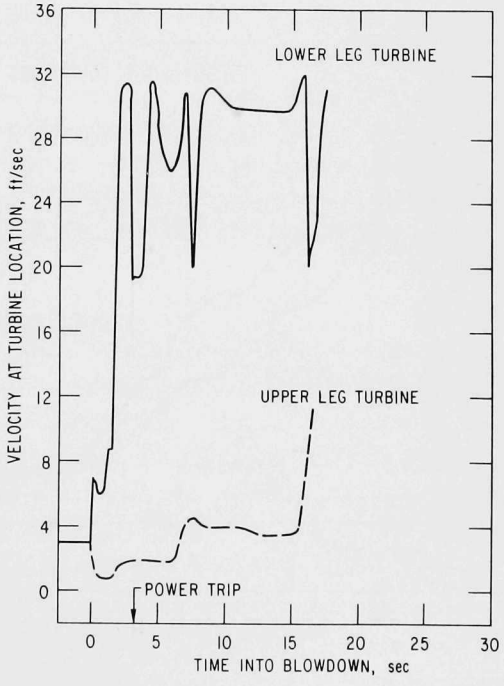

Fig. I.24. Turbine-flow Measurement for Run 6/9. ANL Neg. No. 900-75-499.

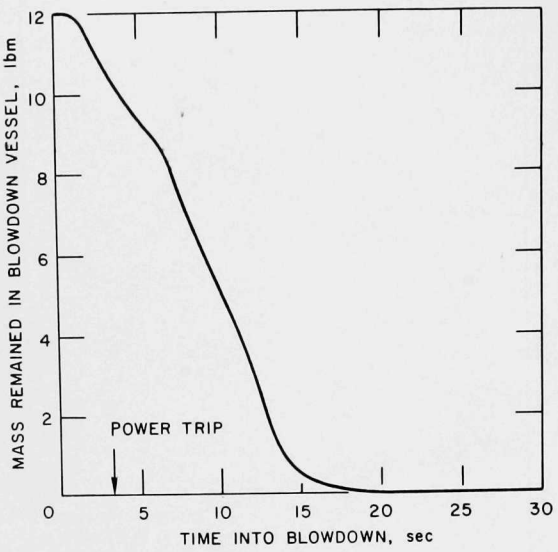

Fig. I.25. Mass in Blowdown Vessel for Run 6/9. ANL Neg. No. 900-75-496.

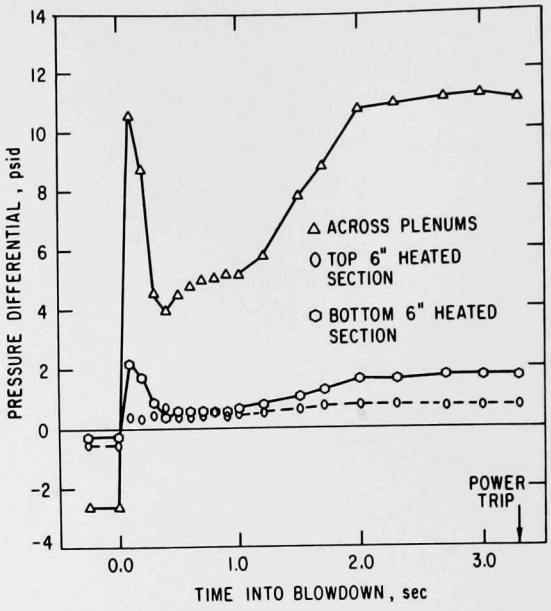

Fig. I.26. Pressure-differential Measurement for Run 6/9. ANL Neg. No. 900-75-920.

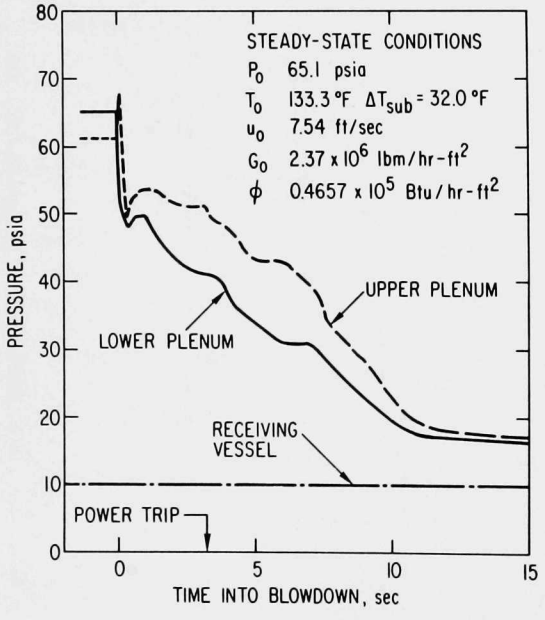

Fig. I.27. Pressure History for Run 6/12. ANL Neg. No. 900-75-416.

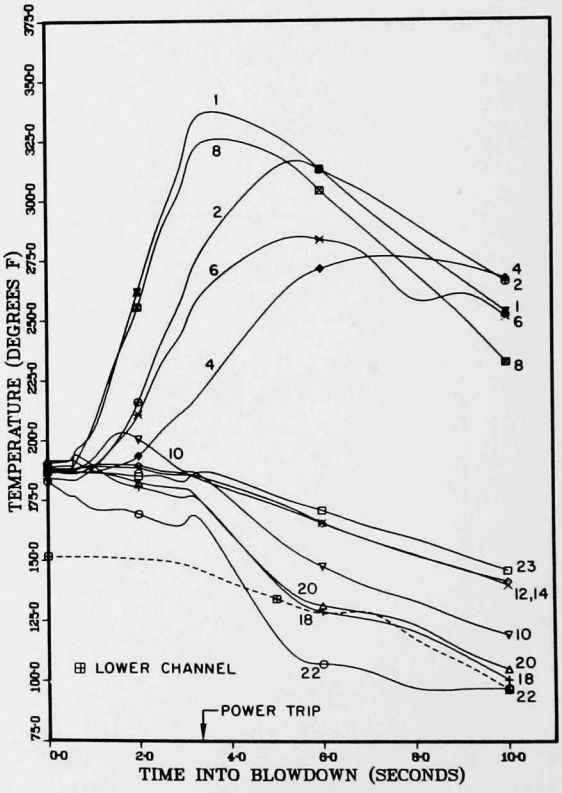

Fig. I.28. Temperature History for Run 6/12. ANL Neg. No. 900-75-802.

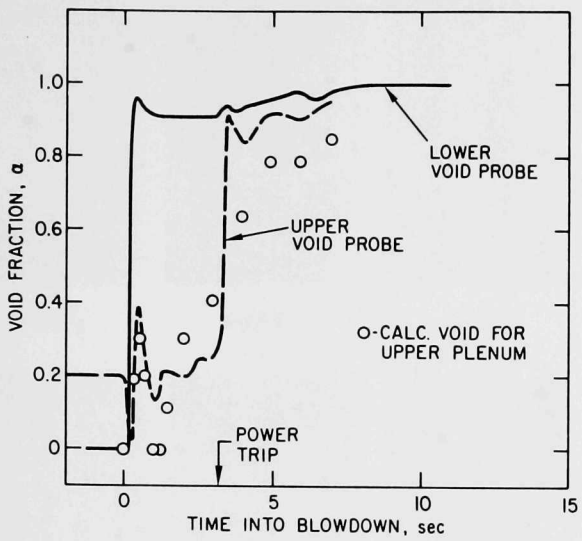

Fig. I.29. Void-fraction Measurement for Run 6/12. ANL Neg. No. 900-75-415.

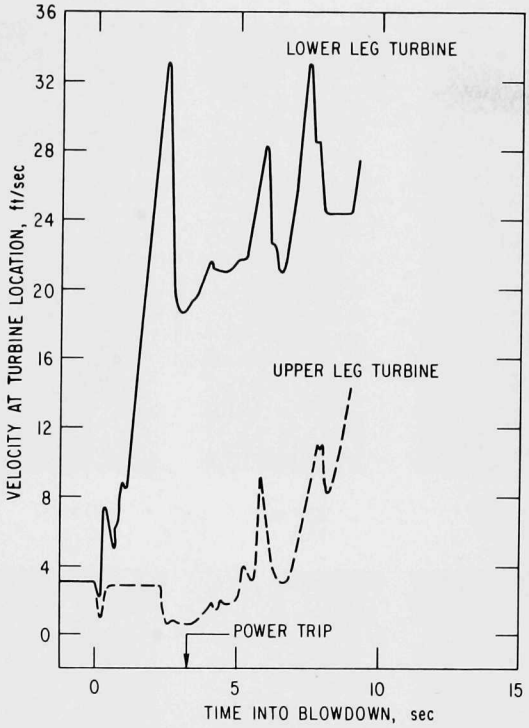

Fig. I.30. Turbine-flow Measurement for Run 6/12. ANL Neg. No. 900-75-494.

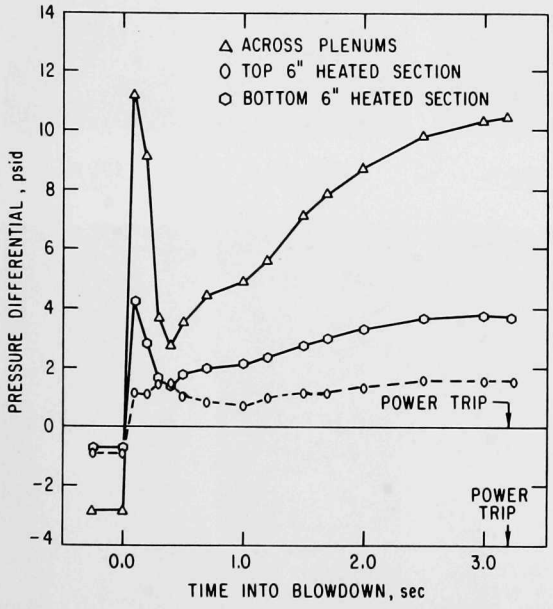

Fig. I.31. Pressure-differential Measurement for Run 6/12. ANL Neg. No. 900-75-922.

as selected prints at various times in Figs. I.32-I.34. The corresponding transient coolant velocities, obtained with a motion picture analyzer, are presented in Figs. I.35-I.37. The velocity shown is more indicative of the liquid phase. CHF was found to occur only at the lower one-third portion of the heated channel and its time was short (~400 ms), as shown in Table I.3.

All three tests showed similar behavior during the early blowdown phase. The flow reversal was observed to last 50-60 ms (see Figs. I.35-I.37), the upflow decayed as soon as depressurization started, and as the flow decayed, the bubble density on the heating surface increased rapidly. Vigorous vaporization occurred during downflow, as seen from prints at 80 ms, and this high void mixture was swept out of the heated channel at an accelerating speed. The lower void probe showed an immediate jump to high void fraction, qualitatively in agreement

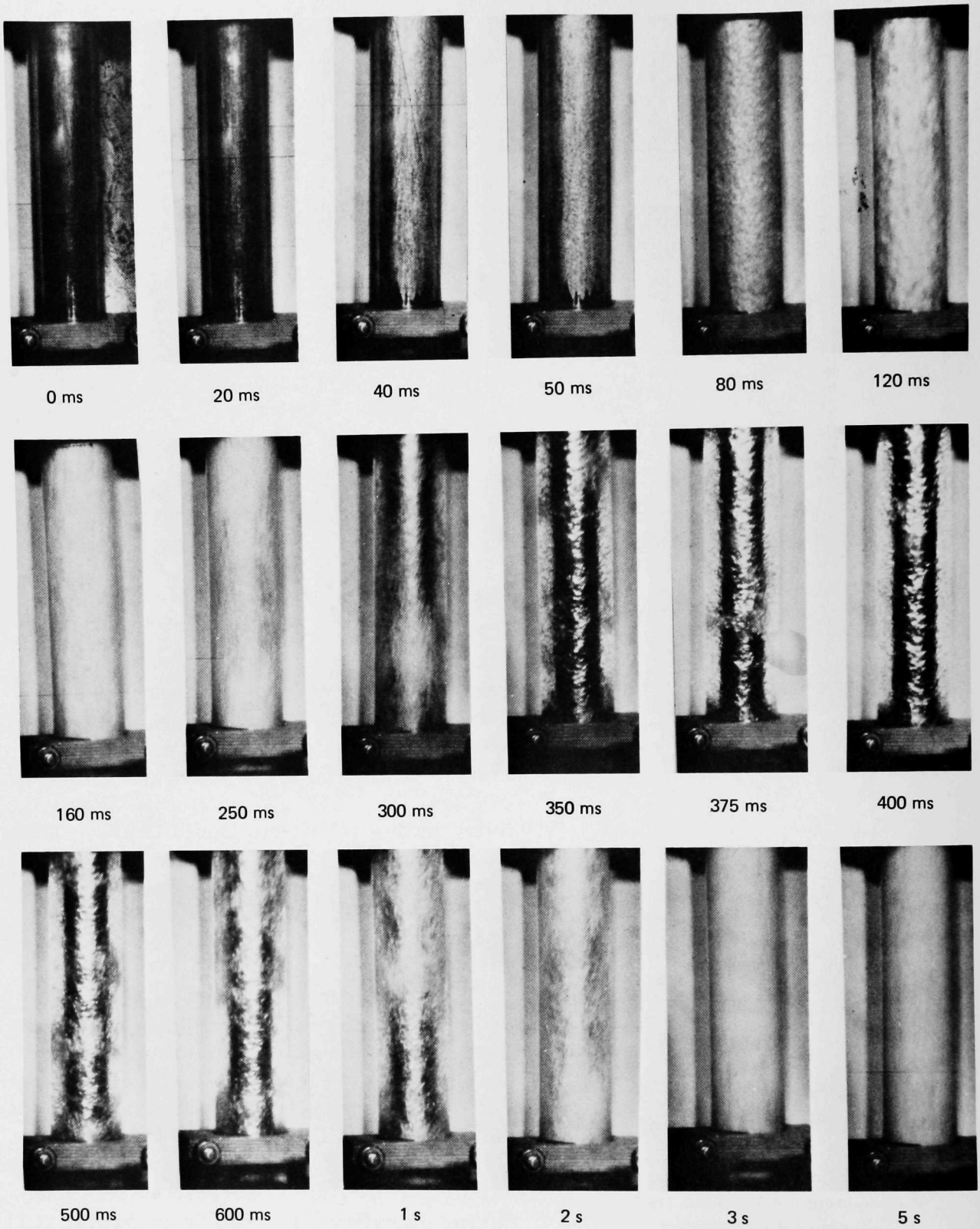

Fig. I.32. Selected Prints for Run 6/4. ANL Neg. No. 900-75-326.

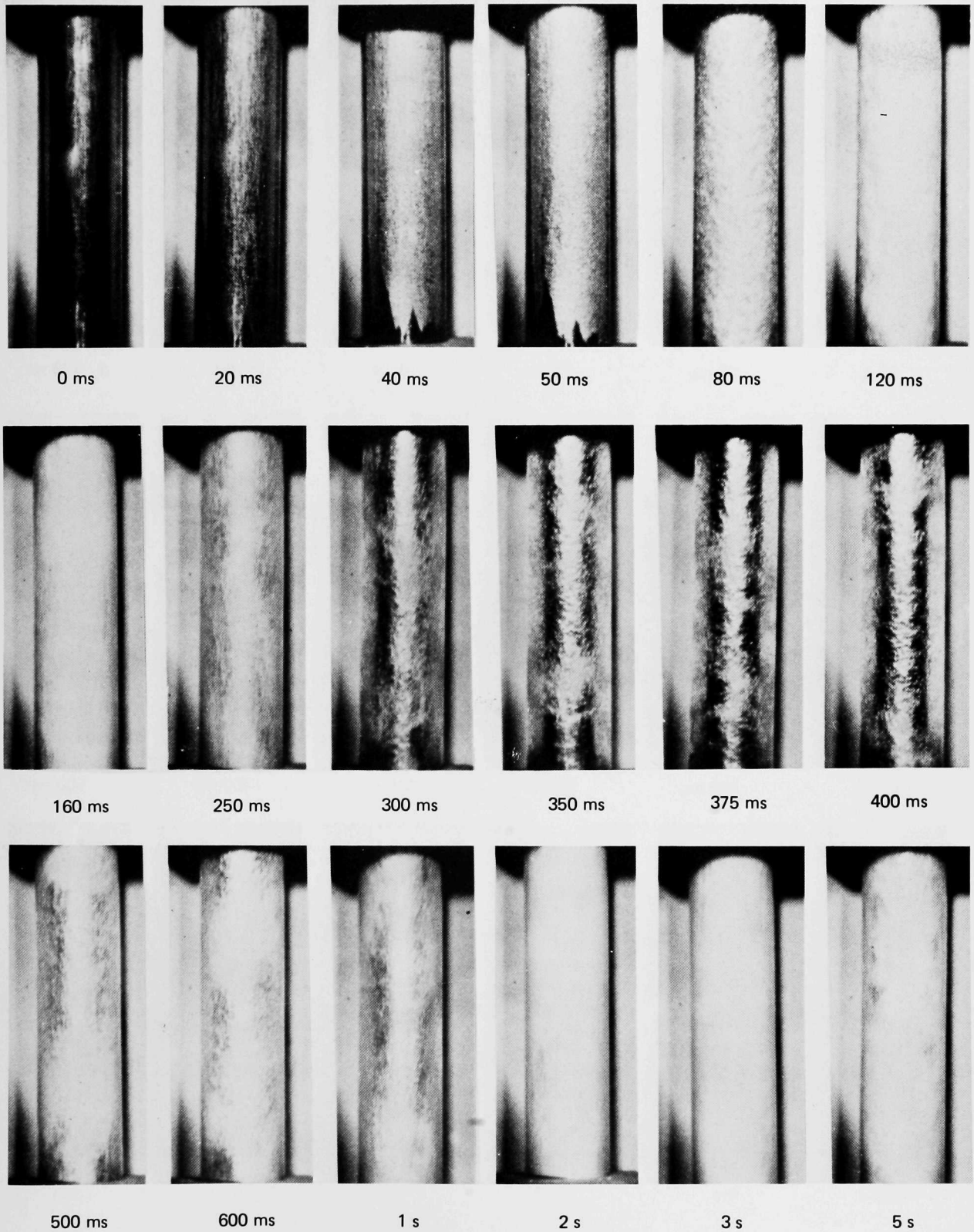

Fig. I.33. Selected Prints for Run 6/9. ANL Neg. No. 900-75-325.

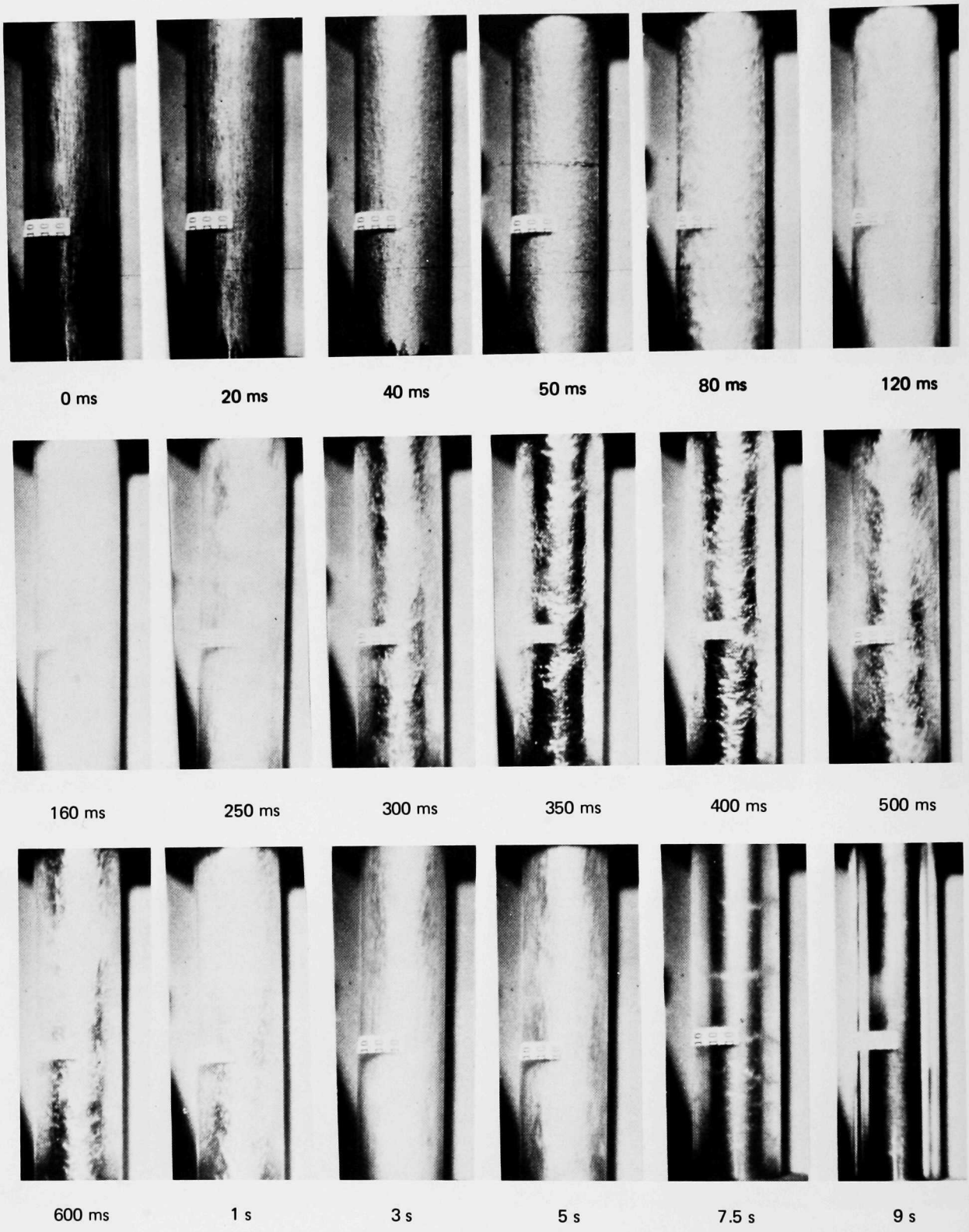

Fig. I.34. Selected Prints for Run 6/12. ANL Neg. No. 900-75-327 Rev. 1.

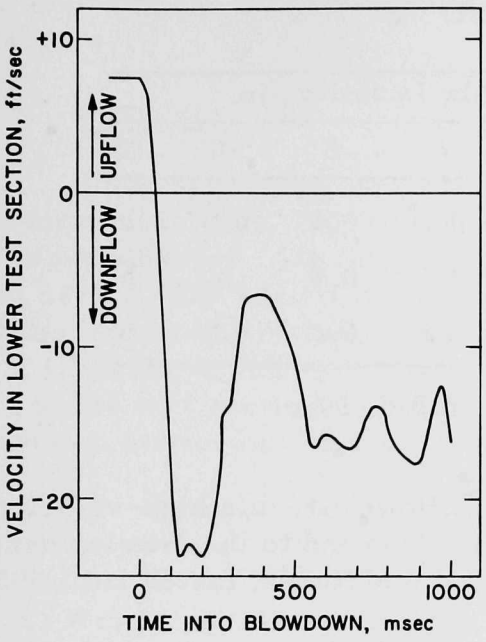

Fig. I.35. Velocity Observed in High-speed Photography of Run 6/4. ANL Neg. No. 900-75-988.

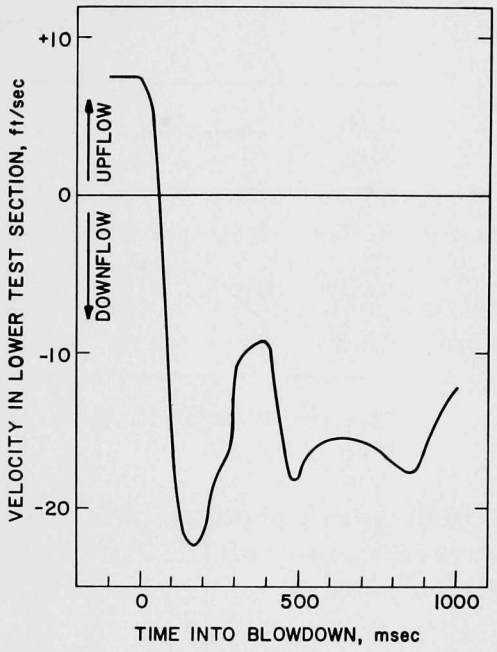

Fig. I.36. Velocity Observed in High-speed Photography of Run 6/9. ANL Neg. No. 900-75-944.

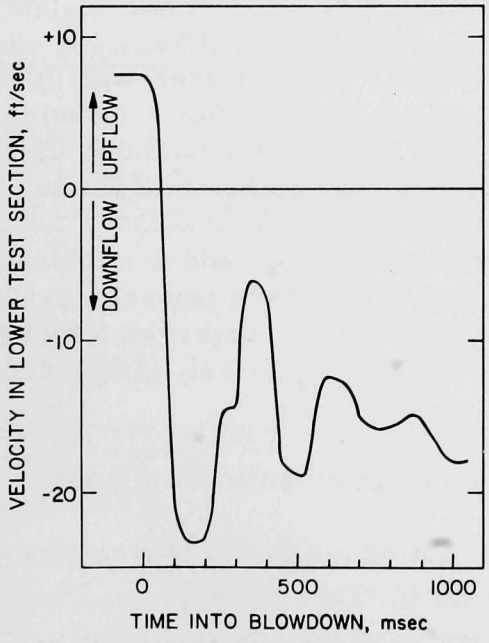

Fig. I.37

Velocity Observed in High-speed Photography of Run 6/12. ANL Neg. No. 900-75-987.

TABLE I.3. Time to CHF[a] (t_{CHF}) for Diabatic Blowdown

Run No.	Time to CHF, s: Thermocouple Location, in.						
	1	2	4	6	8	10	12
6/4	0.4	0.5	0.4	0.5	0.4	0.5	b
6/9	0.3	0.5	0.4	0.5	0.4	b	b
6/12	0.3	0.4	0.4	0.2	0.2	0.3	b

[a] t_{CHF} is defined by Eq. 46 in Ref. 30.
[b] No CHF.

with the high-speed photographic results. However, this high-velocity flow was observed to drop off at about 250 ms. This led to the development of an annular flow pattern, which, judging from the pictures, lasted until 500 ms.

During this period, considerable slip between liquid and vapor phases was observed; roll waves frequently passed along, while smaller droplets traveled down the core at a much higher velocity. Wavy liquid films were observed adhering to the outer unheated wall, although it is uncertain, judging from the motion pictures, whether a liquid film was also present on the heated wall.

According to the thermocouples at the heater-wall location, CHF was experienced with the appearance of the annular flow. Considering the uncertainty in determining the time to CHF, it can be concluded that no difference was observed among these runs with different blowdown volumes.

Note that rewetting took place at the 8- and 6-in. locations in Run 6/9 and at the 10-in. location in Run 6/12 before power trip. It is recommended in future tests that the power-trip circuit be set at a higher temperature to study if the early CHF can be completely rewet, giving rise to another CHF much later in time, as observed in Run 5/29.[31]

To summarize, the following statements are made:

a. Critical heat flux did not occur in the 60-ms flow-reversal period.

b. The first or early CHF occurred at about 400 ms, coinciding with the appearance of an annular flow pattern. This time was independent of the blowdown volume, and its occurrence was restricted to the lower one-third of the heated channel.

c. For some cases the first CHF was rewet, and a second CHF was observed to occur at near depletion of liquid in the test section. Its time, however, was dependent on the blowdown volume.

Planning for future tests is underway. They will include a double-ended break, with the feasibility of bidirectional flow in the heated channel and new test section capable of operating at higher pressures and temperatures.

4. Summary

High-speed photographic results are presented from three diabatic blowdown tests. These and other tests reported previously indicated the following behavior. (1) Critical heat flux did not occur in the 60-ms flow-reversal period. (2) The first CHF occurred at ~400 ms in the lower one-third of the heated channel and its time was independent of the blowdown volume. (3) If the first CHF was rewet, a later CHF would occur at near depletion of liquid in the test section, and the time scale for this event was dependent on the system blowdown volume.

References

1. R. W. Wright, A. F. Fustenberg, G. H. Humberstone, L. G. Neal, L. B. Wentz, and S. M. Zivi, Kinetic Studies of Heterogeneous Water Reactors--Annual Summary Report--1966, STL-372-50 (Dec 1966).

2. P. D. Hess and K. J. Brondyke, Causes of Molten Aluminum Explosions and Their Prevention, Metal Progress 95(4), 93-100 (1969).

3. R. W. Wright and G. H. Humberstone, Dispersal and Pressure Generation by Water Impact Upon Molten Aluminum, Trans. Am. Nucl. Soc. 9, 305-306 (1966).

4. A. W. Bennett, G. F. Hewitt, H. A. Kearsey, and R. F. K. Keeys, Heat Transfer to Steam-Water Mixtures Flowing in Uniformly Heated Tubes in Which the Critical Heat Flux Has Been Exceeded, AERE-R5373 (Oct 1967).

5. R. P. Forslund and W. M. Rohsenow, Thermal Non-Equilibrium in Dispersed Flow Film Boiling in a Vertical Tube, MIT Report 75312-44 (Nov 1966).

6. M. Ishii, Thermo-Fluid Dynamic Theory of Two-Phase Flow, Chapters IX and X, Eyrolles, Paris, Scientific and Medical Publication of France, New York (1975).

7. M. Réocreux, "Contribution à l'étude des débits critiques en éculement diphasique eau vapeur," Ph.D. thesis, University of Grenoble, France (1974).

8. N. Zuber, "Flow Excursions and Oscillations in Boiling, Two-Phase Flow Systems with Heat Addition," Proc. Symp. Two-Phase Flow Dynamics, Vol. 1, p. 1071 (1967).

9. G. Kocamustafaogullari, Thermo-Fluid Dynamics of Separated Two-Phase Flow, Ph.D. thesis, Georgia Institute of Technology, Atlanta (1971).

10. N. Zuber, F. W. Staub, G. Bijwaard, and P. G. Kroeger, Steady State and Transient Void Fraction in Two-Phase Flow Systems, GEAP-5417, Vol. 1 (1967).

11. N. Zuber and J. A. Findley, Average Volumetric Concentration in Two-Phase Flow Systems, J. Heat Transfer 87, 453 (1965).

12. N. Zuber, On the Dispersed Two-Phase Flow on the Laminar Flow Regime, Chem. Eng. Sci. 19, 897 (1964).

13. G. B. Wallis, The Terminal Speed of Single Drops or Bubbles in an Infinite Medium, Int. J. Multiphase Flow 1, 491 (1974).

14. H. Brinkman, Viscosity of Concentrated Suspensions and Solutions, J. Chem. Phys. 20, 571 (1952).

15. R. Roscoe, The Viscosity of Suspensions of Rigid Spheres, Br. J. Appl. Phys. 3, 267 (1952).

16. R. F. Landel, B. G. Moser, and A. J. Bauman, "Rheology of Concentrated Suspensions: Effects of a Surfactant," Proc. 4th Int. Congress on Rheology, Brown University, Part 2, p. 663 (1965).

17. N. A. Frankel and A. Acrivos, On the Viscosity of a Concentrated Suspension of Solid Spheres, Chem, Eng. Sci. 22, 847 (1967).

18. H. Eilers, Kolloid-Z. 97, 313 (1941).

19. D. G. Thomas, Transport Characteristics of Suspension: VIII, J. Colloid Sci. 20, 267 (1965).

20. J. F. Richardson and W. N. Zaki, Sedimentation and Fluidization: Part 1, Trans. Inst. Chem. Eng. 32, 35 (1954).

21. W. H. Jens and P. A. Lottes, Analysis of Heat Transfer, Burnout, Pressure Drop, and Density Data for High Pressure Water, ANL-4627 (1951).

22. H. S. Crapo, M. F. Jensen, and K. E. Sackett, Experiment Data Report for Semi-scale MOD-1 Test S-02-2, ANCR-1232 (1975).

23. H. S. Crapo, M. F. Jensen, and K. E. Sackett, Experiment Data Report for Semi-scale MOD-1 Test S-02-3, ANCR-1233 (1975).

24. H. S. Crapo, M. F. Jensen, and K. E. Sackett, Experiment Data Report for Semi-scale MOD-1 Test S-02-4, ANCR-1234 (1975).

25. H. S. Crapo, M. F. Jensen, and K. E. Sackett, Experiment Data Report for Semi-scale MOD-1 Test S-02-7, ANCR-1237 (1975).

26. R. A. Hedrick, C. D. Morgan, D. H. Roy, R. H. Stoudt, J. S. Gellerstedt, and L. A. Zielke, Analytical and Experimental Investigation of Heat Transfer During Simulation Cold-Leg Blowdown Accidents, paper presented at the CREST Specialist Meeting, Energy Core Coolant for Light Water Reactors, Munich Technical University, Germany (1972).

27. J. D. White, D. L. Clark, R. W. McCulloch, and W. E. Baucum, Fuel Rods Simulation, ORNL-TM-4729, Vol. 1, p. 7 (Dec 1974).

28. C. G. Lawson, Heat Transfer from Electrically Heated Rods During a Simulated Loss-of-Coolant Accident, Chem, Eng. Prog. Symp., Series 119, 67, 1 (1971).

29. J. C. M. Leung and O. C. Jones, "Transient Critical Heat Flux," Light-water-reactor Safety Research Program: Quarterly Progress Report, January-March 1975, ANL-75-28, p. 18 (June 13, 1975).

30. J. C. M. Leung, R. E. Henry, and O. C. Jones, "Transient Critical Heat Flux," Light-water-reactor Safety Research Program: Quarterly Progress Report, April-June 1975, ANL-75-58, p. 27 (Sept 26, 1975).

31. J. C. M. Leung, R. E. Henry, and O. C. Jones, "Transient Critical Heat Flux," Light-water-reactor Safety Research Program: Quarterly Progress Report, July-Sept 1975, ANL-75-72, p. 19 (1975).

32. M. N. Hutcherson, Contribution to the Theory of the Two-Phase Blowdown Phenomenon, ANL-75-82 (Dec 1975).

33. S. Banerjee, W. T. Hancox, R. B. Jeffries, and M. T. Sulatisky, Transient Two-Phase Flow and Heat Transfer During Blowdown from Subcooled Conditions with Heat Addition, 15th National Heat Transfer Conference, San Francisco (Aug 1975).

II. TRANSIENT FUEL RESPONSE AND FISSION-PRODUCT RELEASE PROGRAM

Responsible Group Leaders:
L. A. Neimark and R. B. Poeppel, MSD

Coordinated by:
L. R. Kelman, MSD

A physically realistic description of fuel swelling and fission-product release is needed to aid in predicting the behavior of fuel rods and fission products under certain hypothetical light-water-reactor (LWR) accident conditions. To satisfy this need, a comprehensive computer-based model, the Steady-state and Transient (SST) fuel-element behavior code, is being developed at Argonne National Laboratory (ANL). This model will be incorporated into the Fuel-rod Analysis Program (FRAP) code being developed by the Aerojet Nuclear Company (ANC). The analytical effort is supported by data developed from characterization of irradiated LWR fuel and from out-of-reactor transient heating tests on irradiated commercial LWR fuel under a range of thermal conditions. In the near term, emphasis in the experimental program is being placed on fuel thermal conditions that are applicable to anticipated hypothetical power-coolant-mismatch (PCM) accidents. Later experimental efforts will turn to conditions typical of other types of hypothetical accidents.

The technical status of the program was reviewed in Germantown, Md., on December 8, 1975, by the Water Reactor Safety Research (WRSR) Fission Product Review Group. No changes in scope or direction were recommended by the Group. The following summarizes recent significant analytical and experimental advances and the status of the program at the end of this quarter:

(a) Models for the influence of interconnected porosity and the effect of grain growth on fission-gas behavior have been incorporated into GRASS.

(b) Models for the enhanced diffusivity of fission-gas bubbles on grain boundaries have been incorporated into GRASS.

(c) Initial verification of GRASS Steady-state Modification 2 [GRASS (SS)-Mod 2] has been accomplished by comparison of results with Carolinas-Virginia Tube Reactor (CVTR) data.

(d) Checkout and scoping tests of the in-cell direct-electrical-heating (DEH) equipment were completed, and additional improvements were made in the electronics and temperature-measuring capability.

(e) Interim equipment to recover DEH fuel specimens from irradiated fuel rods has been assembled in the hot cell, and usable quartz-enclosed DEH specimens have been extracted from fuel irradiated in the Carolina Power and Light (CPL) Company H. B. Robinson Pressurized-Water Reactor (PWR).

(f) The capability to subject irradiated fuel pellets to programmed thermal conditions applicable to anticipated hypothetical PCM-type accidents has been demonstrated by successful DEH testing of several specimens from the Robinson fuel rods.

(g) Axial burnup analysis of a Robinson fuel rod has been perfomed.

(h) A matrix for the initial DEH transient test plan has been developed, with conditions applicable to hypothetical PCM-type accidents, to provide experimental correlations and data on fission-gas behavior in and release from transient-heated fuel, which will be of use to model developers. The WRSR Fission Product Review Group has conditionally approved the matrix.

A. Modeling of Fuel-Fission-product Behavior (J. Rest, MSD)

1. Modeling of Fission-gas Behavior during Steady-state Conditions

During this quarter, the steady-state GRASS code verification effort has required the inclusion in GRASS of several additional models for fission-gas release. This new version of GRASS, GRASS-Mod 2, differs from its predecessor, GRASS-Mod 1, in that GRASS-Mod 2 includes:

(a) Enhanced diffusivities (for diffusivities less than those calculated from the theory of surface diffusion) of fission gas on grain boundaries that have the form

$$D_n = 1.12 \times 10^{-8} \exp[-32{,}000/(1.986T)](R_A/R_n)^{1.62} \text{ cm}^2/\text{s}, \quad (1)$$

where D_n is the diffusivity of a bubble with a radius R_n, T is the temperature (°K), and R_A is the atomic radius of the fission gas.

(b) The dependence of fission-gas behavior on fractional porosity, grain size, and pore size via a model of interconnected porosity.

(c) A grain-growth model for UO_2 in SST with the grain size as a function of time input to GRASS-Mod 2.

In GRASS-Mod 1 the grain-boundary-bubble diffusivities were taken as proportional to the diffusivities of fission-gas bubbles in the lattice. However, fission-gas-bubble diffusion in the matrix is slower than that predicted by the theoretical model based on surface diffusion,[1] probably because the motion of a bubble requires the nucleation of "steps." The values of the bubble diffusivities will depend on the step density. Since grain boundaries contain natural steps, the bubble diffusivities on the grain boundaries will probably be "enhanced" and exhibit different temperature dependencies when compared with lattice-bubble diffusivities. The values of the grain-boundary fission-gas-bubble diffusivities should lie between the values for the bubble diffusivities in the lattice (as a lower limit) and the values of the bubble diffusivities as calculated from the theory of surface diffusion.

Few data are available on the values of fission-gas-bubble diffusivities on grain boundaries. Thus, the diffusivities of fission-gas bubbles on the grain boundaries are the main physical properties determined through GRASS verification (e.g., Eq. 1). GRASS-Mod 1 could not be verified for "realistic" values of the grain-boundary-bubble diffusivities. Indeed, this fact, along with

the successful preliminary verification of GRASS-Mod 2 (to be described below), underlines the importance of the models listed in Items (a)-(c) above. These models are not independent, and it is the interplay between them that is critical to describing fission-gas release.

The role of interlinked porosity in fission-gas behavior has only recently been recognized.[2-4] In GRASS-Mod 1 the rate at which the fission gas reached the grain edges was assumed to be the controlling factor for fission-gas release. However, the escape path of fission gas from the grain edges to the free surface depends on physical properties such as fabricated porosity, pore size, and grain size. To account for actual gas release, this dependence of grain-edge escape paths for fission gas on the fuel microstructure must be included in the model.

A treatment of interlinked porosity, based on the mathematical theory of percolation and discussed in the July-September 1975 quarterly report (ANL-75-72, p. 30), has been incorporated into the GRASS code. In this model, fission gas that reaches the grain edges encounters a network of interconnected porosity that may or may not form a part of the free surface. The probability that a chain of pores does connect to the free surface, defined as the pore interlinkage fraction, depends on physical properties such as grain size, pore size, and fractional porosity. The rate of fission-gas release is then given by the amount of gas that arrives at the grain edges per unit time multiplied by the pore interlinkage fraction. The remaining gas links up along the grain edges and contributes not only to pore growth but to grain-edge swelling. In fact, at relatively high burnup (~3 at. %), the grain-edge swelling due to interconnected tunnels of fission gas is the dominant fuel-swelling mechanism.[3] During hypothetical off-normal conditions, the fission gas retained along the grain edges is probably the main contribution to fission-gas release. During power ramps, these tunnels of fission gas may vent as a result of increased internal pressure, or fuel cracking may connect the tunnel edges directly with the free surface.

The grain size is a critical parameter in the phenomena of fission-gas behavior. The size of the grain affects not only fission-gas release but also the size of the bubbles that reside on the grain boundaries. The bubble-size distributions in the fuel are an important factor in fission-gas behavior, not only during normal operation but during hypothetical off-normal situations as well. A new model for grain growth has been incorporated into SST that provides GRASS with the regional grain size as a function of time. This grain-growth model is based on the work of Singh[5] and gives the mean grain diameter D (μm) after annealing for a time t (h) at a temperature T (°K) by

$$D^3 - D_0^3 = 5.2 \times 10^{14} \exp\left(\frac{-120300}{1.986T}\right) t, \qquad (2)$$

where D_0 is the initial grain size. Implicit in the use of this equation is the assumption that it is applicable to steady-state UO_2 irradiation. As additional data become available, the "validity" of Eq. 2 will be more evident.

The task of verifying the GRASS code for a set of data is additionally complicated by the strong coupling between GRASS and the SST gap-conductance and fuel-swelling models. The initial SST-GRASS verification has been completed. The SST-GRASS code results for three CVTR fuel-rod irradiations are shown in Figs. II.1 and II.2. The fractional gas release versus reactor irradiation time is shown in Fig. II.1 with the experimental data (one point for each rod at end of life). Figure II.2 shows the GRASS-calculated total gas release as a function of irradiation time, with end-of-life data points based on calculated fission-gas generation rates. As is evident from these figures, the agreement between GRASS and the CVTR data is reasonable. A simple interpretation of Figs. II.1 and II.2 is complicated by the quite different variable irradiation histories of these three CVTR rods. For rods 33.833 and 44.732, the fraction of fission gas released has a tendency to rise rapidly and then flatten out toward the end of the irradiation time. This release-rate behavior is obscured for rod 13.831 because of its relatively complicated irradiation history. The rod was irradiated at a fairly constant (relatively low) power level for the first 2600 h of irradiation before the power level was increased and the last 1700 h at an incrementally increasing power level.

The decrease in the rate of gas release as a function of irradiation time observed in Figs. II.1 and II.2 can be understood in terms of grain growth. As the grains in the hotter fuel regions grow, the pore interlinkage fraction (Eq. 1) increases and a higher rate of gas release would be expected. However, the rate at which fission gas migrates from the grain boundaries to the grain edges is proportional (approximately) to the reciprocal of the grain diameter, and the net result is a decrease in the gas-release rate.

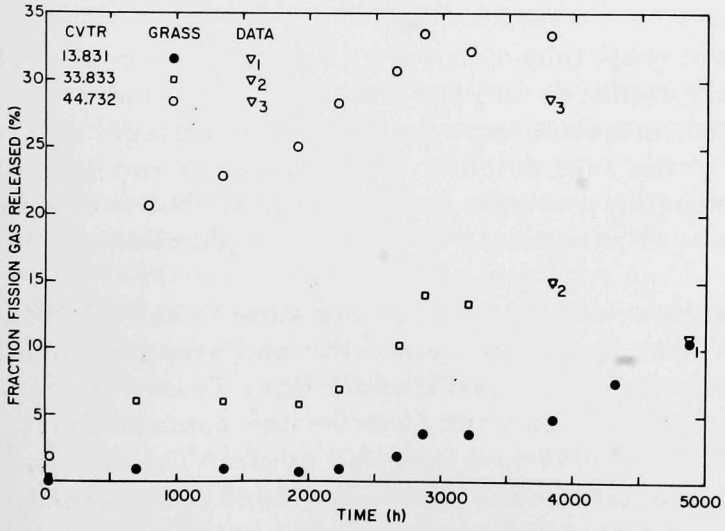

Fig. II.1. GRASS-calculated Fractional Fission-gas Release for Three CVTR Fuel Rods and End-of-life Comparison with Measured Data. Neg. No. MSD-62302.

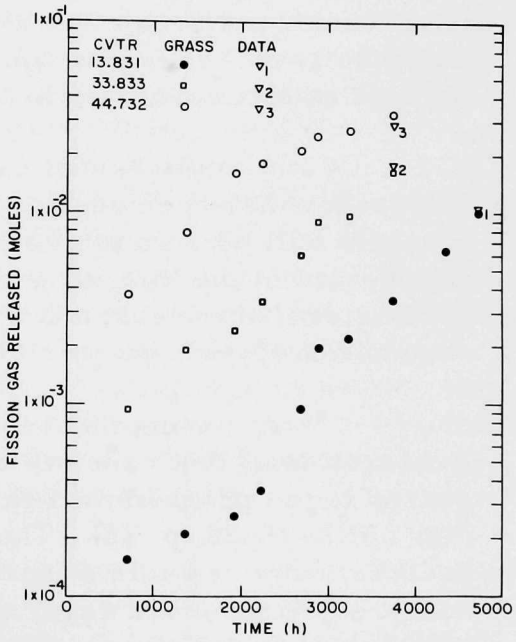

Fig. II.2. GRASS-calculated Total Fission-gas Release for Three CVTR Fuel Rods and End-of-life Comparison with Data. Neg. No. MSD-62303.

B. Experimental Technique (M. G. Seitz and L. R. Kelman, MSD)

1. Direct-electrical-heating Apparatus (M. G. Seitz and D. R. Pepalis, MSD, and E. W. Johanson, EL)

The DEH apparatus (ANL-75-28, p. 25) has been assembled in the hot cell and is being used for transient testing of irradiated LWR fuel. Changes to improve the accuracy of the experimental parameters recorded during testing and better regulate the electrical power applied to the fuel are being made to optimize conditions for use in the initial transient test described in Sec. II.C.1.

An rms analyzing device was added to the DEH apparatus to measure the effective values of the current and voltage. The full-scale values (2.5-V maximum output signal) of the current and voltage to be recorded can be selected with multiposition switches from values of 50, 100, 250, 500, 1000, and 1500 V and 10, 12.5, 25, 50, and 100 A. The effective current and voltage are multiplied together electronically to give the total power. Because the load is resistive, the total power is a measure of the heating power (i.e., active power) delivered to the fuel stack. The power signal, which is the product of the current and voltage, ranges from 500 to 150,000 W.

The analyzer was found to give true rms readings in the frequency range from dc to 20,000-Hz sinusoidal signal. The response of the analyzer was calibrated on all scales with standardized dc and 1000-Hz ac voltage signals. The time constants (time required to attain 63.2% of a step change) for the rms system were measured to be 0.18 s for the voltage, 0.20 s for the current, and 0.10 s for the power. Thus, the metering system has a sufficiently fast response time to record the transient conditions required for the test matrix described in Sec. II.C.1.

A multichannel cathode-ray-tube recorder (Honeywell Model 1858 Visicorder) has been received and replaces the one that was borrowed. Six channels will be used to record the effective current, effective voltage, active power, emf of the thermocouple at the fuel surface, and outputs of two optical pyrometers, one inside and one outside the cell. At present, all but one of the channels are used; the in-cell optical pyrometer is still to be purchased.

A driving mechanism [four-decade electronic time base (4ETB), Research Inc.] that consists of a variable-pulse generator and stepping motor geared to the programmed axis has been ordered for the Data Trak Programmer (ANL-75-28, p. 25). The mechanism is used to drive the control chart in increments of 1 min at speeds from 9999 to 1 min per cycle. This device will provide the more rapid and selectable time spans required for planned DEH tests; the present single 60-min cycle is inadequate.

2. Fuel Temperature during Direct Electrical Heating (M. G. Seitz, MSD)

The temperature of the fuel during transient heating, as well as the behavior of the fission gases, must be determined for the experimental program to be useful to model developers. The DEH Transient Temperature Distribution (DEHTTD) code (ANL-75-28, p. 27) is used to predict the temperature profile within the fuel from the surface temperature, any one of the electrical parameters (voltage, current, or power), and the electrical and thermal conductivities of the fuel. The experimental parameters must be measured accurately as a function of time, and the properties of the fuel must be sufficiently well known to permit accurate prediction of the temperature profiles.

The technique of continuously measuring the surface temperature of the fuel stack with a Chromel/Alumel thermocouple (ANL-75-72, p. 37) has worked well in the transient tests run to date. An additional thermocouple will be introduced to permit simultaneous measurement of temperature at a second location on the surface of the fuel or end pellets. Experience to date has revealed the need for an optical pyrometer to complement the thermocouple for measuring the relatively low DEH-specimen surface temperatures anticipated in most of the planned initial transient tests (Sec. II.C.1). An optical pyrometer designed for use in the 400-1100°C temperature range will be procured early next quarter. The head of this pyrometer will be installed inside the hot cell to avoid excessive attenuation of the infrared radiation through the window.

The electrical-conductivity measurements described in Sec. II.C.2 were used as input data for the DEHTTD code. A temperature profile was calculated from the surface temperature and measured power input. The current and voltage that would occur with the calculated temperature profile and specific power were also predicted with the code and were consistent with experimental measurements at surface temperatures below 1000°C.

However, at higher temperatures there is disagreement between the predicted and measured current and/or voltage; this suggests that the conductivity-temperature dependence presently used in the code may not accurately depict that of the fuel stack at high temperatures. To eliminate this disagreement, the conductivity measurements will be extended to higher temperatures. The dependence of the conductivity on temperature used in the DEHTTD code will be adjusted to give accurate predictions of measured parameters at high temperatures. The final solution will be verified by using the code to predict center melting that is observed experimentally.

Although the initial work appears to indicate that the fuel stack may be treated as a homogeneous material, it in fact consists of two materials: the unirradiated end pellets and the irradiated fuel. A more accurate treatment, which will develop two solutions, one for the end pellets and one for the fuel, is being considered to account for this difference. If this procedure is

used, the code will again be checked by comparing its predictions with experimental results. To be of most value, this treatment will include the surface temperature of the end pellets. The addition of another thermocouple and the in-cell optical pyrometer will permit measurement of this temperature.

3. Fission-gas Collection, Measurement, and Sampling System (M. G. Seitz and D. R. Pepalis, MSD)

Initial DEH tests using the fission-gas collection apparatus (ANL-75-28, Fig. II.1) yielded unexpectedly large quantities of air collected in the charcoal trap with the fission gas. We suspect that incomplete purging of the system was the source of the atmospheric gases. In future runs a more extensive purging of the system will be implemented. Evacuation of the specimen chamber and collection train before filling with helium also appears feasible. The latter method may be used to remove atmospheric gases if it is required.

The fission-gas measuring and sampling apparatus is being assembled and tested. Figure II.3 shows the apparatus during assembly. The 73-liter Dewar and krypton-xenon cold trap are seen at the left of the photograph and are situated in front of the helium-gas outlet and return discharge in the cell wall. Gases from the trap will be piped to the measuring and sampling apparatus, where they will be moved into a calibrated volume with the Toepler pump (A).

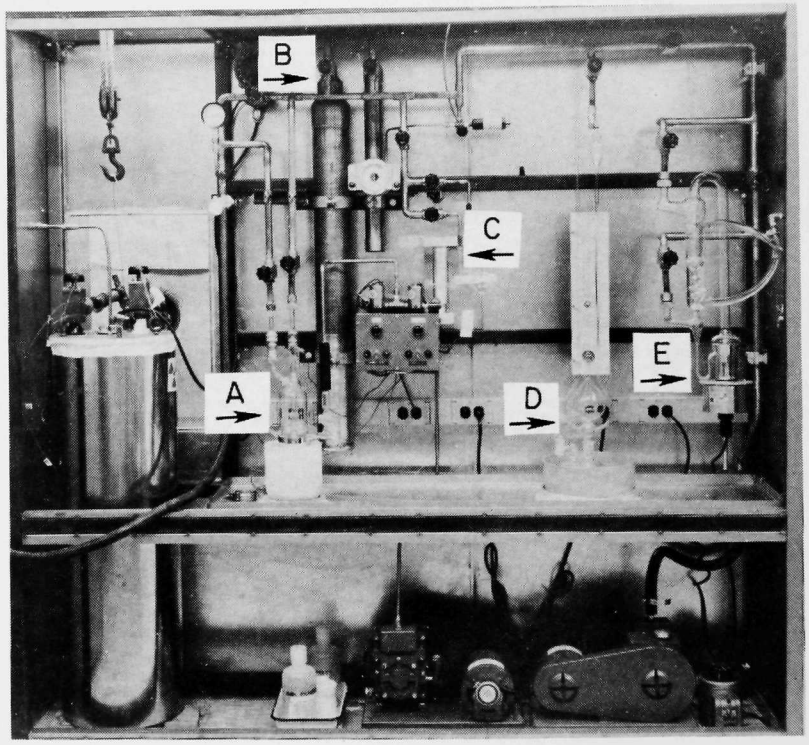

Fig. II.3. Fission-gas Measuring and Sampling Apparatus Used for Measuring Pressure and Volume of Gas and Taking Samples for Other Analysis. The major features of the system are identified in the text. Neg. No. MSD-186384.

Toward the back of the cabinet are two reservoirs (B) that will be calibrated and may be introduced as part of the calibrated volume. Samples of the gas are sealed off in glass bulbs that are fitted to the sampling ports (C). The pressure in the apparatus is monitored with a capsule-type gauge (Wallace and Tiernan 300 series), a thermocouple gauge, and a McLeod gauge (D). The diffusion pump (E) and the fore pump at the left of the cabinet are used to evacuate the system before admitting gas. After the apparatus is assembled, the cabinet will be fitted with sliding doors and an overhead duct for ventilation.

4. Hot Cell (M. G. Seitz and D. R. Pepalis, MSD)

The specimen-preparation box, which is a completely enclosed box within the K-1 cell in M-Wing of Building 200 (ANL-75-72, p. 34), has been equipped to prepare fuel specimens. Figure II.4 is a view through the cell window that shows the cutoff saw, the slip-impregnation gun and fittings, and the device used to transfer the fuel specimen from the Zircaloy cladding into a close-fitting quartz container. Although these items are essentially duplicates of those used previously, modifications were necessary to permit the preparation of several useful fuel specimens during this quarter.

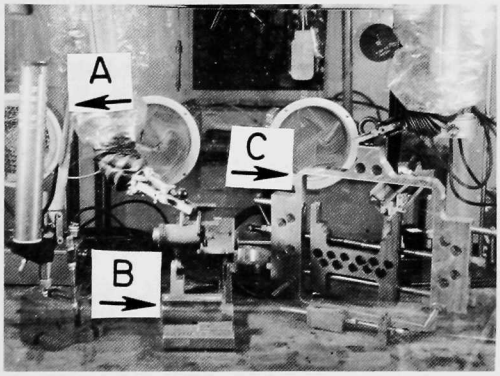

Fig. II.4

Specimen-preparation Box as Positioned at the A Window of the K-1 Hot Cell. The pieces of equipment used for extracting fuel from cladding are the (A) slip-impregnation gun, (B) cutoff saw, and (C) extraction frame. Clam-shell blocks used to hold the fuel, cladding, and quartz container during extrusion are seen below the extraction frame. Neg. No. MSD-186351.

The Saxton PWR fuel rod, MAPI No. M12, and the General Electric Company (GE) BWR rod, GE-SA-1 No. B58 (ANL-75-58, p. 41), as well as the upper half of the F-7 rod from the CPL Robinson plant (ANL-75-58, p. 55), have been transferred to storage in the fuel safe of the K-1 hot cell.

C. Experimental Program (M. G. Seitz and L. R. Kelman, MSD)

1. Experimental Plan (L. R. Kelman and M. G. Seitz, MSD)

The matrix for the initial set of DEH transient tests has been developed to provide experimental correlations and data on fission-gas behavior in and release from transient-heated fuel, which will be of use to model developers. A condition considered in formulation of the matrix was the use of existing capabilities of the experimental apparatus and techniques. The capabilities, some of which are described in the present report and in previous reports (ANL-75-28, -58, and -72), include recovery of useful DEH fuel

specimens in quartz containers and transient heating of the fuel so that the center heats at rates up to 500°C/s. The tests may be run to melting of the fuel with attendant failure of electrical continuity, or they may be terminated after a designated time.

The range of thermal transients and temperature profiles to be produced in the fuel during the transient tests encompasses that anticipated in PCM accidents. Heating rates of 20, 200, and 500°C/s have been selected for the center temperature. The center temperatures that result from these heating rates are shown schematically in Fig. II.5 as the solid straight lines, and the corresponding surface temperatures are shown in dashed lines.

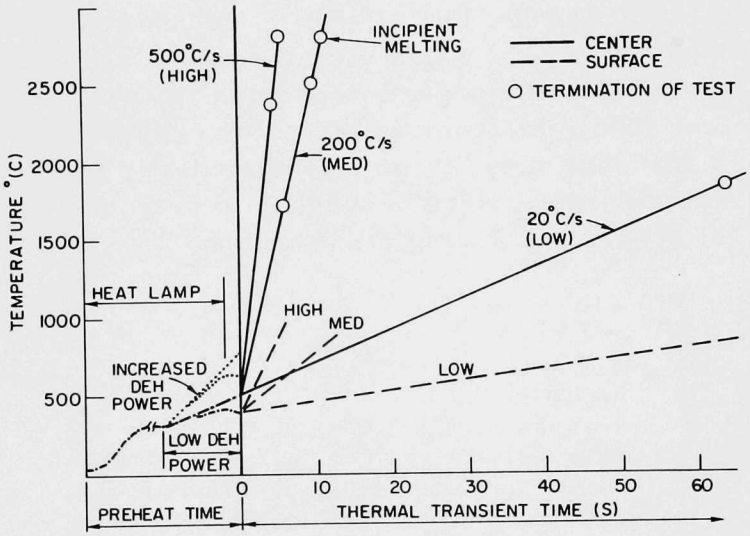

Fig. II.5

Schematic of Thermal Histories of Fuel in Initial DEH Transient Tests. The fuel is first heated with an auxiliary heat lamp, followed by the application of low DEH power to obtain starting conditions. High DEH power is then applied to the fuel stacks to cause transient heating. ANL Neg. No. 306-76-44.

A matrix of the minimum number of tests planned for the first phase of the program is shown in Table II.1. The table details 25 tests that represent a broad spectrum of temperature ramps, power, and burnup applicable to possible PCM accidents. This number of tests, which include fuel from three reactors, is considered a minimum to cover the desired conditions.

Before the matrix tests are begun, a series of DEH tests will be run to optimize conditions for the matrix and establish the reproducibility of temperature profiles and behavior of several fuel specimens from the CPL Robinson fuel rods. Modifications to the test plan and additional tests can be expected if the need is indicated by the results of the preliminary tests. The tests that will be run to produce center melting for each temperature ramp will be used to verify computed temperature profiles for transient heating and establish the maximum time for the transient.

A series of interrupted tests, which will be run to determine fuel and fission-product behavior during a heating ramp, is shown in Table II.1 for a center temperature ramp of 200°C/s. The points at which the tests are interrupted were chosen arbitrarily; it may be desirable to change them after preliminary results are obtained.

TABLE II.1. Minimum Number of Tests in Initial DEH Transient Test Plan

Fuel Source	W Robinson PWR (Rod Center)			W Robinson PWR (Rod Ends)	GE SA-1 BWR	MAPI PWR
Maximum Burnup, MWd/Mg	36,000			Decreasing burnup	36,200	8000
Linear Heat Rate, kW/m	23 (avg)			Decreasing power	46 (max)	13-16
T_{ℓ} Ramp Rates, °C/s	20	200	500	200	200	200
Low Initial T_{ℓ}						
Condition at Start of Ramp	-	1	-	-	-	-
60% Time to Center Melting	-	1	-	-	-	-
80% Time to Center Melting	1	2	1	4	2	2
Incipient Center Melting	1	2	1	1	1	1
Fuel Failure	-	1	-	-	-	-
Higher Initial T_{ℓ}						
80% Time to Center Melting	-	2	-	-	--	-
Incipient Center Melting	-	1	-	-	-	-
Total (25 Tests Minimum)	2	10	2	5	3	3

Most of the tests will be started with fuel temperatures that are lower than in-reactor. The low starting temperature was selected to minimize thermal effects on fission-gas movement before the transient. In addition, a limited number of tests with increased initial temperatures will be run.

Tests are also planned to determine fission-product behavior as a function of position in the fuel rod over a range of burnup. For the fuel in these tests, the burnup and power levels vary simultaneously so that the effect of each on fission-product behavior cannot be determined. A limited number of tests using high-burnup, high-power GE (BWR) and low-burnup, low-power MAPI (PWR) fuel are planned as a step in the direction of determining the effects of burnup and power.

Successful completion of this series of DEH tests will add significantly to the existing data base[6] for the fraction of fission gas released at various stages of a transient to melting. The fuel-temperature profiles and heating rates in DEH tests are more prototypic of reactor thermal conditions than those obtained in the externally heated tests of Ref. 6.

2. Experimental Results (M. G. Seitz and D. R. Pepalis, MSD)

Three irradiated Robinson fuel specimens were prepared using slotted quartz tubing as containers for the fuel, as described in the previous quarterly report (ANL-75-72, Fig. II.10), and a fourth specimen was prepared in a quartz container without slots. The specimens were mounted in the specimen chamber for transient testing and heated with the auxiliary line heater (ANL-75-72, p. 35) after purging the specimen chamber with helium. The conditions and results of the four tests are shown in Table II.2.

TABLE II.2. DEH Tests Preceding the Transient Test Matrix

Test	Quartz Container	T_i,[a] °C	T_f,[b] °C	Time, s	Comments
1	Slotted	600	1000	9	Condensed fission products analyzed
2	Slotted	-	-	-	Fuel column failed
3	Slotted	-	-	-	Fuel column failed
4	Drilled	906	1217	20	Gas analysis, center melting

[a] T_i = initial surface temperature.

[b] T_f = final surface temperature.

The thermal transient was initiated after a conditioning period in which a steady-state temperature profile was established by applying low DEH power. It was anticipated that the thermal transients would produce center melting. The first transient test was started with a steady-state surface temperature of 600°C. A maximum surface temperature of 1000°C was achieved in 9 s, at which time the test was terminated. The specimen chamber and fuel column during transient heating are shown in Fig. II.6.

The fourth transient test was started with a steady-state surface temperature of 906°C, and a maximum surface temperature of 1217°C was achieved in 20 s (the termination of the test). Electrical continuity was maintained throughout the first and fourth tests.

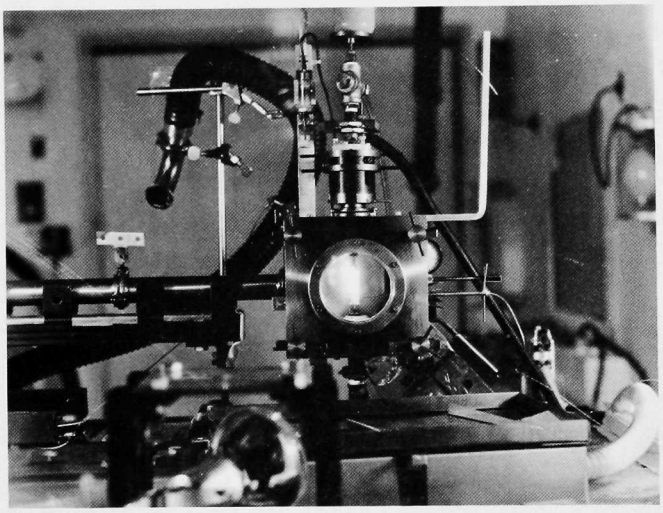

Fig. II.6. First High-burnup Robinson Fuel Specimen in Slotted Quartz Container during DEH Transient Test. Neg. No. MSD-185851.

However, the second and third specimens fractured when the electrical power was turned on. These failures are believed to be due to the cracking of the quartz containers along the slots as a result of stresses that may have been initiated, for example, by thermal expansion of the fuel, fuel disaggregation caused by the release of volatiles as electrical heating started, or nonaxial loading by the electrodes. Several changes were made to eliminate this failure mode, including the use of a larger-inside-diameter quartz container with no slots, a lighter weight on the upper electrode, and an extended preheat period to improve the bake-out of the volatiles. With the weight presently used (400 g), the load on the fuel corresponds to that experienced under a 0.50-m-long fuel column.

To promote the release of volatile bonding material, the preheating of the fuel has been extended to include heating the specimen to 65°C for 24 h before the temperature is raised to 300°C and held for 60 min. The fuel in the fourth test was preheated in this manner, and the test was run successfully to the completion of the electrical transient.

It is necessary, for several reasons, to monitor the fuel-stack electrical conductivity as a function of temperature before and during the heatup of the stack. The room-temperature conductivity measurement is used to ensure that the fuel column is properly loaded in the specimen chamber and correctly positioned with respect to the electrodes. The conductivity at higher temperatures gives an indication of the voltage that is required to initiate electrical heating. Furthermore, the conductivity of fuel columns is compared to see how uniform they are and, consequently, how reproducible the DEH tests may be. Finally, the measured conductivity-temperature relationships are used as direct input to the DEHTTD code.

For measurements taken with a heating rate below 1°C/min, the conductivity only changed with temperature and did not depend upon how long the sample had been heated. In addition, the dependence of the conductivity on temperature generally remained the same for a given fuel specimen whether the fuel temperature was increasing or decreasing. These observations indicate, among other things, that the fuel columns were uniformly heated to the temperature indicated by the thermocouple at the surface of the fuel. This behavior is consistent with previous observations in which little difference was found between the surface and center temperature of UO_2 pellets that were heated with the line heater.

The observed dependence of the product of the stack conductance and temperature on the reciprocal of the temperature for the four fuel stacks is shown in Fig. II.7. Over the temperature range investigated (25-325°C), the conductivity of a specific fuel stack closely follows the relationship

$$\sigma = (K/T)\exp(-0.3/kT), \qquad (3)$$

where K is a constant, T is the absolute stack temperature, and k is Boltzmann's constant. From the figure, K can be seen to vary for different fuel stacks. The behavior observed here is similar to that reported for sintered nonstoichiometric UO_2,[7] and single crystals of UO_2,[8] in which K is dependent upon the stoichiometry of the material.

Figure II.8 shows the fuel column from the fourth transient test. The fuel column and quartz container are seen to have remained intact during the test. The fuel was almost completely obscured by a silvery deposit that accumulated on the inner surface of the quartz during transient heating. The deposit terminates sharply at the fuel and end-pellet interfaces and probably consists of condensed fission products from the fuel. Analysis of the deposit to identify the radioactive isotopes is underway.

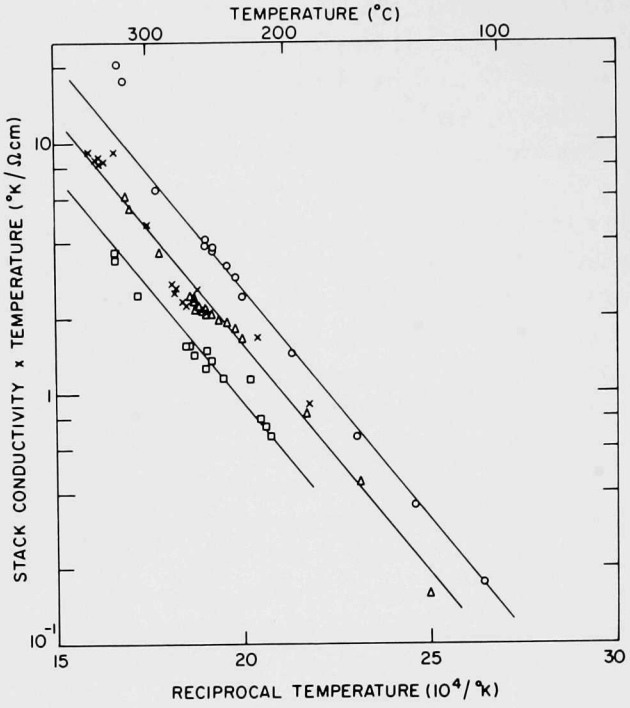

Fig. II.7

Electrical Conductivity as a Function of Reciprocal Temperature for Irradiated PWR Fuel Stacks Prepared for DEH Transient Heating. The different symbols refer to data from four fuel stacks. ANL Neg. No. 306-76-43.

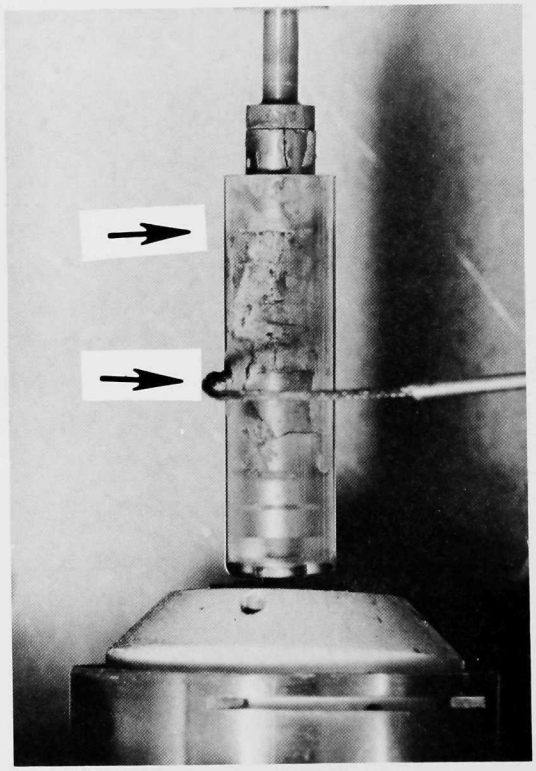

Fig. II.8

Fourth PWR Fuel Column after Transient Test. Arrows delineate the extent of the irradiated fuel with unirradiated UO_2 pellets above and below it. The thermocouple can be seen extending around the front of the column and through the quartz to the surface of the fuel. Neg. No. MSD-186091.

After DEH testing, the fuel columns were removed from the specimen chamber and returned to the containment box for examination. The slotted quartz container used in the first test fractured from handling, and the fuel aggregate fell from the quartz. The tungsten disk, end pellets, and fuel were free of the quartz and did not appear to have chemically reacted with it. Figure II.9 shows the fuel aggregate from the first run. The long piece in the

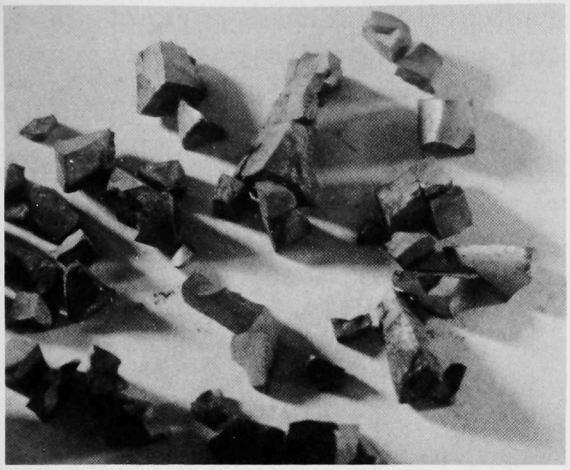

Fig. II.9. Aggregate of PWR Fuel from CPL Robinson Plant after Transient Test. Neg. No. MSD-185884.

center of the photograph is the length of the fuel column used and appears to be several pieces connected by a melt column. No other features peculiar to the transient-tested fuel were observed (e.g., new chemical phases, additional fracturing, evidence of chemical reactions, and other effects observable in handling or under low magnification).

The quartz container used in the fourth transient test remained intact, and the components of the column were pushed out of the cylinder without resistance. The end pellets and fuel were handled with forceps. Evidence of melting was noted on the ends of the pellets. The melt zone appeared to extend through nearly the entire length of the column as evidenced by the hole or altered spot on the ends of all pellets except the end at the lower electrode. When the fuel was removed from the container, it fell into pieces similar to those in Fig. II.9.

From the appearance of the fuel columns after transient testing, the fission gases released from the fuel did not appear to be prevented from moving to the helium gas stream and ultimately being captured in the krypton-xenon cold trap. That is, the quartz container, together with the fuel column, did not form enclosures that were inaccessible to the helium sweep gas. Thus, it is believed that, following the purge of the specimen chamber and collection system after transient testing, all the fission gases were moved to the krypton-xenon cold trap.

After passing through the krypton-xenon trap, the helium sweep gas in the fourth test was monitored for radioactivity. No release of activity past the trap was discernible above background, indicating that the trap was working with high efficiency.

Gases collected from the fourth test were analyzed to identify the major constituents. As discussed in Sec. II.B.3 of the present report, large quantities of atmospheric gases were found. Even so, xenon could be identified in the sample. Furthermore, the isotopes of xenon--131, 132, 134, and 136--were identified in the sample in the proportions 0.4:0.4:1.0:0.7. Xenon-129 was not detected, clearly indicating that the xenon is fission gas with little or no atmospheric xenon containment. From a gamma-energy spectrum, the only radionuclide present in the trapped gas was found to be ^{85}Kr, as evidenced by a gamma peak at 515 keV.

The fission products from the first test that accumulated on the tantalum plates in the specimen chamber and on the Raschig-ring traps were

sampled for analysis. Gamma-energy spectra of the five swipe samples were taken to provide identification of the radioactive nuclides present. The proportion of ^{134}Cs to ^{137}Cs found in all samples was the same and accounted for most of the activity of the samples.

A long count (3800 min) was taken of the sample obtained 0.19 m from the start of the Raschig-ring trap and provided identification of the fission-product ^{110M}Ag. The relative amounts of ^{137}Cs, ^{134}Cs, and ^{110M}Ag calculated to be present in the condensate were 285, 161, and 1, respectively.

3. Burnup Analysis (S. M. Gehl and M. G. Seitz, MSD)

Results of ^{148}Nd mass-spectrometric burnup analysis of samples taken from three axial positions in Rod F-7 are presented in Table II.3. The experimental determinations were performed at the Analytical Laboratories of ANL-West. The isotopic analyses were intended to serve as reference points for the calibration of the gross and isotopic gamma-activity traces described in the July-September 1975 quarterly report (ANL-75-72, p. 42). However, for the points analyzed, the ratio of ^{148}Nd burnup to gamma-scan intensity is not a constant; a large deviation in this ratio is observed for the bottom fuel pellet in the rod. This discrepancy may be explained by distortions in the neutron energy spectrum or different burnup histories of the center and periphery of the core, such that ^{148}Nd is enriched at the periphery relative to the amount of radionuclides present, as estimated by the total gamma activity. At the bottom of the core, from gamma scans for individual isotopes, ^{148}Nd was found to be enriched relative to ^{137}Cs but depleted relative to ^{106}Rh. Consideration will be given to these variations to select a measure of gamma activity that is closely related to burnup.

TABLE II.3. Burnup Analysis of CPL-Robinson Fuel Rod F-7

Sample Identity	Distance from Rod Bottom, m	U,g	^{148}Ni, μg	Burnup, at. %	Relative Gamma Scan Intensity (GSI)	Ratio BU:GSI[a]
155AA8	0.006	2.9072	389.8	1.26	21	0.060
155AA7	0.57	2.0758	706.2	3.14	75	0.042
155AA3	0.93	1.9152	648.5	3.12	78	0.040

[a]BU = burnup of sample (%).

4. Microstructural Characterization (S. M. Gehl, MSD)

The continuing investigation of the microstructural characteristics of the Robinson fuel has revealed a pellet structure that is radically different from the microstructure discribed in the July-September 1975 quarterly report (ANL-75-72, Fig. II.8). This pellet, shown in Fig. II.10, has a system of coarse porosity similar to the previously reported structure. However, the structure

also contains a system of patches in which the pore-volume fraction is locally higher than in the surrounding material. The mean pore intercept in the patches is ~10 μm. The patches are roughly the same size as the coarse pores. This pore structure is probably the result of faulty powder preparation or compaction during the fabrication of the pellet and was not formed during the fuel burnup cycle. Only one pellet of this type has been observed in the seven that have been prepared metallographically. The frequency of occurrence of this pellet type and the effect of its microstructure on fission-gas release are not known at present. If this pellet type constitutes an appreciable fraction of the Robinson fuel and the results of the DEH tests indicate different gas-release behavior, a study of the fission-gas release from such pellets may be warranted.

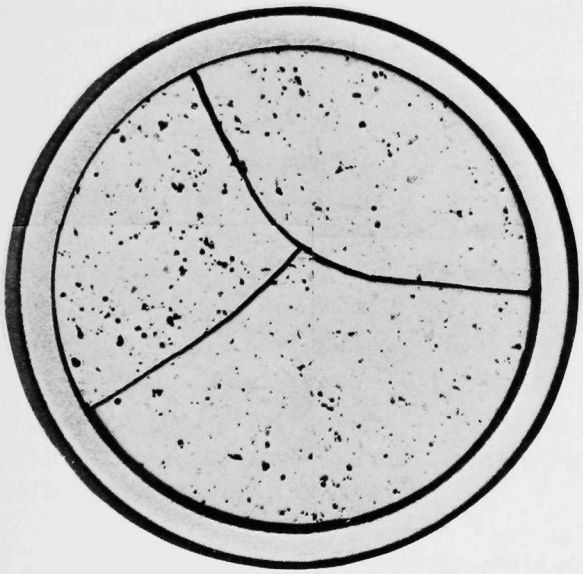

Fig. II.10

Microstructure of High-burnup Pellet 0.89 m from Bottom of Robinson Fuel Rod F-7. Mag. 7.5X. Neg. No. MSD-185985.

References

1. L. E. Willertz and P. G. Shewmon, Diffusion of Helium Gas Bubbles in Gold and Copper Foils, Met. Trans. 1, 2217 (1970).
2. L. C. Michels and R. B. Poeppel, Influence of Grain Boundaries on Fission Gas Release in Mixed-Oxide Fuels, Trans. Am. Nucl. Soc. 15(1), 199 (1972).
3. J. A. Turnbull and M. O. Tucker, Swelling in UO_2 under Conditions of Gas Release, Phil. Mag. 30, 47 (1972).
4. W. B. Beere and G. L. Reynolds, The Morphology and Growth Rate of Interlinked Porosity in Irradiated UO_2, J. Nucl. Mater. 47, 51 (1973).
5. R. N. Singh, Isothermal Grain Growth Kinetics in Sintered UO_2 Pellets, to be submitted to J. Nucl. Mater.
6. E. T. Weber, O. D. Slagle, and C. A. Hinman, "Laboratory Studies of Melting and Gas Release Behavior of Irradiated Fuel," Proc. of the Fast Reactor Safety Meeting, CONF-740401-P2, Am. Nucl. Soc., p. 641 (1974).

7. S. Aronson, J. E. Rulli, and B. E. Schaner, Electrical Properties of Nonstoichiometric Uranium Dioxide, Chem. Phys. 35(4), 1382 (1961).

8. P. Nagels, J. Devreese, and M. Benayer, Electronic Conduction in Single Crystals of Uranium Dioxide, J. Appl. Phys. 35, 1175 (1964).

III. MECHANICAL PROPERTIES OF ZIRCALOY CONTAINING OXYGEN

H. M. Chung, A. M. Garde, E. I. H. Lin, and T. F. Kassner, MSD

SUMMARY

Uniaxial and biaxial mechanical-property data are being obtained on oxygen-contaminated Zircaloy to establish a more quantitative cladding-embrittlement criterion applicable to postulated loss-of-coolant-accident (LOCA) situations in light-water reactors (LWR's). The mechanical-property information, when incorporated into fuel-element modeling codes, will provide a quantitative basis for evaluating cladding deformation over a wide range of LOCA and power-coolant-mismatch (PCM) conditions.

In the present reporting period, additional data have been obtained on the effects of texture, heat treatment, and oxygen concentration and distribution on the uniaxial tensile properties of Zircaloy-4. In general, the results indicate that (1) texture has a significant effect on the deformation behavior of Zircaloy at temperatures below ~850°C, (2) heat treatment that results in formation of the martensitic α' structure increases the ultimate tensile strength (UTS) and decreases the ductility of Zircaloy, and (3) oxygen concentrations in the range of 0.1-1.1 wt % (uniform distribution) result in a monotonic increase in the UTS at temperatures between 850 and 1100°C. The presence of brittle ZrO_2 and α-surface layers on composite specimens decreases the total strain, but does not change the UTS of the material significantly.

A systematic study of the diametral expansion and rupture characteristics of as-received Zircaloy-4 tubing has been conducted by means of high heating-rate burst tests. From information on the temperature, pressure, and diametral strain and strain rate, the onset of plastic instability was established and a relationship between the effective stress and strain during deformation was determined for each test. The circumferential strain and effective stress at the onset of instability were plotted as a function of burst temperature, and the results were compared with similar data from other investigations. The effects of heating rate and axial restraint of the cladding on the temperature and magnitude of the superplastic strain maxima, which occur at ~850 and ~1050°C, were evaluated from the available data. The microstructures of the Zircaloy cladding in the region of uniform deformation and the rupture areas have been examined for evidence of dynamic recrystallization, which leads to large superplastic deformations.

In conjunction with the experimental program, a modeling effort has been initiated to (a) provide an analytical tool for interpretation of the mechanical-property data, (b) investigate Zircaloy cladding deformation under various postulated LOCA and PCM conditions, and (c) recommend modifications, if necessary, to the present acceptance criteria for emergency core cooling systems (ECCS's) in LWR's, based on the mechanical behavior of

oxygen-contaminated Zircaloy. To minimize the initial developmental effort, a literature and software-market survey of available nonlinear finite-element deformation codes was made and resulted in the selection of NONSAP. An IBM version of the code has been obtained, and modifications are in progress to incorporate the effect of a multiphase structure, containing oxygen concentration gradients, on the mechanical properties and deformation characteristics of composite Zircaloy material.

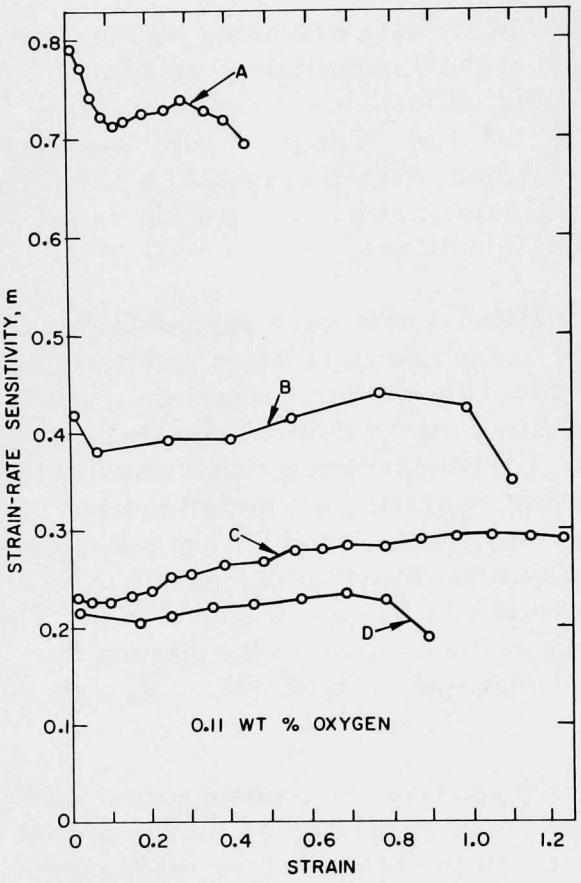

Fig. III.1

Strain-rate Sensitivity of As-received Zircaloy-4 at 850°C as a Function of Strain. The four curves are for different strain-rate ranges; (A) 3.3×10^{-6} to 3.3×10^{-5} s^{-1}, (B) 3.3×10^{-5} to 3.3×10^{-4} s^{-1}, (C) 3.3×10^{-4} to 3.3×10^{-3} s^{-1}, (D) 3.3×10^{-3} to 3.3×10^{-2} s^{-1}. ANL Neg. No. 306-76-10.

A. Mechanical Properties of As-received Zircaloy-4

1. Strain-rate Sensitivity of Zircaloy-4 at 850°C

Figure III.1 shows the effect of strain on the strain-rate sensitivity of as-received Zircaloy-4 at 850°C. The four curves are for different ranges of strain-rate change. As the starting strain rate decreases from 3.3×10^{-3} to 3.3×10^{-6} s^{-1}, the average value of the strain-rate sensitivity increases from ~0.2 to ~0.75. This observation is consistent with the earlier finding[1] that the superplastic elongation peak at 850°C is strongly dependent on strain rate. It was reported[1] that the total elongation at 850°C increases with a decrease in strain rate. These results show that the amount of the tensile elongation under superplastic deformation conditions is related to the magnitude of the strain-rate sensitivity.

2. Effect of Texture on Mechanical Properties of Zircaloy-4

Figure III.2 shows the influence of texture on the temperature dependence of uniform strain of Zircaloy-4. The orientation angles between the tensile axis and the rolling direction were 0° for longitudinal, 45° for diagonal, and 90° for the transverse specimens. Since the Zircaloy sheet had a texture in which most of the grains had basal poles tilted at ~30° away from the normal (thickness) direction toward the transverse direction, the longitudinal specimens had more grains favorably oriented for prism slip than the transverse specimens. The diagonal orientation is midway between the longitudinal and transverse orientations. The results in Fig. III.2 indicate that the uniform strain is somewhat texture-dependent below 800°C, whereas above this temperature the texture influence appears to be negligible.

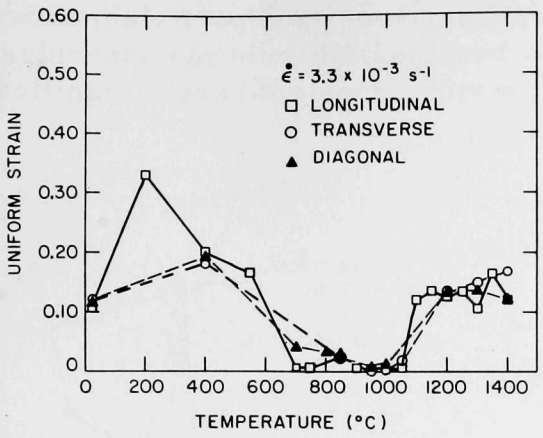

Fig. III.2

The Effect of Texture on the Uniform Strain of Zircaloy-4 at Temperatures between Ambient and 1400°C. ANL Neg. No. 306-76-12.

The texture dependence of the total strain of Zircaloy-4 is shown in Fig. III.3. The total strain is defined as $(\ell - \ell_0)/\ell_0$, where ℓ_0 is the initial gauge length of the specimen and ℓ is the specimen gauge length at fracture. The texture effect on the total strain is significant at the low-temperature superplastic elongation peak at 850°C, which implies that prism slip has an important role in superplastic deformation. Above 1000°C, grain growth during tensile testing is considerable; this makes it difficult to deduce the effect of texture on total elongation from the data in Fig. III.3.

Fig. III.3

Influence of Texture on the Total Strain of Zircaloy-4 at Temperatures between Ambient and 1400°C. ANL Neg. No. 306-76-20.

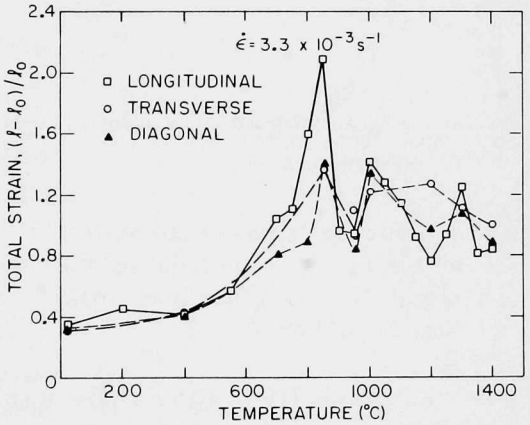

Figure III.4 shows the variation of the UTS with temperature. Although some texture effect is evident below 800°C, the UTS is independent of texture at higher temperatures. The strain-rate sensitivity is plotted against temperature at $\epsilon = 0.02$ for longitudinal and transverse specimens in Fig. III.5. For both specimen orientations, the strain-rate sensitivity has a maximum value at 900°C rather than 850°C, the temperature at which maximum elongation is observed. This observation implies that two conditions are essential for maximum superplastic deformation: a high value for strain-rate sensitivity m and the presence of a favorable microstructure. At 850°C, both these conditions are satisfied in that m is ~0.3 and the microstructure consists of two soft phases. The deformation within each α grain can be accommodated by the soft β phase at the grain boundary without void nucleation. At 900°C, although the strain-rate sensitivity is high, the microstructure

contains hard α-phase particles. In the presence of hard particles, accommodation of individual grain deformation becomes difficult and superplasticity is reduced. Figure III.5 also shows that texture does not have a significant influence on the strain-rate sensitivity.

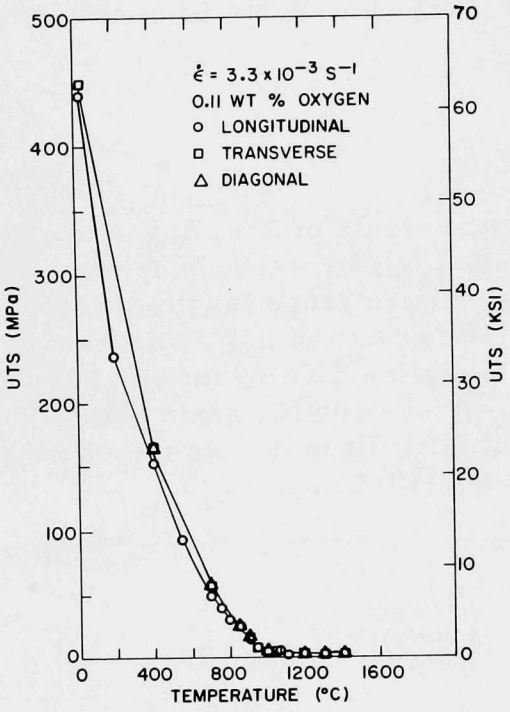

Fig. III.4. Temperature Dependence of the UTS for Longitudinal, Transverse, and Diagonal Zircaloy-4 Specimens. ANL Neg. No. 306-76-13.

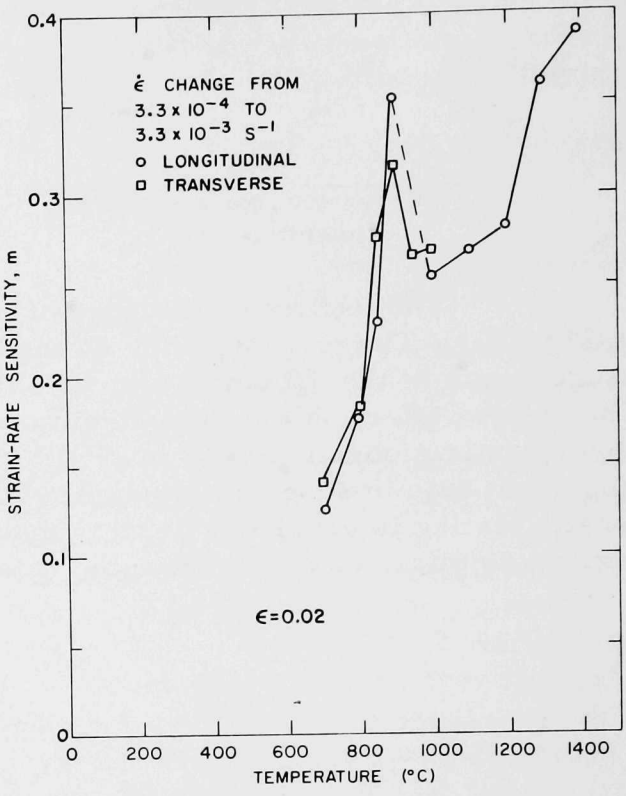

Fig. III.5. Strain-rate Sensitivity as a Function of Temperature for Longitudinal and Transverse Zircaloy-4 Specimens. ANL Neg. No. 306-76-14.

Figure III.6 shows the variation of strain-rate sensitivity with strain for longitudinal and transverse Zircaloy-4 specimens. Although the strain-rate sensitivity of a transverse specimen is always greater than that of a longitudinal specimen, the strain dependence of strain-rate sensitivity is almost identical in both cases.

The results presented in Figs. III.2-III.6 indicate that texture effects in the deformation of Zircaloy are significant below 850°C and negligible above 1000°C. Factors that contribute to this type of behavior are (a) the greater symmetry of the body-centered-cubic (bcc) structure of β-phase Zircaloy (>1000°C) when compared with the low-temperature (<810°C) α-phase hexagonal-close-packed (hcp) material, (b) the change in the dominant deformation mode of Zircaloy as the temperature is increased[2] (i.e., below 500°C, slip occurs on first-order prism planes; at higher temperatures, both basal and pyramidal slip take place), and (c) superplastic deformation at 850 and 1000°C, where possible grain rotation diminishes texture effects.

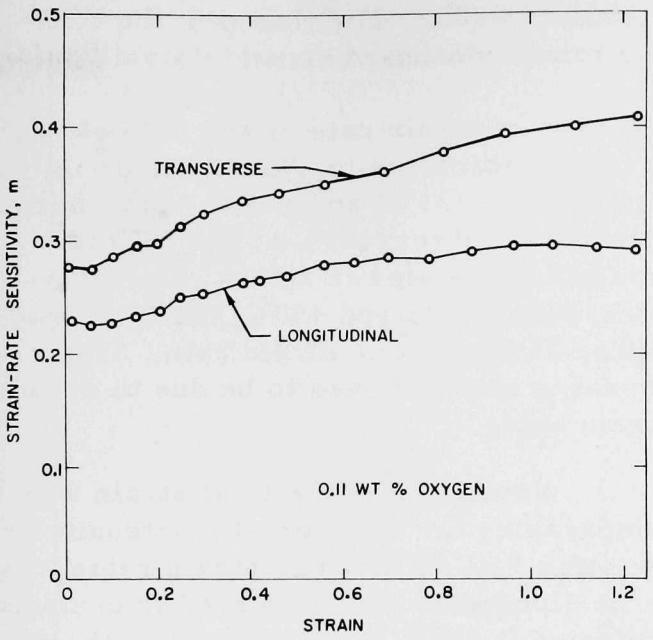

Fig. III.6

Strain Dependence of the Strain-rate Sensitivity of Transverse and Longitudinal Zircaloy-4 Specimens at 850°C. ANL Neg. No. 306-76-19.

3. Mechanical Properties of Zircaloy Martensite

A comparison of the total-strain-versus-temperature data for Zircaloy-4 specimens that contained equiaxed α phase and acicular α' phase was presented in the previous progress report.[1] It was observed that the specimen batch containing equiaxed α phase exhibited a large superplastic elongation peak near 850°C. Such a peak was considerably suppressed in another batch of material with an acicular martensite structure. Figure III.7 compares the corresponding UTS-versus-temperature data. The UTS data for the equiaxed specimens were obtained by heating the as-received equiaxed Zircaloy-4 to the deformation temperature and then straining to fracture. The data for acicular Zircaloy-4 were obtained by heating the as-received material into the β-phase field (1000°C) and then cooling the specimen to the deformation temperature (<1000°C) to conduct the tensile test to fracture. When β phase is cooled below the $\beta/(\alpha + \beta)$ phase boundary, it transforms martensitically to acicular α'. Below 850°C, the acicular α' material is stronger than the equiaxed α-Zircaloy; this is consistent with the elongation data reported earlier.[1] Moreover, whereas the UTS of equiaxed α decreases continuously as the temperature increases, that

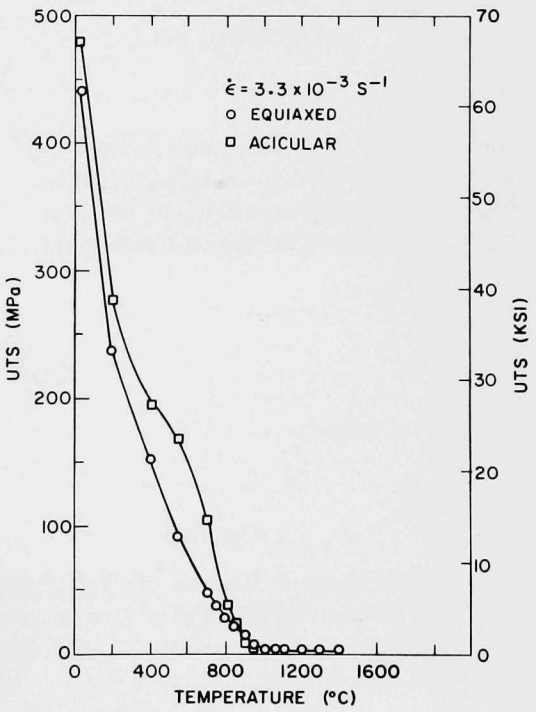

Fig. III.7

Comparison of the Temperature Dependence of the UTS of Zircaloy-4 Containing Equiaxed α Phase and Acicular (Martensitic) α' Phase. ANL Neg. No. 306-76-21.

of acicular α' shows a hump between 400 and 800°C. This hump in the UTS-versus-temperature diagram may be a manifestation of dynamic strain aging.[3]

Figure III.8 shows the influence of strain rate on the UTS of Zircaloy containing martensitic α' at temperatures up to ~950°C. At room temperature (23°C) and above 450°C, normal behavior is observed; i.e., the UTS is smaller at the slower strain rate. However, between 23 and 450°C, the UTS is higher at the slower strain rate. This reversal is also believed to be due to dynamic strain aging.

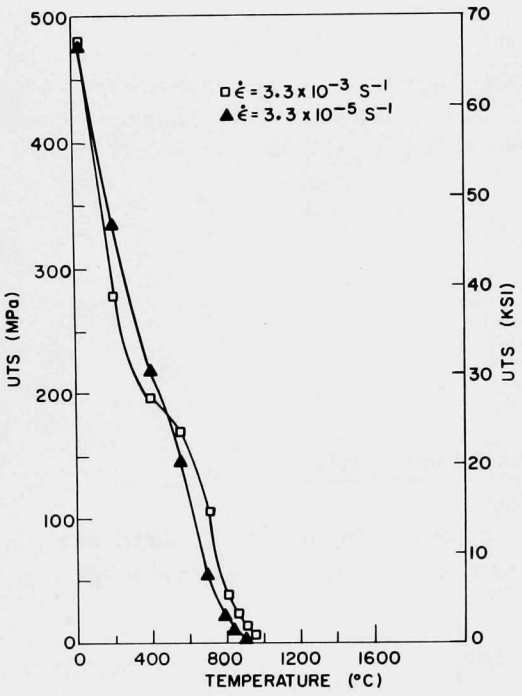

Fig. III.8

Comparison of the Temperature Dependence of the UTS for Zircaloy-4 Specimens Containing Acicular (Martensitic) α' Phase at Two Strain Rates. ANL Neg. No. 306-76-11.

Variations of the total strain with temperature for Zircaloy-4 martensite are shown in Fig. III.9 at two strain rates. The large elongation peak observed in equiaxed material at 850°C is not present in the data from the martensitic specimens at $\dot{\epsilon}$ = 3.3 x 10^{-3} s^{-1}. A microstructural examination of the martensitic specimen deformed at 850°C, $\dot{\epsilon}$ = 3.3 x 10^{-3} s^{-1}, shows no evidence of recrystallization during deformation. When the strain rate is decreased to 3.3 x 10^{-5} s^{-1}, however, the elongation increased to ~1.05. The microstructure in the deformed region, in this case, revealed extensive recrystallization. These results imply that, at sufficiently low strain rates (<10^{-5} s^{-1}), superplastic deformation reappears in Zircaloy martensite.

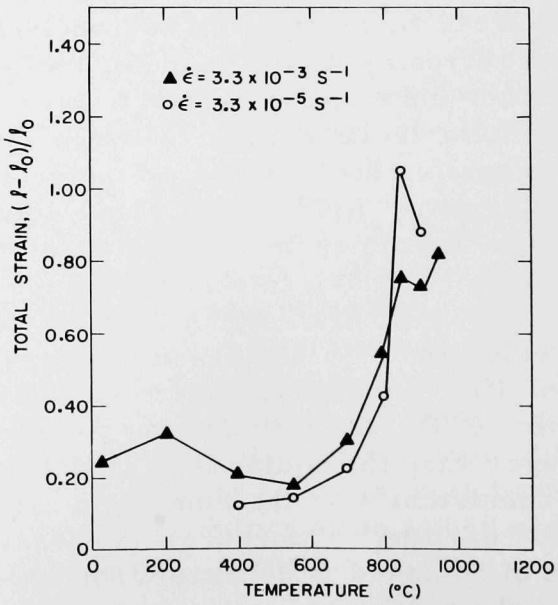

Fig. III.9

Effect of Strain Rate on the Total Strain of Zircaloy Martensite at Temperatures between Ambient and 1000°C. ANL Neg. No. 306-76-24.

Figure III.10 shows the temperature dependence of the strain-rate sensitivity of Zircaloy with equiaxed α and acicular α' structures. Consistent with the total elongation data in the temperature range of 850-1000°C, the strain-rate sensitivity of Zircaloy martensite is smaller than that of Zircaloy containing equiaxed α phase.

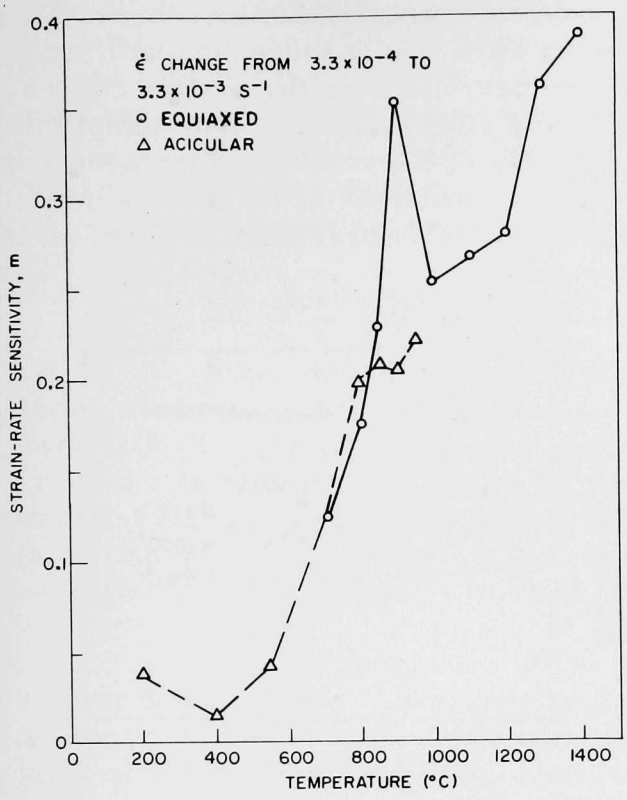

Fig. III.10

Temperature Variation of the Strain-rate Sensitivity of Zircaloy-4 with Equiaxed α and Acicular α' Grains. ANL Neg. No. 306-76-25.

B. Effect of Oxygen on the Mechanical Properties of Zircaloy-4

1. Homogeneous Oxygen Distribution

Uniform oxygen distribution was achieved before deformation by homogenizing the oxygen-charged samples at an appropriate temperature for sufficient time. The effect of oxygen in Zircaloy-4 on the UTS at temperatures in the $\alpha + \beta$ and β-phase regions is shown in Fig. III.11. Oxygen increases the UTS of Zircaloy monotonically at these temperatures. Similar data, presented earlier[1] for β-Zircaloy at higher temperatures (>1200°C), showed a less systematic trend because of complications, from grain growth in the material, that occurred during homogenization and deformation of the Zircaloy-oxygen alloys.

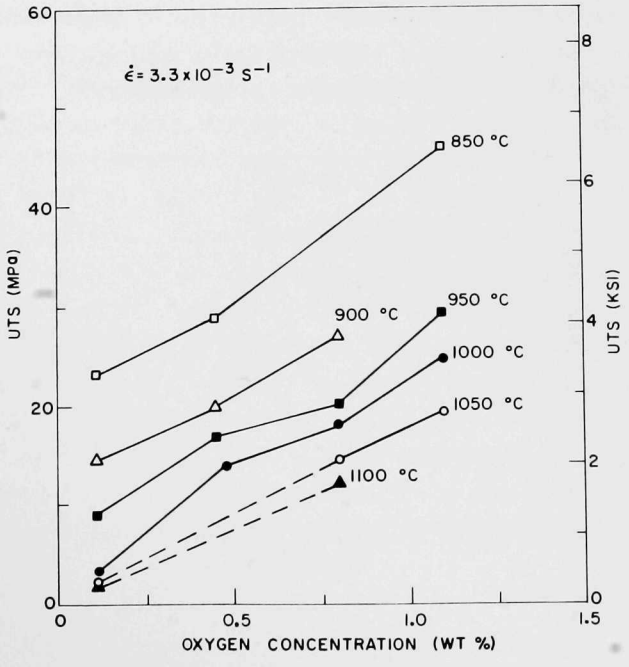

Fig. III.11

Effect of Oxygen on the UTS of Zircaloy-4 at Several Temperatures between 850 and 1100°C. ANL Neg. No. 306-76-15.

Figures III.12 and III.13 demonstrate the influence of oxygen on the uniform and total strain of Zircaloy-4, respectively. Except for the initial portion of the 850°C curve in Fig. III.12 (<0.5 wt % oxygen), the data indicate that the uniform strain increases as the oxygen concentration increases. This is probably the result of the work-hardening rate, which increases with oxygen concentration. In Fig. III.13 the total strain decreases as the oxygen concentration increases, except for the 900, 950, and 1000°C curves. The temperature range of the two-phase ($\alpha + \beta$) field for Zircaloy is altered by oxygen additions; thus, the phase distributions as well as the compositions of the phases must be considered in an attempt to rationalize the results presented in Figs. III.12 and III.13.

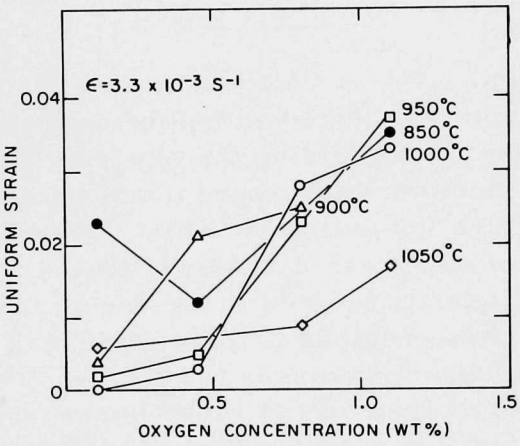

Fig. III.12. Oxygen Concentration Dependence of the Uniform Strain of Zircaloy-4 at 850, 900, 950, 1000, and 1050°C. ANL Neg. No. 306-76-17.

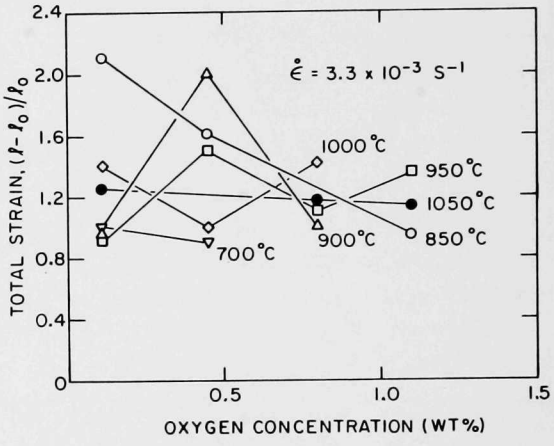

Fig. III.13. Total Strain of Zircaloy-4 as a Function of Oxygen Concentration at 700, 850, 900, 1000, and 1050°C. ANL Neg. No. 306-76-16.

Figure III.14 shows the influence of oxygen on the total strain of Zircaloy-4 as a function of temperature. The 0.11 and 0.45 wt % oxygen results were previously reported.[1] With increasing oxygen concentration, the low-temperature superplastic elongation peak (i.e., at 850°C for 0.11 wt % oxygen) shifts to higher temperatures. This observation is consistent with

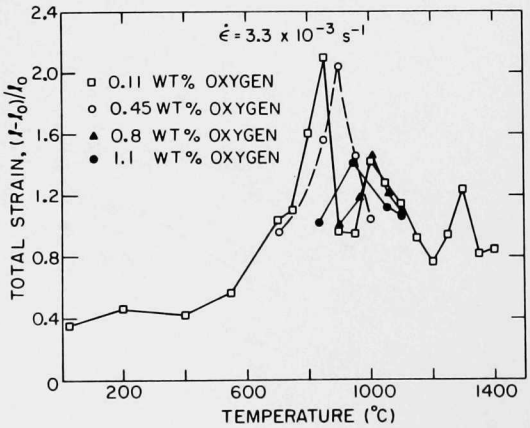

Fig. III.14

Effect of Oxygen on the Temperature Dependence of the Total Strain of Zircaloy-4. ANL Neg. No. 306-76-18.

the Zircaloy-oxygen phase diagram, since the $\alpha/(\alpha + \beta)$ boundary shifts to higher temperatures with increasing oxygen concentration. The figure also shows that the amount of elongation at the peak decreases as the oxygen concentration increases (i.e., 2.1 total strain at 0.11 wt % oxygen, compared with 1.4 total strain at 1.1 wt % oxygen). This decrease in elongation occurs because oxygen reduces the ductility of both the α and β phases. We could not determine the influence of oxygen on the high-temperature superplastic elongation peak (i.e., the peak at ~1000°C for 0.11 wt % oxygen) because of the long homogenization times required to obtain a small equiaxed grain structure with large oxygen concentrations at temperatures below ~850°C.

2. Composite Material with Oxygen Gradients in α and β Phases

Since the duration of a hypothetical LOCA in an LWR is quite short, steam oxidation of the Zircaloy cladding during an LOCA will produce $ZrO_2/\alpha/\beta$, $ZrO_2/\alpha/(\alpha + \beta)$, or ZrO_2/α composites with oxygen concentration gradients in each phase. Although an understanding of the influence of oxygen on the mechanical properties of the individual α and β phases will be useful in an interpretation of the mechanical properties of composite materials, it is essential to conduct tensile tests on composites.

Tensile specimens of the as-received Zircaloy-4 (containing 0.11 wt % oxygen) were heated in oxygen for 12 min at 800°C to increase the oxygen level to 0.8 wt %. This charging process produced a surface oxide layer and α phase with a steep oxygen concentration gradient. The oxide surface layer was quite thin, so that ~95% of the total thickness was α phase. However, the number of phase layers and/or the oxygen concentration gradient in each phase can change before high-temperature deformation in the INSTRON furnace. Metallographic examination of the fractured specimens will be used to determine the final layer thicknesses. Another batch of the composite specimens (with 0.8 wt % total oxygen concentration) was homogenized at 815°C for 25 days to obtain an equiaxed 17-μm α-phase grain size with uniform oxygen distribution across the specimen thickness.

Figure III.15 compares the temperature dependence of the total strain for the homogenized and composite specimens. Figure III.16 shows the corresponding comparison of UTS-versus-temperature data. All the homogenized specimens referred to in Figs. III.15 and III.16 were in the two-phase $(\alpha + \beta)$ region during the deformation. Thus, the composition and volume fraction of each phase varied according to the phase diagram at the test temperature, although there was no macroscopic oxygen gradient across the specimen. The structures of the composite specimens at the deformation temperature were as follows: oxide $|\alpha|$ oxide (800°C), oxide $|\alpha/(\alpha + \beta)/\alpha|$ oxide (850, 900, and 950°C, with decreasing thicknesses of the oxide and α-layers as the temperature increased), and $\alpha/\beta/\alpha$ (1000°C). An oxygen concentration gradient was present in each phase. Metallographic examination of the deformed samples revealed that the oxide surface was cracked severely in all cases and

the oxide/α interface was separated at several places. Thus, only the α and β layers of the composite were load-bearing. The results in Fig. III.15 demonstrate that the presence of a brittle α layer on the surface decreases the total strain (ductility) of Zircaloy considerably, although the UTS does not change significantly (Fig. III.16).

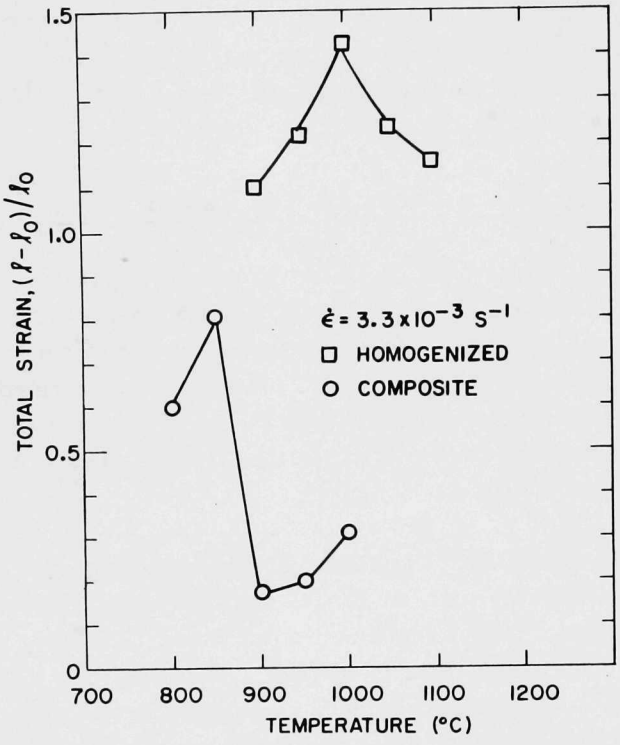

Fig. III.15

Temperature Dependence of the Total Strain of Homogenized and Composite Zircaloy-4 Specimens Containing 0.8 wt % Oxygen. ANL Neg. No. 306-76-23.

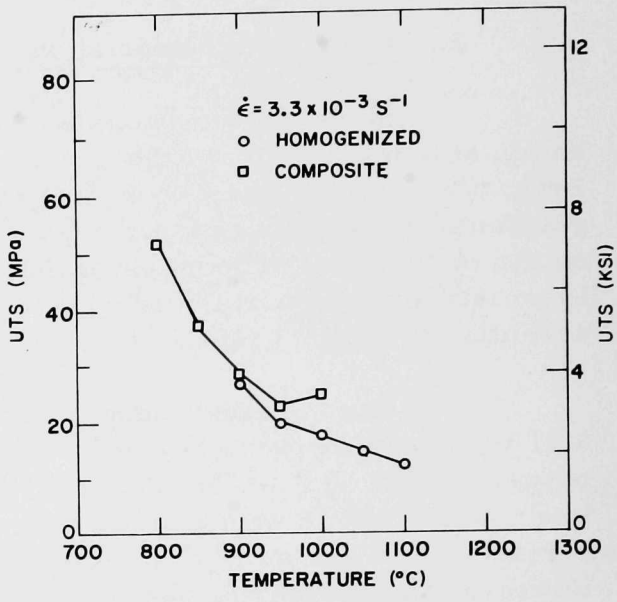

Fig. III.16

The UTS as a Function of Temperature for Homogenized and Composite Zircaloy-4 Specimens Containing 0.8 wt % Oxygen. ANL Neg. No. 306-76-22.

C. Biaxial Tube-rupture Experiments and Data-analysis Procedures

Details of the experimental procedures, test matrices, and preliminary test results on deformation and rupture characteristics of Zircaloy-4 cladding under biaxial-loading conditions have been reported previously.[1] In the present reporting period, a systematic study of the diametral expansion and rupture characteristics of as-received material in the stress-relieved condition has been performed by means of high-heating-rate transient-temperature tests. Several tests have also been conducted on oxidized-homogenized material. In view of the importance of superplastic deformation at ~850 and ~1050°C, particular effort was devoted to the accurate determination of the magnitude of circumferential strain at rupture in the vicinity of these temperatures.

A rapid-feedback power-control system for establishing programmed heating rates between 2 and 150°C/s was built and tested. Both Chromel-Alumel

and platinum, platinum-10% rhodium thermocouples (0.025-cm diameter) were successfully spark-welded to the as-received and oxidized specimens. Optimum spark-welding currents and voltages for both types of thermocouples have been determined for the different materials.

A 0.05-W helium-neon laser was used to illuminate the central 7.5-cm length of the Zircaloy tube. Both the direct and shadow images of the specimen length were monitored simultaneously on high-speed-camera film and were then used to determine the diametral strain by the technique reported previously.[1]

Information from the high-speed camera and the Visicorder readout of the temperature and pressure changes were used to establish the onset of plastic instability and the effective stress-strain relationships during deformation. A computer program was written to analyze the data from each rupture test. The computer printout gives the temperature, diametral strain, diametral strain rate, effective strain, effective stress, and stability function values, defined in Eq. 7 below, for each time increment (film frame) before rupture. An analysis of biaxial deformation of thin-wall tubing involves the determination of the functional forms of the effective stress and strain in terms of the principal stresses and strains that best describe the deformation behavior. In this investigation, the effective stress $\bar{\sigma}$ and strain $\bar{\epsilon}$ have been defined in terms of the principal stresses and strains by the respective relations

$$\bar{\sigma} = \frac{1}{\sqrt{2}}[(\sigma_z - \sigma_\theta)^2 + (\sigma_\theta - \sigma_r)^2 + (\sigma_r - \sigma_z)^2]^{1/2} \tag{1}$$

and

$$\bar{\epsilon} = \frac{\sqrt{2}}{3}[(\epsilon_z - \epsilon_\theta)^2 + (\epsilon_\theta - \epsilon_r)^2 + (\epsilon_r - \epsilon_z)^2]^{1/2}, \tag{2}$$

where the subscripts z, θ, and r refer to the axial, tangential, and radial components, respectively. In calculating effective strain up to the onset of plastic instability, we assumed that the tangential strain was equal to diametral strain and the axial strain was negligible. Beyond the point of onset of local ballooning, the assumption is no longer valid; therefore, the effective strain value is, at best, a crude approximation. The radial-strain value was obtained from the incompressibility equation

$$\epsilon_\theta + \epsilon_r + \epsilon_z = 0 \tag{3}$$

and the condition that $\epsilon_z \simeq 0$.

For the purpose of calculating the effective stress up to the onset of plastic instability, the tangential stress is given by

$$\sigma_\theta = \frac{P(t)D(t)}{2h(t)}, \tag{4}$$

where the condition of biaxiality is

$$\sigma_\theta/\sigma_z \simeq 2.0, \tag{5}$$

and the radial stress component $\sigma_r \simeq 0$.

The time-dependent values of the internal pressure and diameter are denoted by P(t) and D(t), respectively. The wall thickness h(t) was calculated from

$$\pi\left[\left(\frac{D}{2}\right)^2 - \left(\frac{D}{2} - h\right)^2\right] = \pi\left[\left(\frac{D_0}{2}\right)^2 - \left(\frac{D_0}{2} - h_0\right)^2\right], \tag{6}$$

where D_0 and h_0 are the initial diameter and wall thickness of the tube, respectively.

The plastic stability condition, discussed in the previous report,[1] can be rewritten as

$$D\,\frac{d^2D}{dR^2}\Big/2\left(\frac{dD}{dR}\right)^2 \lesssim 1 \text{ (plastically stable)}, \tag{7}$$

where D is the diameter and R is the high-speed-camera frame number before rupture, either an integer or an interpolated noninteger value. The left-hand side of Eq. 7, defined as the stability function, is computed from the information from each rupture test. An example was given in the previous report.[1]

D. High Heating-rate Rupture-test Results on As-received Zircaloy-4 Cladding

1. Stress-strain Characteristics

Twenty-three as-received and four oxidized-homogenized Zircaloy-4 tubes were tested with initial pressures that ranged from 1.4 to 9 MPa (200-1200 psi) and under uncontrolled transient-heating conditions at an initial heating rate of 115°C/s. Characteristic true effective stress and strain data are plotted as a function of temperature in Fig. III.17. The internal pressure initially increases slowly because of the thermal expansion of the argon gas; however, at a later stage, when the tube expansion rate is faster than that of the gas, the pressure starts to decrease during ballooning. However, the large radial and tangential strains more than compensate for the decrease in internal pressure, and the true effective stress thereby increases significantly from the initial value.

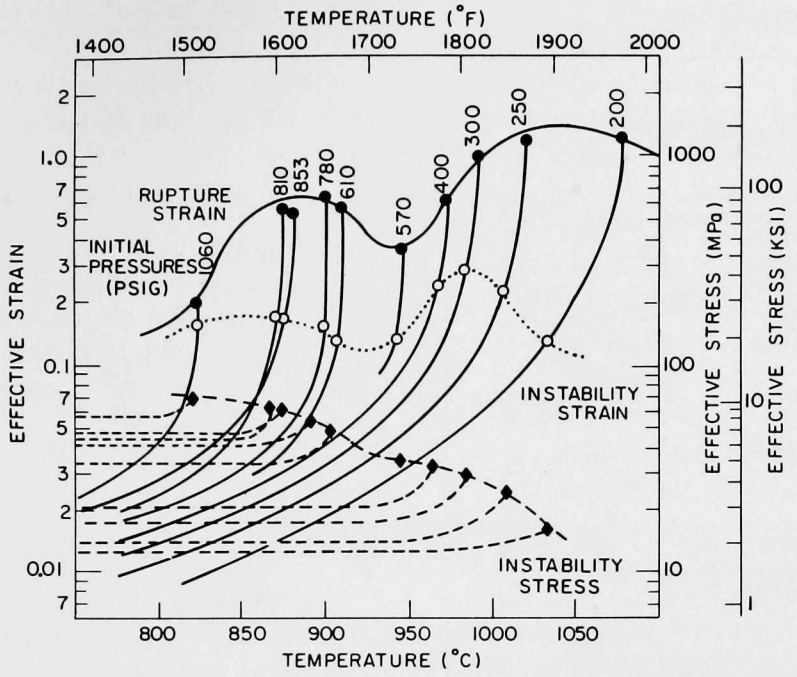

Fig. III.17. Effective Strain and Stress vs Temperature Obtained from Zircaloy-4 Tube-burst Experiments at an Initial Heating Rate of 115°C/s. Effective strain and stress at the onset of plastic instability are also shown. ANL Neg. No. 306-76-34.

The instability stress and strain determined by the method described in Sec. III.C are also shown in Fig. III.17. The effective strain values beyond the onset of plastic instability are only approximate. The rupture strain shows two maxima (at ~870 and ~1050°C) similar to the results from isothermal uniaxial tensile tests. The effective strain at the onset of plastic instability exhibits maxima that are much smaller, and the maximum at ~870°C is not very distinct. Note that transient-temperature deformation and rupture should be represented in a four-dimensional space with the following coordinates: $\bar{\sigma}$, $\bar{\epsilon}$, $\dot{\bar{\epsilon}}$, and T, i.e.,

$$F(\bar{\sigma}, \bar{\epsilon}, \dot{\bar{\epsilon}}, T) = 0. \tag{8}$$

In Fig. III.17 the strain-rate information is not shown. Because of the importance of the strain-rate sensitivity in the deformation behavior of Zircaloy, it is not meaningful to examine the relationship of σ versus ϵ, at constant temperature, from a cross-plot of the results in Fig. III.17.

Figure III.18 shows the stress-strain characteristics of oxidized-homogenized Zircaloy that contains 0.24 wt % oxygen and has an acicular α' structure. The material exhibits an effective strain during uniform expansion that is ~10 times smaller than that of as-received equiaxed α-phase material (Fig. III.17), and, as a result, the stress remains essentially constant up to the onset of plastic instability. Ballooning is responsible for most of the total rupture strain, and, as discussed previously,[1] the strain is concentrated at the limited number of sites where the α-colony grain direction is oriented parallel to the hoop-stress direction.

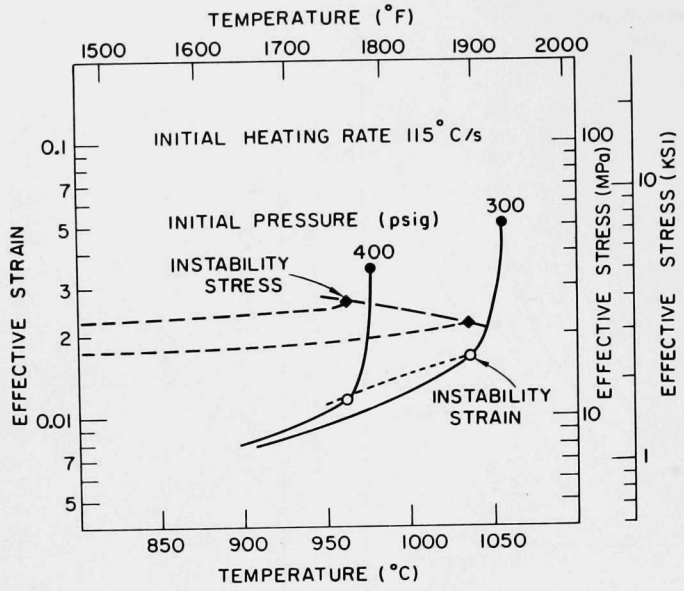

Fig. III.18

Effective Stress and Strain vs Temperature Obtained from Tube-burst Tests on Oxidized-Homogenized Zircaloy-4 Containing 0.24 wt % Oxygen. ANL Neg. No. 306-76-27.

From the results in Fig. III.17, the effective stress is plotted as a function of temperature (Fig. III.19) at several isostrain values up to the strain at the onset of instability. Extension of this plot to the strain at rupture is not possible because of the difficulty in calculating stresses beyond the onset of local ballooning. Figure III.19 can be used to predict values of uniform strain for any given initial pressure. However, from Fig. III.17, a considerable increase in the effective stress occurs near the onset of plastic instability. In this case, the stress increase should be compensated to predict strain values near instability.

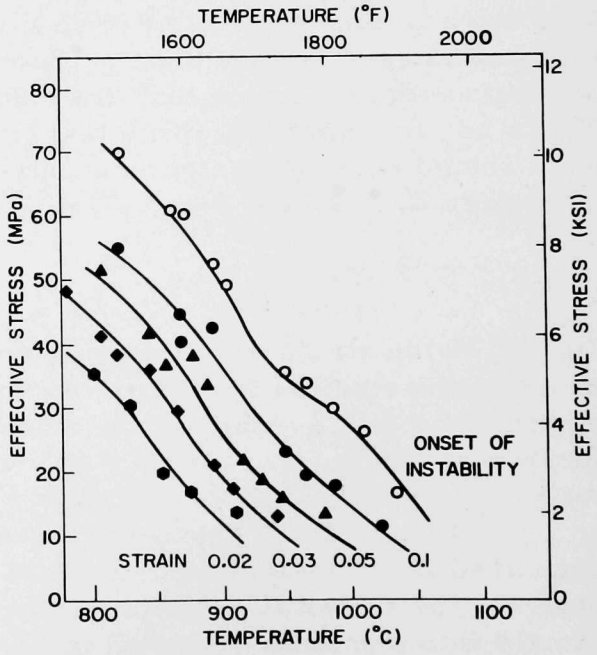

Fig. III.19

Effective Stress vs Temperature at Constant Effective Strain Values Obtained from Zircaloy Tube-burst Tests at an Initial Heating Rate of 115°C/s. Effective stress and temperature at onset of plastic instability are also shown. ANL Neg. No. 306-76-28.

2. Correlation of Burst Temperature with Circumferential Strain

The dependence of the burst temperature on the initial pressure is shown in Fig. III.20 for the as-received and the oxidized-homogenized Zircaloy containing 0.24 wt % oxygen. The results on the as-received material are in good agreement with the data on maximum pressure versus burst temperature reported by Hobson et al.[4] The oxidized-homogenized α' material is considerably stronger than as-received Zircaloy.

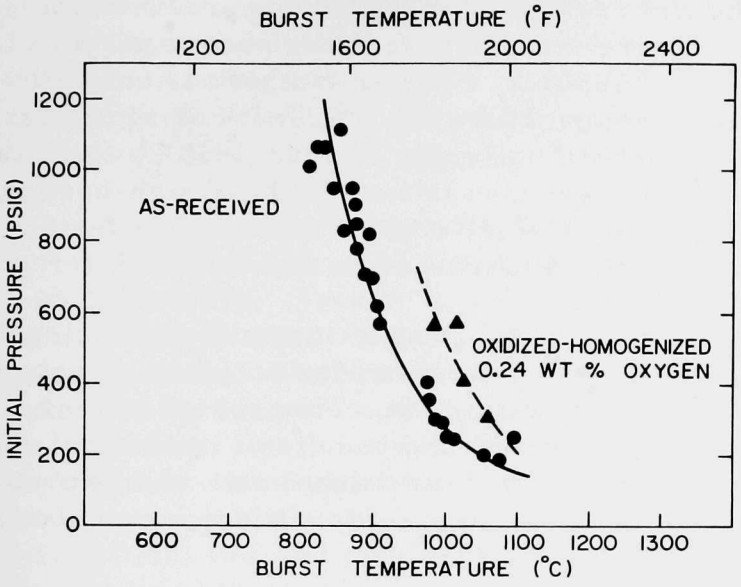

Fig. III.20

Initial Pressure vs Burst Temperature for As-received and Oxidized-Homogenized (0.24 wt % oxygen) Zircaloy Tubing for an Initial Heating Rate of 115°C/s. ANL Neg. No. 306-76-32.

Figure III.21 shows the maximum circumferential rupture strain versus burst temperature. Uniaxial strain data from the highest strain-rate tests ($\dot{\epsilon} = 3.3 \times 10^{-2}\ s^{-1}$) are shown for comparison. The circumferential strain has maximum values of 0.7 and 1.23 at ~870 and ~1050°C, respectively. The temperature of the first maximum is ~30-40°C higher than the

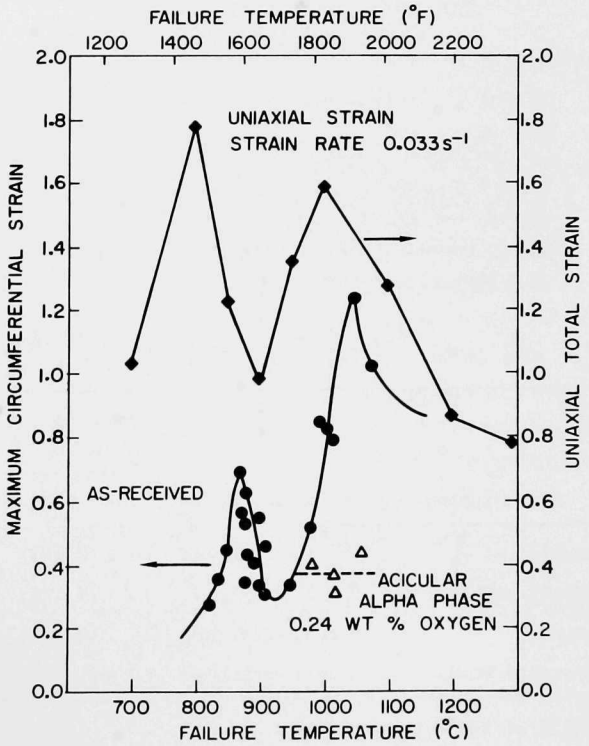

Fig. III.21

Maximum Circumferential Strain for As-received Zircaloy-4 Cladding (transient-heating tests at an initial rate of 115°C/s) and Uniaxial Strain for Sheet Material (isothermal uniaxial tensile tests at $\dot{\epsilon} = 3.3 \times 10^{-2}\ s^{-1}$) as a Function of Temperature. Circumferential strain data for homogeneous Zircaloy-4 tubing containing 0.24 wt % oxygen are also shown. ANL Neg. No. 306-76-30.

corresponding uniaxial peak temperature. Additional isothermal uniaxial data are being obtained to better define the peak for comparison with the biaxial data.

Biaxial transient-temperature deformation decreases the maximum rupture strain considerably. The first peak (830-870°C) is suppressed to a greater extent than the second peak (~1050°C). Also, in isothermal uniaxial deformation, the maximum elongation at ~850°C is larger than at ~1050°C, whereas the reverse is true in these high-heating-rate biaxial-rupture tests. This feature will be discussed in more detail later.

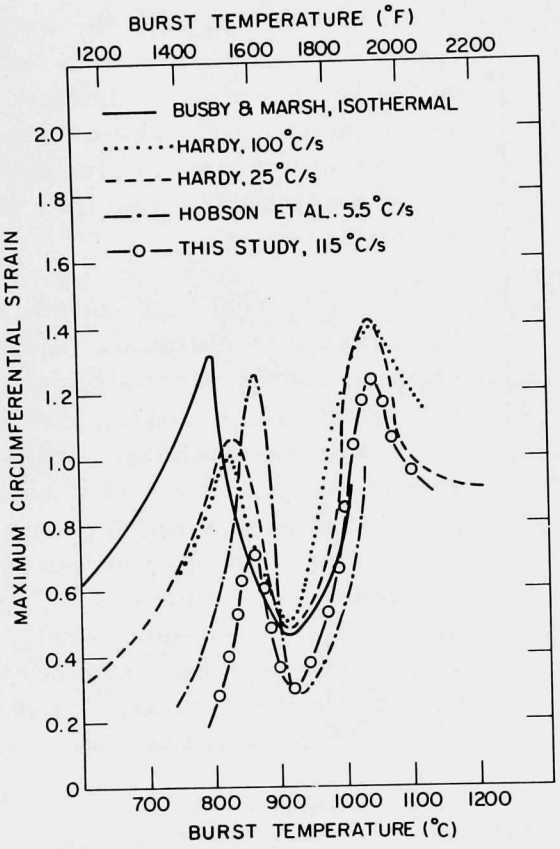

Fig. III.22

Comparison of Circumferential-strain and Burst-temperature Data on Unoxidized Zircaloy-4 Tubes That Have the Materials Parameters shown in Table III.1. ANL Neg. No. 306-76-29.

Acicular α' material containing 0.24 wt % oxygen does not show a rupture strain maximum. This observation is consistent with the results of isothermal uniaxial tests. Additional data will be obtained on this material for a wider range of rupture temperatures.

Figure III.22 compares the present rupture-strain-versus-temperature data with results of Hobson et al.,[4] Busby and Marsh,[5] and Hardy.[6] Table III.1 lists the tube dimensions, material conditions, and heating modes used in the various studies.

The strain minimum in the two-phase ($\alpha + \beta$) region at ~920°C, with strain values ranging from 0.25 to 0.5, is a common feature of these investigations. Compared with the data of Hardy,[6] the high-temperature rupture-strain maximum is somewhat smaller in the present study; however, the temperature agrees well,

TABLE III.1. Comparison of Material Condition, Tube Dimensions, and Heating Modes for Zircaloy-4 Biaxial-rupture Tests

Investigator	Material State	Nominal Outside Diameter, mm (in.)	Nominal Wall Thickness, mm (in.)	Wall-thickness Variation, mm	Heating Mode
Hobson et al.[4]	Stress-relieved	14.3 (0.563)	0.813 (0.032)	0.018-0.089	Transient from 315°C
Busby and Marsh[5]	Recrystallized	15.9 (0.626)	0.940 (0.037)	-	Isothermal
Hardy[6]	Stress-relieved	15.3 (0.601)	0.381 (0.015)	0.038	Transient from R.T.[a]
Present Study	Stress-relieved	10.9 (0.430)	0.635 (0.025)	0.038	Transient from R.T.[a]

[a]R.T. = room temperature.

i.e., ~1050°C. The low-temperature rupture-strain maximum reported by Hobson et al.[4] occurs approximately at the same temperature as the present data, i.e., ~870°C, but the rupture strain is considerably less in our work. Hardy showed that the rupture-strain maximum occurred at ~820°C for heating rates of 100 and 25°C/s, whereas, in the isothermal pressure-ramp rupture study of Busby and Marsh,[5] the first rupture-strain maximum was at ~800°C. From these observations, it may be difficult to find a definite correlation between the heating rate and the temperature and magnitude of the rupture-strain maximum at 800-870°C. However, other factors besides heating rate can influence the temperature and magnitude of the superplastic strain maxima.

For a given heating rate and geometrical arrangement, it is difficult to induce burst at the temperature of maximum expansion by adjusting the initial pressure. Therefore, a large number of burst tests are required in a narrow temperature range to accurately determine the temperature at the strain maxima. Wall-thickness variations and the extent of axial restraint can influence the magnitude of the rupture strain, but not the temperature at which the maximum strain occurs, provided a sufficient number of burst tests are performed. Although one end of the Zircaloy tube is not restricted in our tube-burst apparatus, the Al_2O_3 rod and end plugs (inserted in the tube to simulate fuel pellets) restrict tube contraction in the axial direction. Similar conditions existed in the Emery et al.[7] investigation. The axial restraint, due to the presence of pellets or a rod inside the tubing, is another factor that can lead to smaller rupture strain in our work when compared with the other results shown in Fig. III.22. Axial restraint as well as the effect of heating rate will be investigated in greater detail.

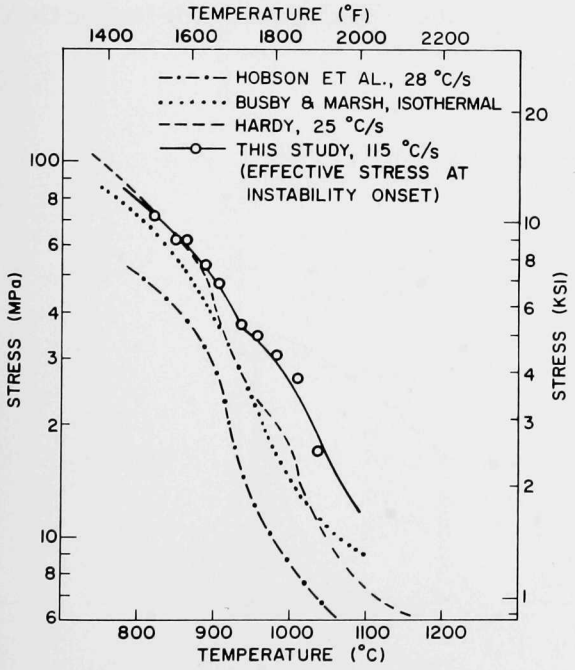

Fig. III.23

Comparison of Burst Stress from Other Investigations with the Effective Stress at the Onset of Plastic Instability from the Present Work. ANL Neg. No. 306-76-33.

Figure III.23 compares the effective stress at the onset of plastic instability from our results with the "rupture stress" reported by previous investigators. Note that ambiguities exist in the calculation of the rupture stress, i.e., the values of pressure, tube diameter, and wall thickness in the vicinity of the rupture. For the data of Hardy,[6] the initial hoop stress is plotted against rupture temperature. The agreement is good at low rupture temperatures, at which the ballooning and uniform strains are small. However, at higher rupture temperatures the rupture strength is apparently underestimated.

3. Local Ballooning Behavior

The present technique of monitoring individual frames during local ballooning by a high-speed camera enables a detailed characterization of the deformation after the onset of plastic instability. A new optical arrangement is being constructed to simultaneously monitor the circumferential shape in each frame in addition to the axial images.

Figure III.24 shows the ratio of diametral strain to the diametral strain at instability, as a function of temperature, from the onset of instability to rupture for several of the tests. The ratio indicates the comparative extent of expansion that takes place during local ballooning. It shows that for ballooning temperatures between 870 and 920°C and at 1000°C and higher, most of the strain at rupture can be attributed to local ballooning. Therefore, it is important to have the capability to calculate ballooning deformation subsequent to the onset of plastic instability in these temperature ranges. The temperatures at which the maxima in the ratio occur are close to the temperatures of the rupture-strain maxima in Fig. III.22. Figure III.24 indicates that the temperature region is the predominant factor in determining the extent and kinetics of local ballooning before rupture. The three experiments in the β phase above 980°C had longer time intervals before rupture and a greater extent of ballooning as the temperature increased. Apparently the rate of stress relaxation by recovery and/or dynamic recrystallization increased as the ballooning temperature increased to the optimum values of ~1060°C. Ballooning deformation,

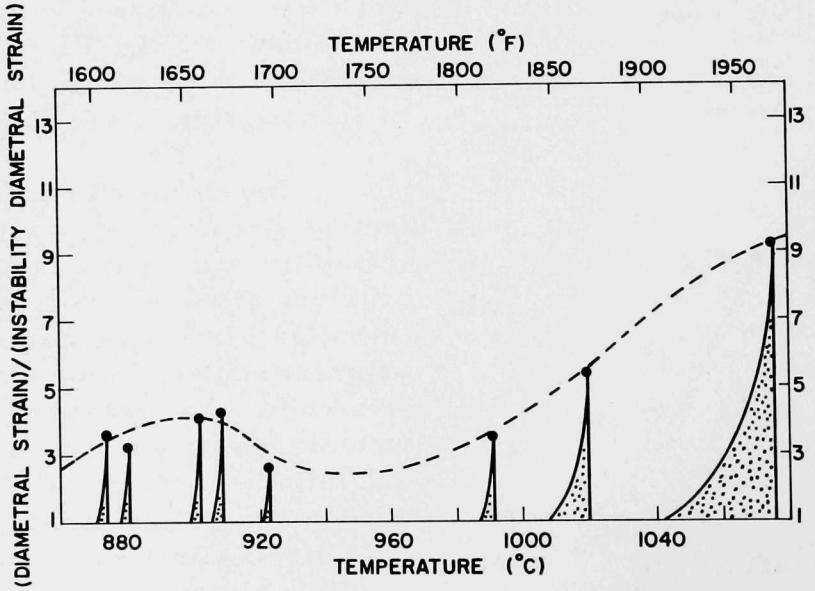

Fig. III.24. Ratio of the Diametral Strain at Rupture to the Diametral Strain at the Onset of Plastic Instability vs Burst Temperature. Intersections of the curved and vertical lines with the temperature abscissa correspond to the temperatures for the onset of instability and rupture, respectively. ANL Neg. No. 306-76-26.

which is the major portion of the total rupture expansion, is primarily sensitive to temperature over a small interval. This fact should enable us to correlate, in a simple manner, the ballooning deformation with a temperature-sensitive material property, e.g., the strain-rate sensitivity. This approach will be pursued further for a range of heating rates between 5 and 120°C/s.

Figure III.25 shows rupture experiments that were conducted in an identical manner, except for a difference in heating rate. Both reached the onset of local ballooning with approximately the same diametral strain but at temperatures of 1005 and 1069°C. The diametral-strain-versus-time data show that both tubes have approximately the same strain-rate history. However, the diametral-strain-versus-temperature results show that one tube ruptured at ~80% strain and the other at ~120%. Considering the similar strain and strain-rate histories of both tubes, we conclude that the faster relaxation rate at ~1080°C is responsible for the increased rupture deformation.

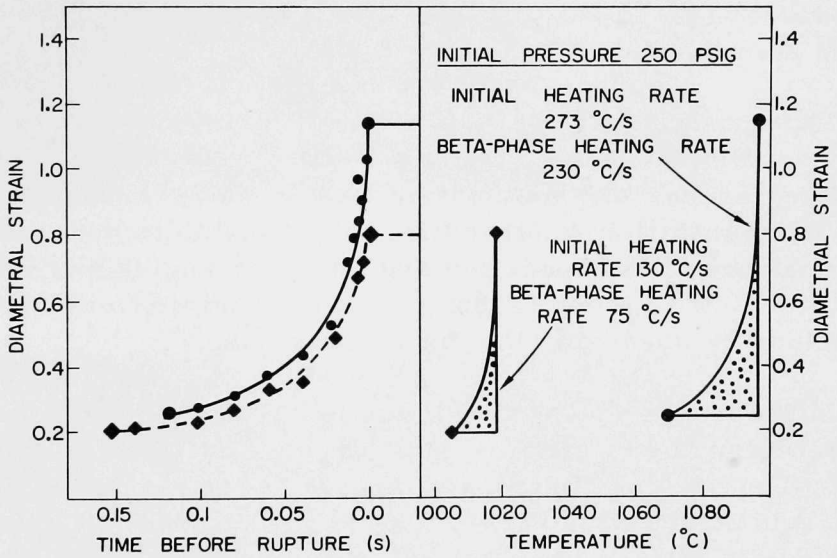

Fig. III.25. Diametral Strain between the Onset of Plastic Instability and Rupture for Zircaloy-4 Cladding Heated at Different Initial Rates. Although the deformation strain and strain-rate histories are comparable, a large difference in the final expansion results because of a larger relaxation rate at ~1080°C than at ~1010°C. ANL Neg. No. 306-76-31.

4. Microstructural Examinations of the Zircaloy-4 Tubing

The uniform strain portions of the specimens that ruptured in the α region or near the $\alpha/(\alpha + \beta)$ transus had equiaxed α grains of ~2- to 3-μm size that formed from the elongated grains in the stress-relieved initial material by thermal recrystallization during heating. However, no evidence of dynamic recrystallization, as a result of deformation, was found, even in specimens that burst at 850-870°C (the temperature range at which the first rupture-strain maximum occurred). This may account for the fact that only

~70% strain was observed in this temperature range, whereas isothermal uniaxial deformation resulted in 130% strain (Fig. III.21). Elongated α grains were found at the rupture area of the tube, and their width was comparable to that of the equiaxed α grains in the regions of uniform deformation. Correlation of the rupture strain at ~850°C with the extent of dynamic recovery and recrystallization of α-phase material will be pursued further for low-heating-rate and isothermal stress-rupture tests.

The specimen that showed a maximum circumferential expansion of 123% at a rupture temperature of ~1050°C was found to exhibit a rim α structure after transformation from the β field. This type of structure has been discussed by Östberg.[8] We have observed the rim α structure infrequently, usually in Zircaloy specimens that were transformed by cooling from temperatures ~20-70°C above the $\beta/(\alpha + \beta)$ transus at moderate initial rates. Rim α forms at the β-grain boundaries at an early stage of the $\beta \rightarrow \alpha'$ transformation when the driving force for the transformation to the Widmanstätten structure is not large enough. If cooled too fast, the Widmanstätten structure dominates the transformation.

The optimum microscope contrast for rim α can be obtained by deep etching, anodizing at 90 V, and observation with a rotatable analyzer and differential interference contrast. Depending on the relative direction of the surrounding Widmanstätten α structure, rim α exhibits best contrast at particular combinations of the specimen and analyzer angles and interference objective rotation. With these techniques it is possible to identify the previous β-grain structure by observing the rim α structure.

Micrographs that reveal these features are shown in Figs. III.26 and III.27 for regions of relatively small strain and for the rupture regions, respectively. The previous β-grain structure in the rupture region in Fig. III.27 is equiaxed, and the grain size is ~2-2.5 times smaller than that in Fig. III.26. Both factors indicate that some dynamic recrystallization occurred during deformation at temperatures in the β-phase region.

After rupture at ~1050°C, the specimen remained at temperatures in the β phase for ~2.1 s. Apparently, simultaneous recovery and dynamic recrystallization resulted in rapid softening at this temperature and caused the large superplastic deformation. This feature will be studied further in lower-heating-rate tests. Optimum cooling-rate adjustment after rupture and/or a decoration technique will be explored to better reveal the previous β-grain structure at the higher-temperature strain maximum.

E. Development of a Failure Criterion for Oxygen-embrittled Zircaloy Cladding

In conjunction with the experimental program, a modeling effort that uses finite-element methodology has been initiated with the following objectives: (1) to provide an analytical tool for interpretating the mechanical-property data and ensure that the test results are presented in a form useful

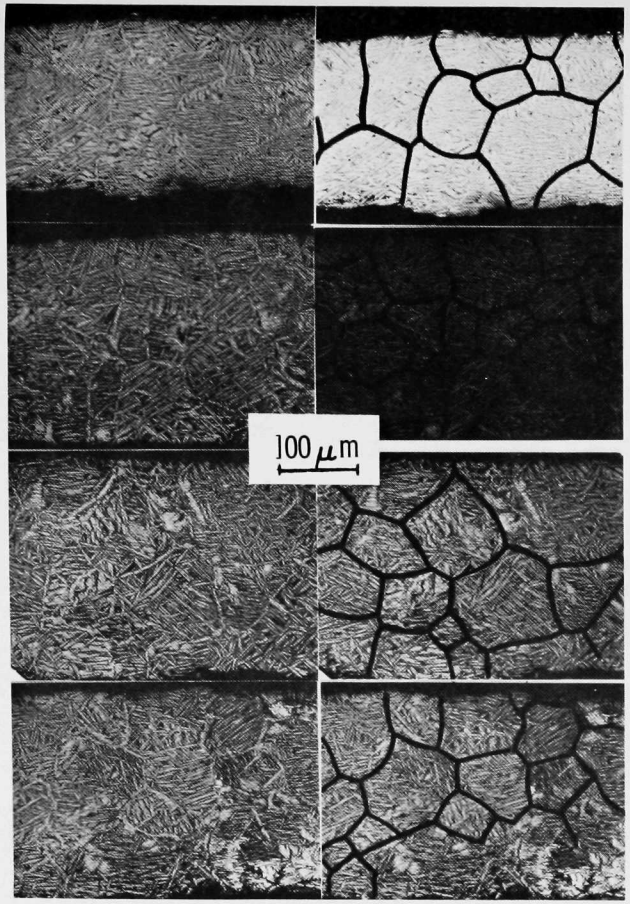

Fig. III.26

Rim α and Previous β-phase Grain Structure of Uniform Deformation Areas of a Zircaloy-4 Tube Ruptured at ~1050°C with 125% Circumferential Strain. Etched, anodized, differential interference contrast. Grain structure outlined by pen on right-hand photos. ANL Neg. No. 306-76-37.

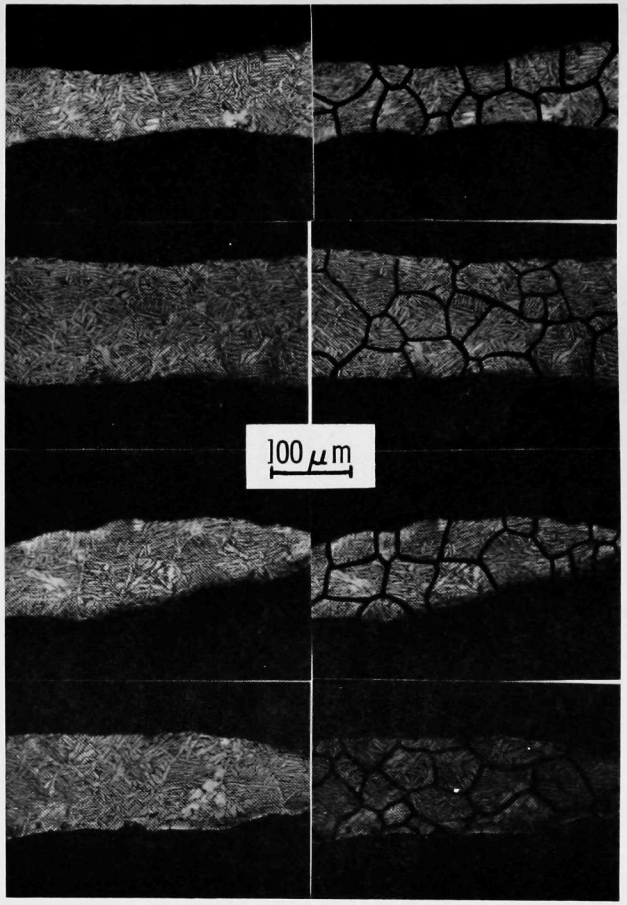

Fig. III.27

Rim α and Previous β-phase Grain Structure of Rupture Areas of a Zircaloy-4 Tube That Burst at ~1050°C with 125% Circumferential Strain. Note the smaller equiaxed β-grain size when compared with Fig. III.26. Etched, anodized, differential interference contrast. Grain structure outlined by pen on right-hand photos. ANL Neg. No. 306-76-36.

to fuel-element analysis and design, (2) to study the deformation behavior of Zircaloy cladding under various postulated LOCA and PCM conditions, and (3) to establish physical interpretations and, if necessary, recommend modifications to the present acceptance criteria[9] for the ECCS in LWR's based on the mechanical behavior of oxygen-contaminated Zircaloy.

Unlike integrated fuel-element-behavior codes, such as FRAP-T2,[10] the present finite-element code will not consider the behavior of the fuel or the effects of irradiation on the cladding, but will concentrate on the mechanical-deformation behavior of Zircaloy during LOCA and PCM transients. The detailed deformation studies, along with the mechanical-property data, will provide pertinent constitutive information on the cladding. A deformation analysis that considers the state of the material in detail (e.g., composite $ZrO_2/\alpha/\beta$ structure with oxygen gradients) can be used to establish the validity of simplified models containing average materials properties (e.g., the FRAP-T2 code). On the other hand, FRAP-T2 generates valuable information about the fuel behavior and fuel-cladding mechanical interaction that the finite-element code will use as input information in the LOCA and PCM studies.

1. Requirements of the Finite-element Code

In view of the experimental information on the high-temperature mechanical properties of both as-received and oxidized Zircaloy, particularly with regard to superplasticity and strain-rate sensitivity, the finite-element code must have the capability to analyze (a) large deformation, (b) elastic-plastic (possibly elastic visco-plastic) behavior, (c) effects of multiphase structure and phase transformations, (d) effects of oxygen concentration and concentration gradients, (e) anisotropic behavior at temperatures below ~800°C, (f) steady-state and transient heat transfer, and (g) fracture phenomena in the material.

To use the available nonlinear codes and thereby minimize the initial developmental effort, a literature and software-market survey was conducted that led to the selection of NONSAP.[11] The NONSAP code has the elastic-plastic analysis option and, for large deformation, provides both the Lagrangian and updated Lagrangian (or Eulerian) formulations; thus it meets requirements (a) and (b). The SIMTRAN-I (Ref. 12) computer code developed at Oak Ridge National Laboratory (ORNL) simultaneously solves the one-dimensional heat-conduction and oxygen-diffusion equations by a finite-difference technique. Thus, it provides the information on the oxygen distribution, temperature profile, β-phase thickness, and motion of the ZrO_2/α and α/β phase boundaries required in items (c), (d), and (f).

An IBM version of NONSAP has been acquired from the University of Southern California, and reorganization and modification of the code are in progress. As soon as SIMTRAN-I is received from ORNL, work on incorporating certain features of the code into the deformation analysis will be initiated.

The experimental deformation behavior of Zircaloy cladding under different temperatures and pressure transients will be compared with results obtained from the finite-element code. The adequacy of a one-dimensional semi-empirical constitutive relation, based on uniaxial tensile data, for prediction of biaxial deformation behavior will be examined. The onset of plastic instability also will be studied both experimentally and analytically.

2. Establishment of the Embrittlement Criterion

Of the five current acceptance criteria[9] for the ECCS in LWR's, the first three have direct implications with regard to the mechanical behavior of the Zircaloy cladding. The third, that a coolable core geometry be maintained, was considered in establishing the first two: (a) The peak cladding temperature shall not exceed 1204°C (2200°F), and (b) the total oxidation shall nowhere exceed 17% of the cladding thickness before oxidation.

The intent of these criteria is to avoid coolant flow blockage after blowdown and ensure sufficient cladding ductility during the reflood stage of an LOCA. Although local ballooning and burst of the Zircaloy cladding may occur during an LOCA, the cladding must be capable of containing the UO_2 fuel pellets and maintaining the core geometry. These criteria are intended to be conservative. However, the quantitative limits of the first two criteria are not without controversy,[9] in that the arguments were based on a limited knowledge of the mechanical behavior of the oxidized Zircaloy as well as uncertainties in the stress calculations (due to an inadequate mechanical-property data base). The results of the present program will be used to assess the degree of conservatism and provide the physical interpretations of the criteria based on a better understanding of the mechanical behavior of Zircaloy and more detailed analyses of cladding deformation under LOCA and PCM conditions. The superplastic deformation characteristics of Zircaloy at ~850 and ~1050°C will be carefully considered with regard to ballooning deformation of the cladding and possible flow blockage. A fracture-mechanics approach will be used to determine the capability of the material to withstand thermal shock as well as mechanical loading during reflood for various degrees of cladding oxidation. If necessary, the criteria will be restated along with justifications.

References

1. Light-water-reactor Safety Research Program: Quarterly Progress Report, July-September 1975, Sec. III., "Mechanical Properties of Zircaloy Containing Oxygen," ANL-75-72 (Feb 1976).

2. E. Tenokhoff, Operable Deformation Systems and Mechanical Behavior of Textured Zircaloy Tubing, Zirconium in Nuclear Applications, ASTM STP 551, American Society for Testing and Materials, p. 179 (1974).

3. A. M. Garde, E. Aigeltinger, B. N. Woodruff, and R. E. Reed-Hill, Concerning the Strength of Dynamic Strain Aging in Zirconium, Met. Trans. 6A, 1183 (June 1975).

4. D. O. Hobson, M. F. Osborne, and G. W. Parker, Comparison of Rupture Data from Irradiated Fuel Rods and Unirradiated Cladding, Nucl. Tech. 11, 479 (1971).

5. C. C. Busby and K. B. Marsh, High Temperature Deformation and Burst Characteristics of Recrystallized Zircaloy-4 Tubing, WAPD-TM-900, Bettis Atomic Power Laboratory, Pittsburgh, Pa. (Jan 1970).

6. D. G. Hardy, High Temperature Expansion and Rupture Behavior of Zircaloy Tubing, Topical Meeting on Water-reactor Safety, Salt Lake City, Utah, March 26-28, 1973, G. A. Freund, Compiler, pp. 254-273.

7. A. D. Emery, D. B. Scott, and J. R. Stewart, Effects of Heating Rate and Pressure on Expansion of Zircaloy Tubing During Sudden Heating Conditions, Nucl. Tech. 11, 474 (1971).

8. G. Östberg, Metallographic Study of Isothermal Transformation of Beta Phase in Zircaloy-2, Jernkontorets Ann. 145, 119 (1963).

9. USAEC Docket No. RM-50-1, Acceptance Criteria for Emergency Core Cooling Systems for Light-Water-Cooled Nuclear Power Reactors (Dec 1973).

10. J. A. Dearien et al., FRAP-T2 A Computer Code for the Transient Analysis of Oxide Fuel Rods, Vol. I., Aerojet Nuclear Co. (July 1975).

11. K. J. Bathe, E. L. Wilson, and R. H. Iding, NONSAP--A Structural Analysis Program for Static and Dynamic Response of Nonlinear Systems, Report No. UCSESM 74-3, University of California, Berkeley (Feb 1974).

12. S. Malang, SIMTRAN I--A Computer Code for the Simultaneous Calculation of Oxygen Distributions and Temperature Profiles in Zircaloy During Exposure to High-Temperature Oxidizing Environments, ORNL-5083 (Nov 1975).